Master thesis and internship[BR]- Master's thesis : Holography based on incoherent thermal infrared light in view of metrology applications[BR]- Internship

Auteur : Adrian, Nicolas
Promoteur(s) : Georges, Marc
Faculté : Faculté des Sciences appliquées
Diplôme : Master en ingénieur civil en aérospatiale, à finalité spécialisée en "aerospace engineering"
Année académique : 2023-2024
URI/URL : http://hdl.handle.net/2268.2/20416

Holography based on incoherent thermal infrared light in view of metrology applications

Master's thesis completed in order to obtain the degree of Master of Science in Aerospace Engineering.

Author
Adrian Nicolas

Academic supervisors
Dr. Georges Marc
Dr. Clermont Lionel

University of Liège
School of Engineering and Computer Science

Academic year 2023-2024

Abstract

The main objective of this work was to perform holography using self-emitted infrared light. To do so, holography was first studied by exploring a variety of scientific articles. These articles revealed that two main types of interferometers were used in that field, i.e., the Michelson and the Mach-Zehnder. Following this, it was possible to perform a preliminary study involving optical components assessment and ray tracing simulations. Then, it was possible to determine that the Mach-Zehnder setup was the most practical one, given the ZnSe components' availability in the laboratory. At this point, the practical implementation of the Mach-Zehnder could begin, involving the alignment in the visible domain using a coherent source, i.e., a Helium-Neon laser. Following that, a visible incoherent source, the SuperK Compact, was chosen. It was then possible by using filters to start from a low coherence and progressively decrease it up until reaching a totally incoherent source, i.e., without filters. Thus, the interferometer was aligned to enable interferometry with a white incoherent source. Finally, it was possible to use a self-emitting source, in this case, a welding iron at 450°C, to perform holography. For that purpose, images were recorded using a thermal camera, however, due to the beamsplitters' reflectance, the signal of interest was mixed with noise. Since no other beamsplitters were available at the laboratory, it was not possible to overcome this. However, it was supposed that increasing the reflection of the first beam splitter would yield a better signal-to-noise ratio, therefore effectively increasing the signal of interest compared to the thermal background noise.

Acknowledgments

I am incredibly thankful to my promotor and co-promotor, Dr. M. Georges, and Dr. L. Clermont. Their guidance, advice, motivation, and mentorship properly from the start until the final stage of my research, and their expertise, patience, and sound advice have genuinely contributed to the successful completion of this work. Their support and continuous mentorship in the lab, arduous proofreading, and seamless aid have enlightened the project immensely.

I am deeply indebted to my family for their endless support and motivation. Their belief in me and sustained inspiration always guided me through the challenges that I was facing. Special thanks also go to my significant other, for her patience, understanding, and unflagging support in the most demanding times of this research journey.

I am thankful to each member of the CSL for having created an environment full of positivity and good vibes. Members' support and the excellent climate they keep have been important factors that increase productivity and enjoyment in conducting my research. Most notably, I am thankful for the necessary warm and friendly atmosphere, cooperation, and challenging exchanges with my colleagues L. V., L. B., and E. R. Their encouragement and support have had fantastic value in crafting the course of this research.

Finally, I would like to thank everyone who has directly or indirectly contributed to this work. The support given is incredibly welcome and shall never be forgotten.

Thanks to you all.

Contents

1 | Introduction

In this chapter, an overview of **holography** from its **historical background** and evolution since the pioneering work of Denis Gabor up to its modern application will be given. Basic principles and **governing equations** of holography are discussed where a recording process of amplitude and phase information of light waves is elaborated. Differences between analog and digital holography, their techniques, sets of **advantages**, and **limitations** are also discussed in this chapter. Moreover, the chapter discusses **applications** in metrology to aerospace, e.g., non-destructive testing. The chapter then discusses **low coherence holography** with challenges and the innovation of using low coherence and incoherent light sources. The **organization** of this Master's thesis is done giving the theoretical background of the experiments carried out, including setups and methodologies of the study.

1.1 Historical context of holography

Holography is a technique developed by Denis Gabor and it has evolved from a mere laboratory test to a cornerstone of modern optical science, revolutionizing various fields [1]. It promises an unparalleled depth of insight into the fundamental properties of light and matter, revealing the secrets of dimensionality with high precision and clarity. Compared to conventional photography, which only records the intensity of light, holography records both the amplitude and phase of light waves. Therefore, it preserves more spatial information that will faithfully reproduce the details and nuances of the scene. Hence, holography transcends traditional imaging techniques' limitations, thus offering a perspective into the interplay of light and matter at the quantum level [2, 3]. This recording is based on the interplay of a reference and object beams, through the use of an interferometer. This in turn generates an interference pattern containing sufficient information to reconstruct the three-dimensional optical field emanating from an object [4].

Building upon this foundational understanding of holography, it is necessary to examine the two primary techniques employed to record holograms, i.e.: analog and digital holography. Both methods involve distinct approaches to recording and reconstructing holograms, each with its own set of advantages and drawbacks. The original form of holography developed by Dennis Gabor, analog holography, records holograms on photographic film using laser light. The interference pattern resulting from the interaction of the reference and object beams is recorded onto the film, which preserves both the amplitude and phase information of the light waves. These analog holograms can then be analyzed by illuminating them, revealing a three-dimensional image that appears to float in mid-air. Even though this technique offers high fidelity and resolution, it is limited by the constraints of the photographic film. Moreover, it is impossible to easily store and manipulate the obtained holograms.

On the other hand, digital holography leverages digital sensors and computational techniques to record and reconstruct holograms in a more versatile and efficient manner. In this case, the interference pattern is captured by a digital sensor, e.g., a CCD or CMOS camera, and stored as numerical data. These data can then be processed to reconstruct holographic images, thus allowing for real-time visualization, storage, and manipulation. Digital holography exhibits

numerous advantages over analog holography. This includes the ability to digitally store and transmit holographic data, compatibility with modern computing technologies, and flexibility in the post-processing of the data. Nevertheless, this technique may lead to lower resolution and fidelity, depending on the digital sensor and processing algorithms used. Hence, while analog holography excels in terms of fidelity and image quality, digital holography provides greater versatility and convenience concerning data handling and processing.

1.2 Holography's governing equations

In the case of digital holography, all the recordings correspond to holograms in transmission. Therefore, it is possible to define the object beam such that

$$E_{\text{obj}}(x,y) = o(x,y)e^{i\phi_{\text{obj}}(x,y)} \tag{1.2.1}$$

where $o(x,y)$ and $\phi_{\text{obj}}(x,y)$ are the real amplitude and phase, respectively.
The reference beam can be considered as a collimated beam. Hence, taking into account an amplitude r, the wavelength λ, and an angle θ between the reference and object beam, it can be defined as

$$\begin{cases} E_{\text{ref}}(x,y) = r(x,y)e^{2i\pi\xi x} \\ \xi = \frac{\sin(\theta)}{\lambda} \end{cases} . \tag{1.2.2}$$

The resulting intensity on the hologram plane is therefore given by

$$I_h(x,y) = \left|E_{\text{obj}}(x,y) + E_{\text{ref}}(x,y)\right|^2 . \tag{1.2.3}$$

In terms of the absorbed light energy, the transmission of the holographic plane is expressed as

$$\tau(x,y) = b\, t_b\, I_h(x,y)\,, \tag{1.2.4}$$

where t_b is the exposure time and b is the slope of the linear response.

Given that the hologram is reconstructed by illuminating the holographic plane with the same reference beam used during recording, it is appropriate to express it as

$$\begin{aligned} H(x,y) &= \tau(x,y)\, E_{\text{ref}}(x,y) \\ &= H_1(x,y) + H_2(x,y) + H_3(x,y) + H_4(x,y). \end{aligned} \tag{1.2.5}$$

Where

1. H_1 represents the reference beam transmitted through the hologram plane in a straight line and is given by
$$H_1(x,y) = (b\, t_b\, r^2) r e^{2i\pi\, \xi\, x}. \tag{1.2.6}$$
This term includes a constant factor and a quadratic dependence on the exposure time, representing the amplitude of the reference beam.

2. H_2 is the halo term surrounding the transmitted reference beam, i.e., H_1. The halo term is therefore expressed as

$$H_2(x,y) = b\,t_b\,r\,o^2(x,y)e^{2i\pi\,\xi\,x}. \tag{1.2.7}$$

3. H_3 corresponds to the intensity of the original object with a multiplicative constant, and this term is given by

$$H_3(x,y) = b\,t_b\,r^2\,o(x,y)e^{i\phi_{\text{obj}}(x,y)}. \tag{1.2.8}$$

   The exponential term $e^{i\phi_{\text{obj}}(x,y)}$ introduces a phase shift related to the object phase.

4. H_4 is the complex conjugate of the complex amplitude of the original object beam. It represents the real image of the object and is given by

$$H_4(x,y) = b\,t_b\,r^2\,o(x,y)\,e^{-i\phi_{\text{obj}}(x,y)}e^{4i\pi\,\xi\,x}. \tag{1.2.9}$$

   With the exponential factor, $e^{4i\pi\,\xi\,x}$, indicating that the conjugate wave is shifted with respect to the normal by an angle approximately double that of the reference wave with the same axis

Usually, these terms are referred to in the

- 0^{th} order, containing the non deviated terms, i.e., H_1 and H_2;
- 1^{st} order, containing the real image, i.e., H_3;
- -1^{st} order, containing the virtual image.

When the angle between the reference and object beams, θ, is zero, this is referred to as *in-line* holography, the four terms are overlapping. On the other hand, the *off-axis* holography has a lower noise level as only one of the terms, i.e., the virtual or real image, is used to measure the phase. The reconstruction is then performed numerically by multiplying the transmission function of the hologram by the analytical expression of the reference beam. Therefore, to have a reference beam that can be simulated numerically, a plane or spherical wave is chosen.

1.3 Applications for metrology in aerospace

The possibility of retrieving the amplitude and phase of object beams by holography found some interesting applications for metrology in the aerospace industry. In the space context, two main applications rely on the comparison of the phase of object beams, which evolve with time. The first one is based on changes in the object's shape and is called non-destructive testing [5, 6]. In the early time of holography, mechanical deformations of structures were also demonstrated [7, 8]. The second application concerns the changes of refractive index in transparent media [5]. This could potentially be used for microgravity experiments to

measure fluid phenomena and crystal growths [6, 9, 10, 11], first under microgravity environments, and later through digital holography [12]. These consisted mostly in measuring refractive index variation by measuring phase changes in liquid cells. All these experiments were carried out thanks to the use of lasers in the visible domain, and in stable conditions.

Due to the high constraint of setup stability, i.e., the setup must be stable at a fraction of the wavelength used, holographic non-destructive testing with visible lasers was badly adapted to the actual applications for measuring thermo-mechanical deformation of large space structures in true testing facilities, such as those of the CSL. To overcome this, holographic non-destructive testing at long-wave infrared (LWIR) wavelengths was developed at the CSL, thanks to the use of CO_2 lasers, providing light in the 10 μm wavelength range. Since no analog material could be found in that range, digital recording was considered [13, 14]. Finally, it is important to note that whether in the visible or LWIR, all the applications of holography were developed based on coherent light with a laser illumination of good coherence length.

1.4 Holography in low coherence

In low coherence, i.e., for light sources with short coherence lengths, the optical field does not maintain a stable and predictable phase relationship over long distances. Therefore, the light waves are emitted with random phase differences. Due to the low coherence characteristic, the optical path lengths followed by the waves must be the same, or at least very similar. For this purpose, common-path interferometric configurations will be used, as they usually separate the incoming beam into two separate beams, i.e., the reference and object beams. Each of these paths must be within the coherence length to provide interference patterns.

Using common paths interferometers, such as the Mach-Zehnder or the Michelson, provides a variety of degrees of freedom to ensure that the reference and object waves travel the same or nearly identical distances. Additionally, as both the reference and object waves experience the same optical path length variations, this makes this type of setup more robust against environmental disturbances. Overall, common path interferometers are required to perform holography, in the case of low coherent sources.

Holographic experiments with low coherence sources, such as laser diodes, for transparent objects, exist, particularly in the field of digital holographic microscopy. These experiments are feasible because the setup is based on the Mach-Zehnder configuration [15, 16]. Up to now, such systems work in the visible domain and are commercially available for various applications in the biomedical field.

Going further to totally incoherent light, applications with natural light holography, or, in the thermal infrared spectrum based on self-emission could be rendered possible. While the use of holography with natural white light was demonstrated, the use of self-emission incoherent light was barely approached as of today. Applying this concept in the thermal infrared range could be of interest for various applications, where the phase of light can be used to extract useful information, without requiring an illumination source. For example, 3D localization of

hot particles or other objects, or 3D temperature profiles, where the temperature information is inherently present in the signal, while its phase is reconstructed by holography would provide a means to retrieve profile or distance information.

1.5 Organization of this Master thesis

This master thesis is structured to provide a comprehensive exploration of holography in low coherence conditions. After this introduction on the historical aspect, governing equations, and applications of infrared holography, the focus will shift to a theoretical background covering the basic principles of the concepts discussed throughout this thesis. In particular, the temporal and spatial coherence aspects of light, the types of interferometers considered, and the fundamental equations of interferometry will be covered.

Following this theoretical background, previous holographic experiments in low coherence, using setups similar to the ones presented, will be analyzed along with their results. Similarities and differences will be acknowledged, providing a starting point for the practical implementation. Thermal infrared self-emission will then be covered, along with previous experiments.

Based on the knowledge acquired, the interferometric configurations will be discussed from that point. Then, the optical elements available at CSL will be listed along with their properties. For these, characterization in the visible domain will be performed to understand their behavior, e.g., beam deflection, and polarization. Following this characterization process, the most suitable components will be selected for the experiments. Finally, simulations by ray tracing will be performed to verify the theoretical feasibility of the experiments.

Per the theoretical feasibility determined, the practical implementation will be covered in depth. In particular, a methodology for the alignment of an interferometric setup will be done thoroughly. Starting from a red coherent source, and progressively shifting toward an incoherent one. In particular, a supercontinuum source, along with filters will be used.
Once aligned properly, experiments in the thermal infrared domain will be performed. As well, The difficulties and problems encountered during all these steps will be detailed.

In conclusion, a comprehensive discussion, along with a summary of the findings will be presented. Based on that, future implications and potential research in this field will be investigated.

2 | Theoretical background

This chapter provides a **theoretical background** that will be necessary for the remainder of this Master's thesis. In particular, notions of **coherence**, i.e., temporal and spatial will be presented. Along with that, a presentation of the Michelson and Mach-Zehnder **interferometers**, in addition to the **main equations** of interferometry will be addressed.

2.1 Coherence of light

The coherence of light is the constant phase relation between two waves [17]. It can be subdivided into two categories: temporal and spatial coherence. First, to understand temporal coherence, using the wave property of light, one could see wave trains of light traveling through space. For two independent wave trains, the phase difference between them is random and unpredictable, leading to no visible interference pattern. Then, it is quite obvious that each wave train has a limited duration, τ, therefore defining the coherence length, L_c, as

$$L_c = c \cdot \tau. \tag{2.1.1}$$

Where c is the speed of light. Finally, considering Heisenberg's uncertainty principle for the energy

$$\Delta E \cdot \Delta t \sim h/2\,, \tag{2.1.2}$$

such that linking the photon's energy, E, to its frequency, ν, yields

$$h\Delta\nu \cdot \tau \sim h/2\,. \tag{2.1.3}$$

Where $h = 6.626 \times 10^{-34}\ \frac{\mathrm{m^2\,kg}}{\mathrm{s}}$ is Planck's constant. Hence,

$$\tau \sim 1/\Delta\nu \overset{2.1.1}{\Rightarrow} L_c = \frac{c}{\Delta\nu}. \tag{2.1.4}$$

This spatial coherence length can then be expressed as a function of the wavelength, i.e.:

$$L_c = \frac{c}{\Delta\nu} = \frac{c}{\frac{c\Delta\lambda}{\lambda_0^2}} \Rightarrow L_c = \frac{\lambda_0^2}{\Delta\lambda}. \tag{2.1.5}$$

Where λ_0 is the central wavelength, and $\Delta\lambda$ is the bandwidth of the spectrum.
In the case of an interferometer, if the optical path lengths are not equal within the coherence length, i.e., if the optical path difference is larger than the coherence length, independent wave trains will superimpose. Hence, no interference pattern will be observable.

Concerning spatial coherence, it is directly linked to the fact that real sources are not point sources, even for lasers or distant stars. Therefore, the wavefronts emanating from different parts of the source are not correlated, i.e., their phase relation is random. Hence, the light waves interfere with each other, resulting in a loss of spatial coherence over relatively short distances. The coherence length in this case is given by

$$L_{c,\mathrm{spat}} \approx \frac{\lambda R}{D}. \tag{2.1.6}$$

Where R is the distance from the source to the observation point, and D is the diameter of the source. Thus, the spatial coherence length is a measure of how far apart points can be while still having significant coherence.

Since the three-dimensional recording is based on the interference between the object's field and the reference optical field, it emphasizes the essential role of coherence in the holographic principle. However, this reliance on coherence poses a significant challenge, limiting the broad application of holography. Specialized illumination sources, such as lasers, become necessary, and optical configurations are constrained, consequently. This constraint highlights the ongoing need for advancements to broaden the scope of holographic applications [18].
Nevertheless, several principles have been proposed since early in the development of analog holography to record holograms using incoherent sources [19]. Indeed, low coherence sources can be used in interference microscopy or digital holography for phase microscopy of thin objects. In such a case, the object field is coherent within the coherence length [20].

2.2 Common path interferometers

The common path interferometers of interest are the Mach-Zehnder and the Michelson.
Starting with Figure 2.2.1, the Michelson interferometer uses a beamsplitter that divides the incoming light beam into two paths. One of the newly created beams is directed onto a fixed mirror, while the other one travels to a movable mirror. Both mirrors will reflect the beams towards the beamsplitter, which will combine them, thus creating an interference pattern that can be recorded. This renders the alignment of such an interferometer easier since the components have few degrees of freedom. It is indeed easy to understand that if the beamsplitter's and first mirror's positions are fixed, only the second mirror can move. A difficulty for such a setup is that if the beamsplitter is not a pellicle, i.e., with zero thickness, but is a parallel plate, a compensating plate must be used to adjust the optical path length accordingly. In the visible domain, beamsplitter cubes are used such that the compensator is not required. In comparison, in the thermal infrared range, there is no such pellicle beamsplitter or beamsplitter cube, because they are more complex to manufacture. Instead, one can find beamsplitter plates with a given thickness, with or without wedges, inducing an optical path difference that must be accounted for.

In particular, Figure 2.2.1a shows the paths or the transmitted and reflected beams. It is clear that the transmitted beam has a slightly longer path than the reflected one, due to the beamsplitter's thickness. On the other hand, as depicted in Figure 2.2.1b, the compensating plate induces an additional path length in the reflected beam's path, thus rendering both transmitted and reflected paths equal.

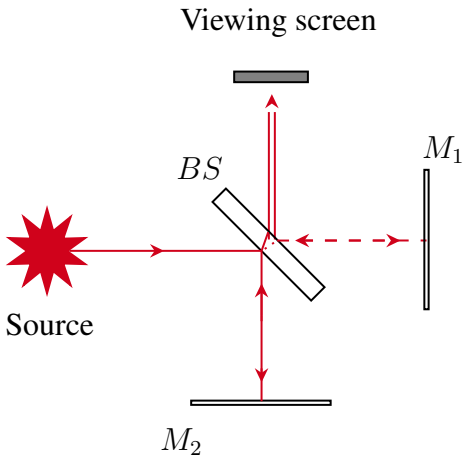

(a) Michelson interferometer without compensating plate.

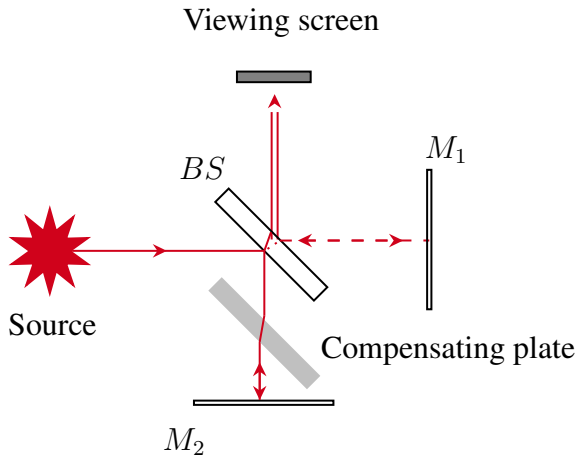

(b) Michelson interferometer with a compensating plate.

Figure 2.2.1: Michelson interferometer. The dashed and plain lines indicate the transmission and reflection, respectively. The shaft line indicates the combined beam. The transmission and reflection from the mirrors to the source were ignored.

The Mach-Zehnder interferometer also employs a beamsplitter to divide the incoming beam into two paths. However, each beam then travels toward separate mirrors before being recombined at a second beamsplitter, as shown in Figure 2.2.2. This configuration, compared to Michelson's, enables greater flexibility for path length adjustment. However, this also increases the complexity of the setup as more degrees of freedom are present.

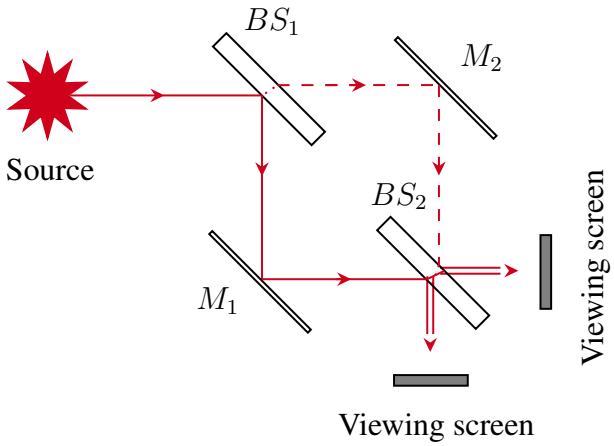

Figure 2.2.2: Mach-Zehnder interferometer. The dashed and plain lines indicate the beam traveling through the first and second arm, respectively. The shaft lines indicate the recombined beams.

In both cases, the obtained pattern reveals information about the phase difference between the two beams, i.e., it is a measure of the phase shifts due to the changes in the optical path lengths of each arm of the interferometer. From here, it is quite clear that in the infrared

domain, where plate beamsplitters are used, the Mach-Zehnder allows more flexibility without requiring any compensating plate.

2.3 Fundamental equations of interferometry

Assuming two monochromatic light waves with the same wavelength and a phase shift $\Delta\phi$, the electric fields are given by

$$\begin{cases} E_1(t) = E_{01}\,\cos(\omega t) \\ E_2(t) = E_{02}\,\cos(\omega t + \Delta\phi) \end{cases} ; \tag{2.3.1}$$

where t represents the time, ω, E_{01}, and E_{02} represents the angular frequency and the amplitude of the waves, respectively. When these waves interfere with one another, the resulting electric field (see Appendix for details) is the sum of each electric field such that

$$\begin{aligned} E(t) &= E_{01}\,\cos(\omega t) + E_{02}\,\cos(\omega t + \Delta\phi) \\ &= [E_{01} + E_{02}\,\cos(\Delta\phi)]\,\cos(\omega t) - [E_{02}\,\sin(\Delta\phi)]\,\sin(\omega t)\,. \end{aligned} \tag{2.3.2}$$

Hence, defining

$$\begin{cases} E_x &= E_{01} + E_{02}\,\cos(\Delta\phi) \\ E_y &= -E_{02}\,\sin(\Delta\phi) \end{cases} \tag{2.3.3}$$

finally yields

$$E(t) = E_x\,\cos(\omega t) + E_y\,\sin(\omega t)\,. \tag{2.3.4}$$

Since the intensity of a wave is proportional to the square of its electric field, such that it is of interest to write

$$E^2(t) = E_x^2\,\cos^2(\omega t) + 2E_xE_y\,\cos(\omega t)\sin(\omega t) + E_y^2\,\sin^2(\omega t). \tag{2.3.5}$$

Therefore, developing the electric field yields

$$E^2(t) = \frac{E_x^2 + E_y^2}{2} + \frac{\left[E_x^2 - E_y^2\right]\cos(2\omega t) + 2E_xE_y\,\sin(2\omega t)}{2} \tag{2.3.6}$$

which can be averaged with respect to time such that

$$\langle E^2(t)\rangle = \frac{E_x^2 + E_y^2}{2}\,, \tag{2.3.7}$$

since $\cos(\omega t)$ and $\sin(\omega t)$ averaged over one period are zero.

Therefore, using Equation 2.3.3 directly yields

$$\langle E^2(t)\rangle = \frac{E_{01}^2 + 2E_{01}E_{02}\,\cos(\Delta\phi) + E_{02}^2}{2}. \tag{2.3.8}$$

And since

$$\begin{cases} I_1 & \propto E_{01}^2 \\ I_2 & \propto E_{01}^2 \\ I & \propto E^2 \end{cases}, \tag{2.3.9}$$

One directly gets

$$I = I_1 + I_2 + 2I_1 I_2 \cos(\Delta\phi). \tag{2.3.10}$$

From the expression of the intensity, it is possible to derive the contrast of the fringes that will be observed. Indeed, the contrast, or visibility, is given by

$$V = \frac{I_{\max} - I_{\min}}{I_{\max} + I_{\min}}. \tag{2.3.11}$$

Where $I_{\max}$ and $I_{\min}$ are the maximum and minimum intensities such that

$$\begin{cases} I = I_{\max} \iff \cos(\Delta\phi) = 1 & \text{i.e., no phase difference;} \\ I = I_{\min} \iff \cos(\Delta\phi) = -1 & \text{i.e., phase difference of } \pi. \end{cases} \tag{2.3.12}$$

Such that

$$\begin{cases} I_{\max} = I_1 + I_2 + 2I_1 I_2 \\ I_{\min} = I_1 + I_2 - 2I_1 I_2 \end{cases}. \tag{2.3.13}$$

Hence,

$$V = \frac{2\sqrt{I_1 I_2}}{I_1 + I_2} \in [0; 1]\,. \tag{2.3.14}$$

However, in practice some noise, n, can be present such that

$$V = \frac{2\sqrt{I_1 I_2}}{I_1 + I_2 + n} < 1. \tag{2.3.15}$$

Therefore, as depicted in Figure 2.3.1, fringe visibility is reduced.

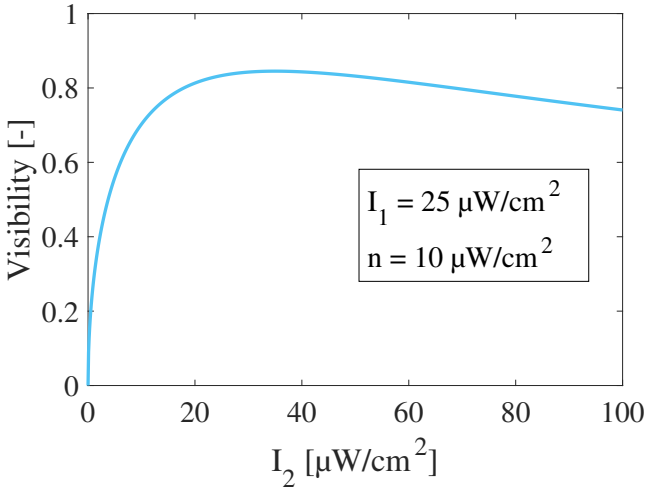

Figure 2.3.1: Degradation of the fringe visibility due to noise considering arbitrary I_1 and n in Equation 2.3.15.

3 | State-of-art of low-coherence holography

This chapter discusses holography applied to **light-in-flight** recording, covering principles and critical experiments in this topic. It looks at ultrashort pulses as a tool for creating dynamic images of light propagation, with milestones in 1978 and 1983. The critical experiments listed include the three-dimensional shapes of moving objects and the imaging of transparent objects through scattering media. The chapter elaborates further on the holography with **Mach-Zehnder** and **Michelson interferometers** and demonstrates processes for recording both **visible** domain and **infrared** domain holograms. It further elaborates on the new developments in full-color holographic image capturing along with radiometric temperature measurements. The chapter ends with insights into the **relevant work at CSL** aimed to further develop holographic techniques in **incoherent light** and bring greater accuracy to holographic imaging.

3.1 Light-in-flight

Light-in-flight recording by holography is based on the use of ultrashort pulses to produce a moving picture of the propagation of light. In 1978, the first light-in-flight recording by holography was performed using a laser with a short coherence length as a substitute for a short pulse length. It was not before 1983 that an experiment with short pulses was performed. It was therefore possible to measure temporal and spatial pulse shape, to record the single pulse during the time it was reflected by a mirror. Moreover, it was even possible to measure the three-dimensional shape of a propeller during rotation and a living human hand! Figure 3.1.1 shows a propeller illuminated from the divergent beam of the laser at A, which produces one single pulse. The reference pulse is then reflected by the two mirrors, M1 and M2, toward the hologram plate, H. Compared to what is shown in the drawing, the distance between H and C is much greater.

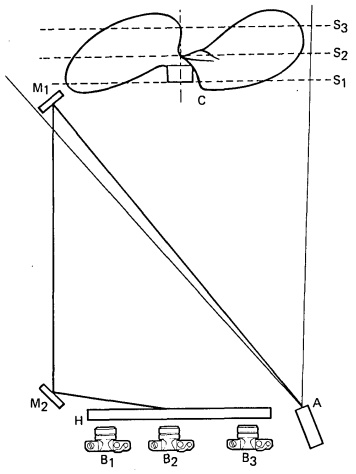

Figure 3.1.1: Schematic view of the holographic setup used to produce the contouring of a fan [21].

Using a setup similar to the one used for the fan, a human hand was contoured. (3.1.2a) The light sheet from one single pulse touches the back of the hand and has just at this moment reached the knuckles. (3.1.2b) Some 100 picoseconds later, the light has moved three centimeters further into the hand. (3.1.2c) Still another 100 picoseconds later, the light sheet just touches the wristwatch recording the time when the 13 picoseconds pulse passes the watch.

(a) (b) (c)

Figure 3.1.2: Coutouring of a human hand using a setup similar to the one present in Figure 3.1.1 [21].

The method was used as a gated viewing device to look through a scattering medium. It was, therefore, possible to see profiles of transparent objects hidden between two ground glasses, by studying only the part of the single pulse that arrived first, i.e., the one that traveled the shortest path. Figure 3.1.3 shows an object, O, placed between two ground glass plates, A and B. The single pulses from the laser, L, were divided by the beamsplitter, M1, into an object pulse and a reference pulse. The object beam illuminates the back plate, B, after it is first diverged by the negative lens, N. On the other hand, the diffuse light passes through the object and then through the front plate, F, to the hologram plate, H, which is also illuminated by the reference pulse, R. The wavefront of the light that went straight from B to H is represented by W. M2, M3, and M4 are mirrors.

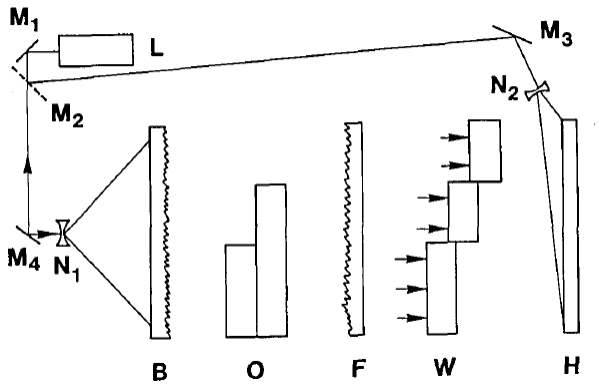

Figure 3.1.3: Holographic setup to image transparent objects between two ground glasses [21].

Figure 3.1.4a shows light that arrives first producing a shadow of the Plexiglas object. (3.1.4b) 20 picoseconds later, the light arrives that has passed through one layer of Plexiglas. (3.1.4c)

After sill another 20 picoseconds, the light arrives that has passed the two layers of Plexiglas. (3.1.4d) When the short laser pulse was replaced by continuous light, nothing of the object's shape could be seen on the ground glass.

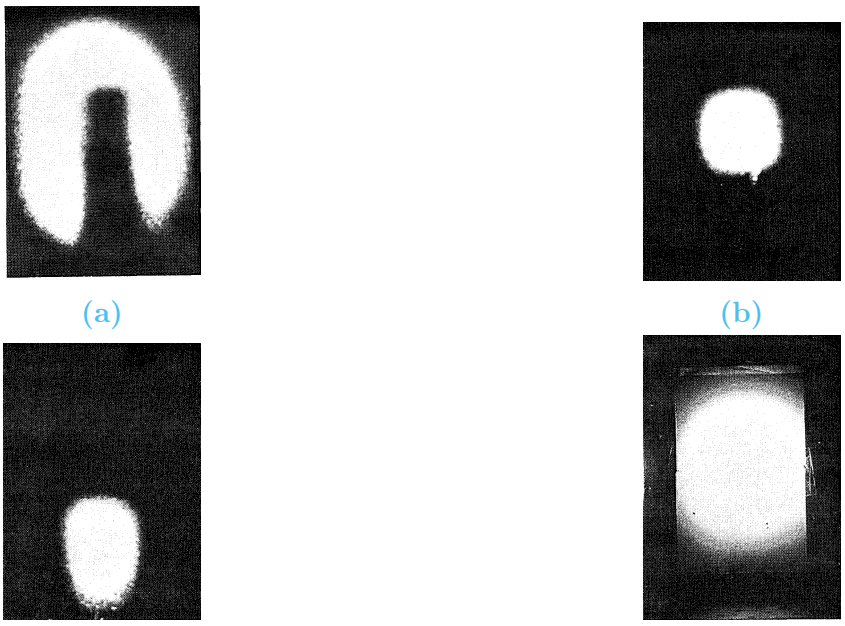

(a) (b) (c) (d)

Figure 3.1.4: Temporal progression of light passing through layers of Plexiglas and the resulting shadows and comparison with a continuous light source. The setup used was the one presented in Figure 3.1.3 [21].

The experiment of Abramson illustrates well the principle of coherence gating which was used later on by many other groups.

3.2 Holography in the visible domain using the Mach-Zehnder interferometer

Giancarlo Pedrini et al., describe how a pinhole, located far from the image plane, produces a spherical wave containing contributions from all object points, using a Mach-Zehnder setup. The interference of the image point and the waves from the pinhole creates a Fresnel zone with fringe density related to the three-dimensional position of the image point [22]. Several trade-offs, such as the one between spatial coherence and intensity are analyzed. In particular, a smaller pinhole increases spatial coherence, while being detrimental for the intensity. This problem requires the use of a density filter on the other arm to balance the contrast of the fringes. The holographic reconstruction process uses phase shifting, the combination of intensity patterns and phase maps, to facilitate digital wavefront propagation at different planes. Figure 3.2.1 shows the recording arrangement, where BS1 and BS1 are beamsplitters, M1 and M2 are mirrors, NDF is a neutral density filter, and PH is a pinhole.

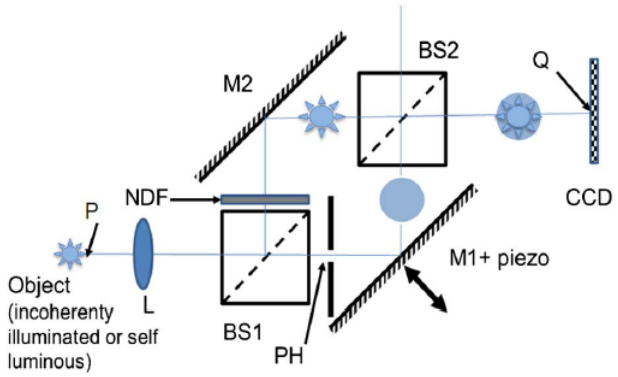

Figure 3.2.1: Experimental setup for hologram recording for incoherently illuminated or self-luminous object [22].

Concerning the lens, L, it is used to focus the object beam right before the CCD, while the reference beam is extended and larger than the object beam, as depicted in Figure 3.2.2. The goal of having the object's focus before the CCD is to get a *larger* object in the detector plane, otherwise, it would alter visibility. It is also worth noting that the position of the lens greatly influence the object seen on the CCD, i.e., the object might be defocused.

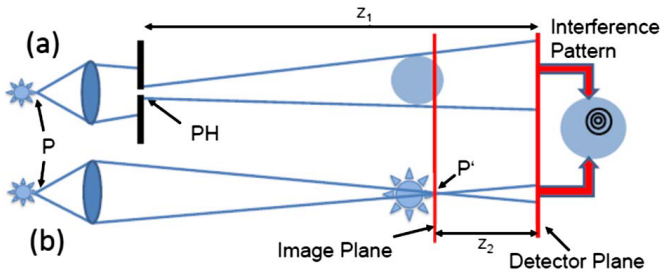

Figure 3.2.2: Propagation of the wave emitted by point P through the two arms of the interferometer, with (a) and without (b) the PH [22].

Figure 3.2.3(a) shows a defocused image of one part of the emitter (0.52 mm × 0.38 mm), recorded by the CCD when one arm of the interferometer was closed. When the path lengths are adjusted and the light goes through both arms, an interference pattern shown in Figure 3.2.3(b) including the intensity profile along the recorded fringes is obtained. One of the mirrors (M1) is mounted on a piezoelectric device in order to apply the phase-shifting technique and extract the phase. Figure 3.2.3(c) shows the phase obtained by applying phase shifting. In the phase map, it is possible to observe straight fringes where the object does not contain high spatial frequencies (homogeneous), but at the edges of the object, these fringes are curved and contain information useful for holographic reconstruction. By combining the intensity pattern [Figure 3.2.3(a)] and the phase map [Figure 3.2.3(c)], a wavefront that can be digitally propagated at different planes is built. The digital reconstruction of the wavefronts by using both the amplitude and phase is shown in Figure 3.2.3(d)-(f). By physical focusing, the image obtained is shown in Figure 3.2.3(g), and finally, the best reconstruction obtained using only the intensity is presented in Figure 3.2.3(h).

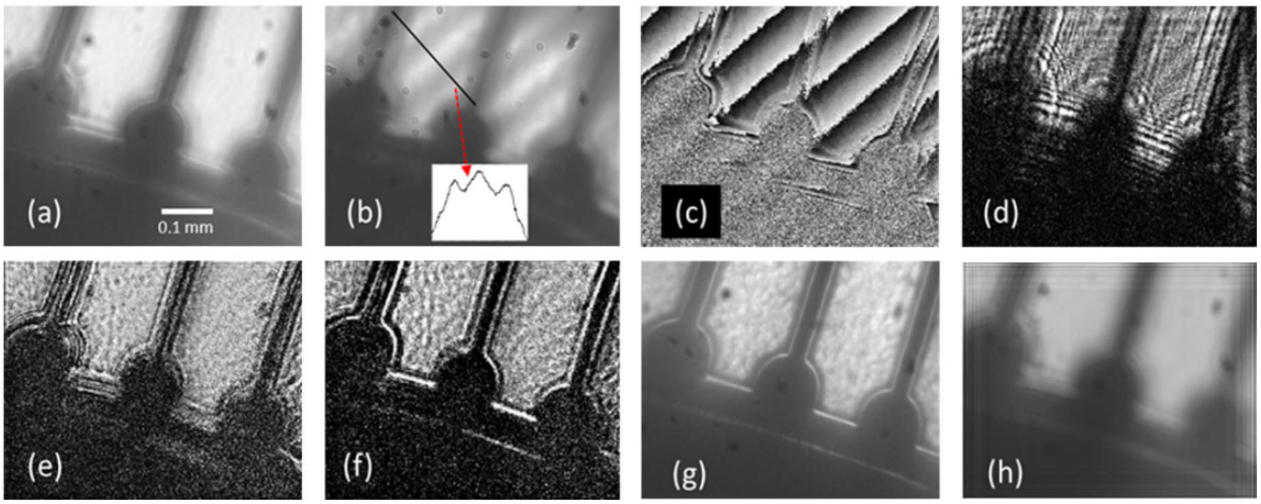

Figure 3.2.3: Obtained results and reconstruction using the experimental setup presented in Figure 3.2.1 [22].

In summary, it has been shown that it is possible to get digital wavefront reconstructions of self-luminous objects by using a setup based on digital in-line holography. The advantage of this approach is that the reference wave is produced in a very simple way by introducing a PH in one arm of a Mach–Zehnder interferometer and there is no need to use expensive elements. The setup can be used to reconstruct the wavefront of small (microscopy) or large objects (astronomy). The digital reconstruction of such wavefronts is of great importance since incoherent wavefronts are the most common in nature. The disadvantage is that a neutral density filter needs to be introduced in the interferometer in order to compensate for the low intensity of the reference. This problem can be solved by using pixelated cooled CCD or CMOS detectors having a dynamic range of 14 bits or higher allowing the recording of the low-modulated interferograms produced when the reference is weaker with respect to the object beam. It is of course possible to insert other elements instead of the PH in one arm of the interferometer, e.g., a lens that slightly changes the curvature of the wavefront; the advantage of the PH is that it produces a perfect spherical wavefront and thus simplifies the evaluation [22].

The technique of spectrally resolved incoherent holography, as a follow-up of initial experiments conducted by the same group presented above, involves recording holograms of incoherently illuminated objects and using self-referencing schemes. The hologram is created by interfering the light from the object with a portion of the same light that has followed a slightly different path. For this approach, interference patterns from each point on the object are incoherently added. Temporal coherence is then enhanced, or specific wavelengths are selected by introducing spectral filters. The Mach-Zehnder interferometer used introduces both variable time delay and radial shear between the interfering optical fields to measure spatial and temporal coherence functions. This, in turn, allows the recording of three-dimensional spectral and spatial information. Indeed, three spatial dimensions and one spectral dimension are resolved without resulting to tomography.

Concerning the variable time delay, it is achieved through a mirror mounted on a piezo-electric transducer (PZT). The mirror can then be shifted, resulting in a non-uniform path delay, leading to distorted spectra in object reconstruction. Finally, the Van-Cittert-Zernike theorem, for spatial coherence, and the Wiener-Kintchine theorem, for temporal coherence, highlight the importance of coherence to maintain resolution and prevent destructive interference. The full setup is presented in Figure 3.2.4

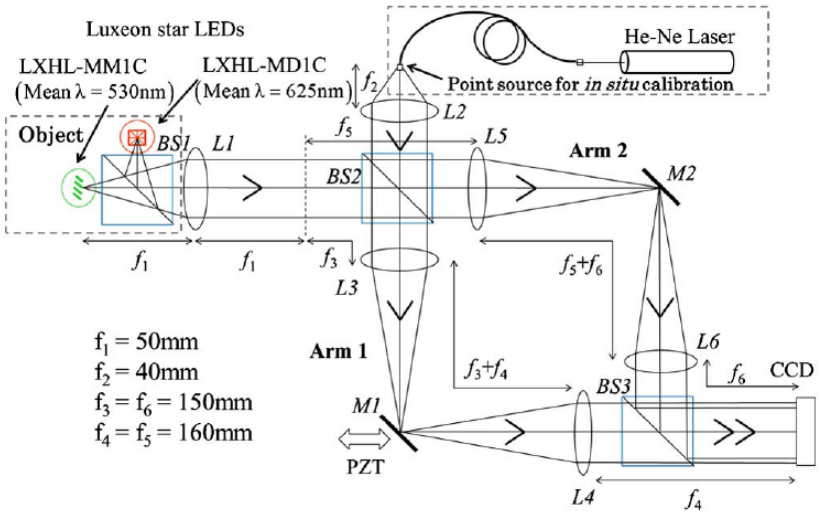

Figure 3.2.4: Experimental setup for the recording of a spectrally resolved incoherent-object hologram [23].

A polychromatic object, i.e., the toy aircraft shown in Figure 3.2.5 was used for the experiment.

Figure 3.2.5: Polychromatic toy aircraft used as the object [23].

This object was then successfully reconstructed. In particular, Figure 3.2.6 presents the combined images of amplitude and phase for λ = 625, 530 and 450 nm (a)-(c). In (a) the point source from the He-Ne laser used for calibration was kept masked.

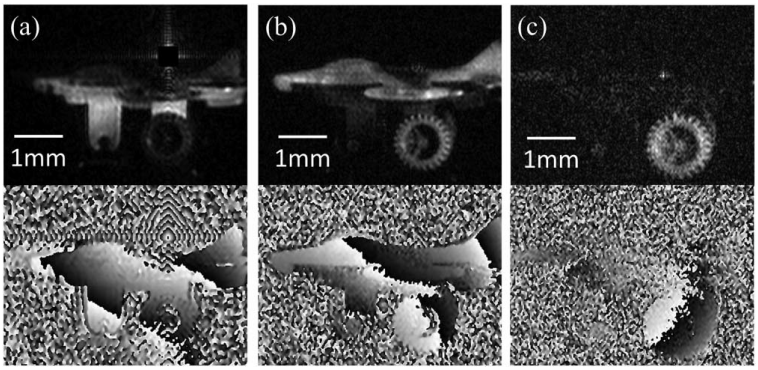

Figure 3.2.6: Reconstruction of the toy aircraft [23].

3.3 Holography in the visible domain using the Michelson interferometer

The setup presented in Figure 3.3.1 comprises a beam-splitting cube and two mirrors with different curvatures. One mirror is a curved mirror to introduce a differential curvature between the two copies of the object field, while the other is a plane mirror mounted on a piezo-actuator for phase shifting. It also consists of three lenses, the first two act as a telescope, collecting and directing light of the object towards the setup. The third one is placed in front of the CCD, which enables the adjustment of magnification and field of view.

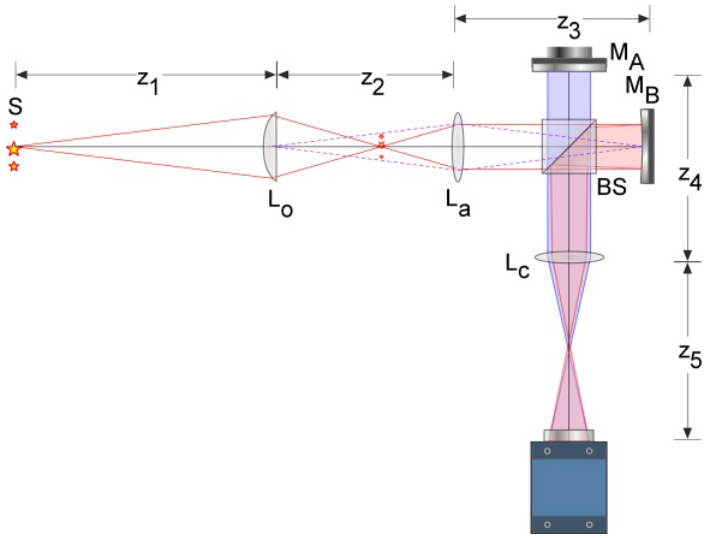

Figure 3.3.1: Setup for the full-color self-interference incoherent digital holography. L's are the lenses, M's the mirrors, and BS is the beam splitting cube [18].

The beamsplitter divides the incoming light from the object into two different paths. The copies of the object are slightly different due to the curvature in one of the mirrors. These copies will then interfere, thus producing a Fresnel zone pattern, recorded by the CCD. Additionally, the piezo-mounted mirror is dithered in order to eliminate incoherent background

noise. As the phase shifts, the CCD records multiple frames of the interference pattern, these frames are then combined to obtain the hologram for each color channel (Red - Green - Blue). The results are shown in Figure 3.3.2. In particular (A) shows the amplitude and phase of the hologram for the red channel. In (B), the numerically focused images from the hologram for the three color channels are shown. (D) represents the full-color focused image, and (E) the full-color image at distances of 20 and 40 mm before and after the best focus, i.e. at 60 mm. (C) corresponds to an image of the scene taken with a cellphone, it is used for comparison.

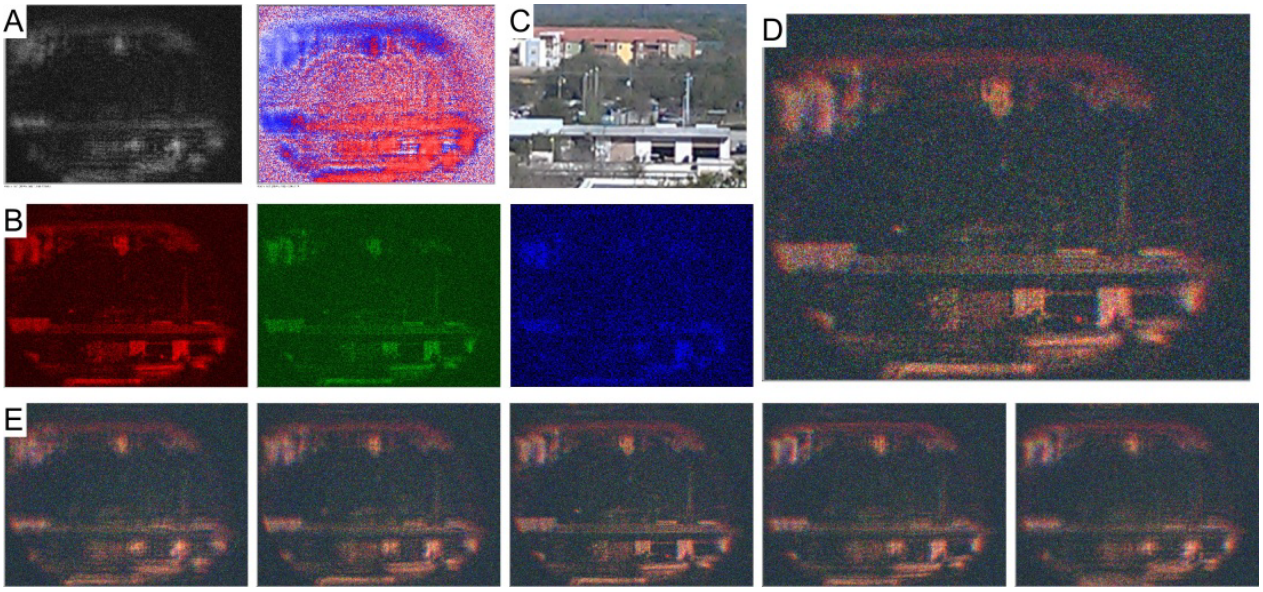

Figure 3.3.2: Full-color self-interference incoherent digital holography of an outdoor scene under clear daylight illumination [18].

This experiment fully demonstrates the ability to capture full-color holographic images. Moreover, the reconstructed images show clear 3D formation. The focus can be adjusted to different parts of the scene by numerically adjusting the reconstruction distance.

3.4 Holography in short-wave infrared using the Michelson interferometer

Similarly to the experiment of Kim Myung ([18]), Masatoshi Imbe provides a working setup to create holograms in the infrared domain ($\lambda \approx 1550$ nm). In particular, the setup depicted in Figure 3.4.1 shows that a Michelson interferometer, with a single lens in this case, is used.

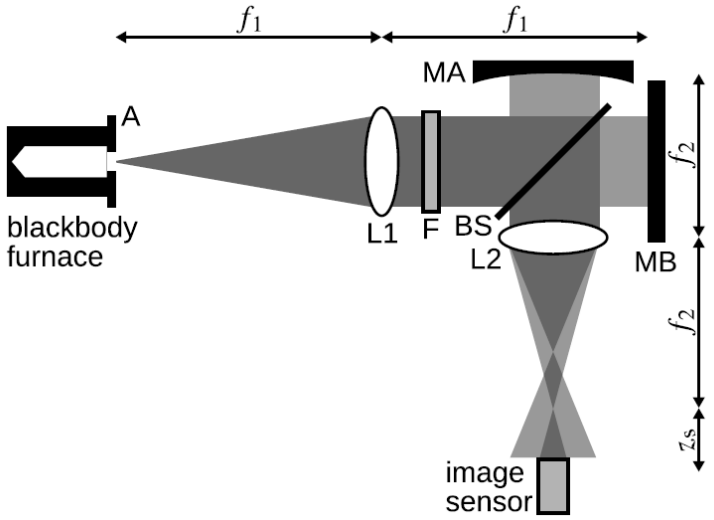

Figure 3.4.1: Schematic diagram of optical setup used in the experiment: L1, L2, lenses; MA, MB, mirrors; BS, beamsplitter; F, bandpass filter; A, aperture [24].

The 3D radiometric temperature measurement, using incoherent digital holography was performed using a blackbody furnace as an object, emitting thermal radiation which can be captured with an InGaAs array sensor. This same furnace was also used as a reference radiator for calibration of the optical system. During this calibration, holograms of the objects were recorded at different temperatures (550 °C, 625 °C, and 700 °C), and then, the reconstructed images were analyzed to determine various calibration parameters. Using these parameters, the temperature distribution of the object at known distances was measured. Nevertheless, when the object is moved to different distances, discrepancies in measurements arise, as shown in Figure 3.4.2. This potentially indicates that the optical elements are misaligned, or that there is residual background interference.

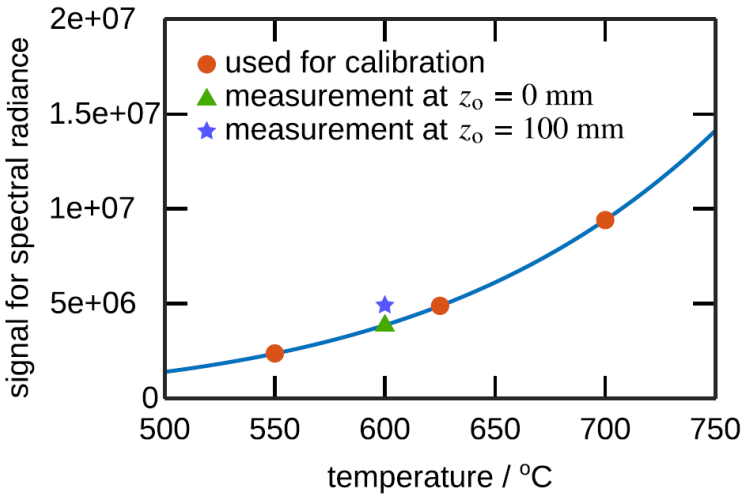

Figure 3.4.2: Calibration curve calculated using calibration parameters. The plots show the signals obtained in the experiment [24].

The potential misalignment of the optical elements could lead to fluctuations in solid angles at different distances, thus affecting the measurements. Residual background and variations in the dark noise of the image sensor could also contribute to the discrepancies. In addition to that, there might also be issues related to the detection wavelength and non-linearity of the sensors, thus affecting the accuracy of the measurements.

Figure 3.4.3(a) and (b) shows the spectral radiances for a temperature of 600°C, at a distance of 322 and 347 mm, respectively. (c) and (d) show the corresponding temperature images. Hence, while the experiment demonstrates the feasibility of incoherent digital holography for radiometric temperature measurements, improvements must be made to enhance the accuracy of the method.

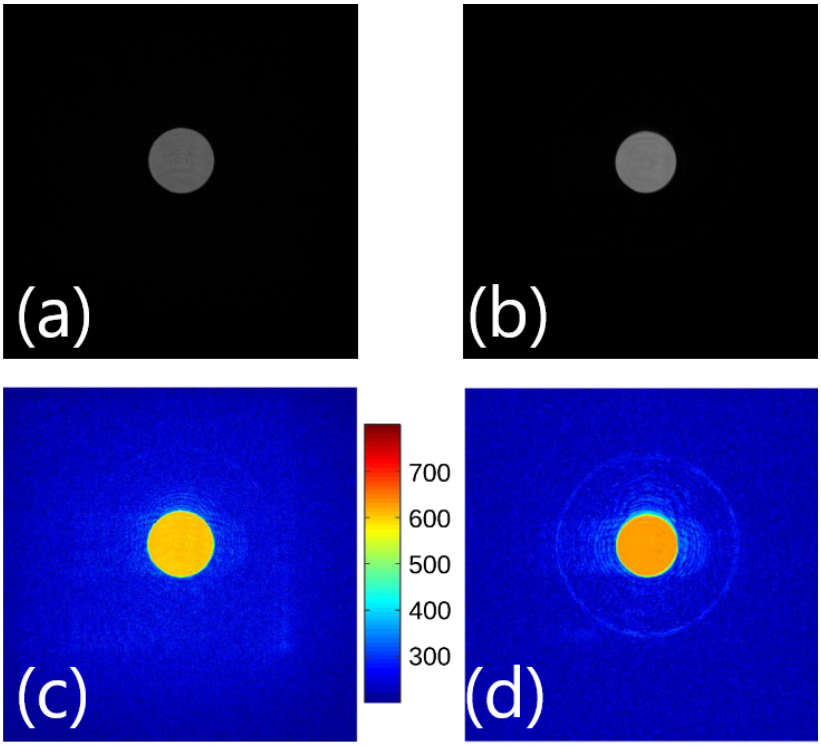

Figure 3.4.3: Images of spectral radiances for a temperature of 600 °C at a distance of 322 mm (a) and 347 mm (b) along with the temperature images (c) and (d) [24].

3.5 Work in the visible domain at CSL

Based on Pedrini's experiment ([22]), preliminary work was performed at CSL by Sarah Muzard, a student of SupOptique France, during a few weeks of internship. In particular, it involved the Mach-Zehnder setup, in incoherent white light, as shown in Figure 3.5.1. She also put in place a LWIR Mach-Zehnder setup, from which she managed to obtain fringes. However, no alignment process was depicted in the official report. In addition to that, the setup was unexpectedly dismantled by accident and there was no trace at all of the results she obtained, except the visual appreciation of her internship supervisor, Marc Georges. It

is precisely the aim of the current work to have an advanced step-by-step procedure for the alignment of an incoherent self-emitting LWIR interferometer.

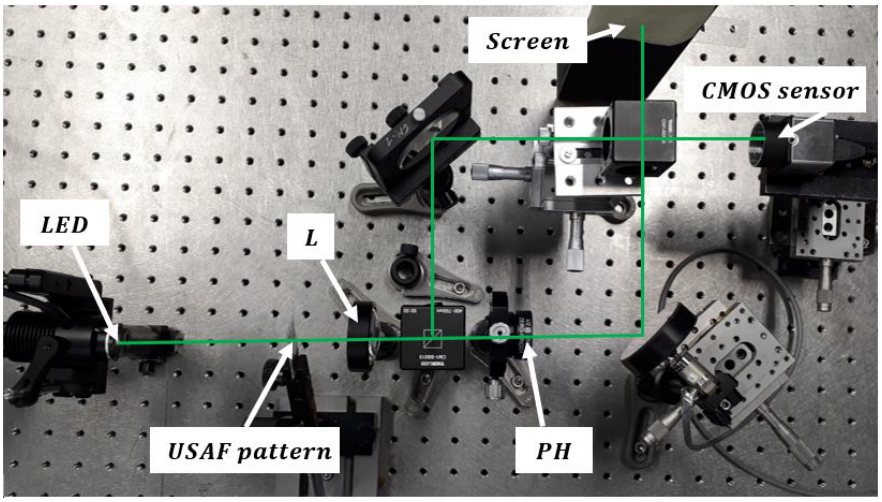

Figure 3.5.1: Experimental Mach-Zehnder setup for holography in white incoherent light [25].

This experiment proved to work to produce fringes, as well as holograms, as shown in Figure 3.5.2. In particular, (a) shows the defocused image of the object, (b) the interference pattern due to the superposition of the two arms, (c) the best reconstruction obtained by using only the intensity, (d) - (f) the digital reconstruction by using both amplitude and phase for numerical propagation.

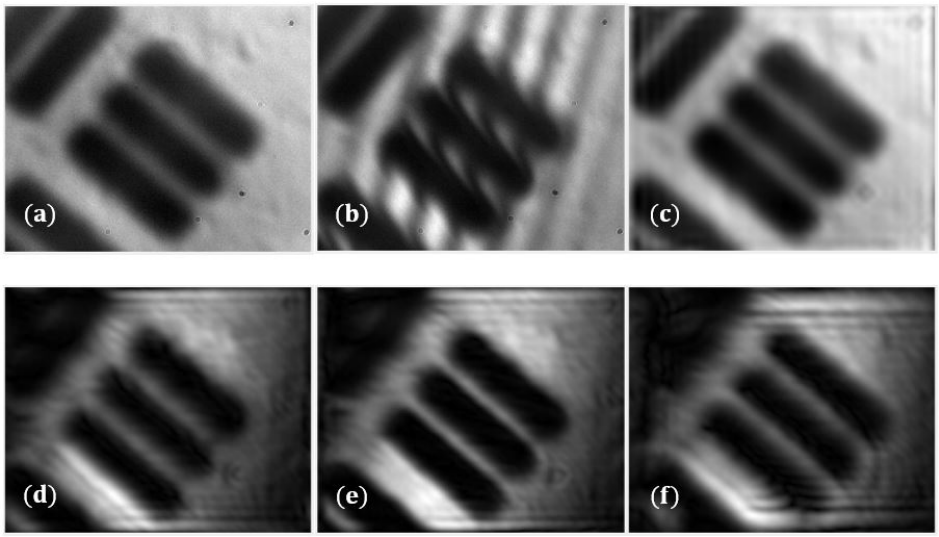

Figure 3.5.2: Obtained results and reconstruction using the experimental setup presented in Figure 3.5.1 [25].

4 | State-of-art of low coherence holography by self-emission

This chapter covers techniques and principles for achieving **holography using low-coherence infrared sources**. In particular, **self-emitting** thermal **sources**. First, **Planck's law** for black bodies and wavelength considerations are explored. This provides an understanding of self-emission in the infrared domain.

The focus then shifts to the thermal infrared, in particular in the 7-14 μm range, and the use of a CO_2 laser for coherent illumination. This is done by examining the **contribution of Marc Georges and Jean-François Vandenrijt** at CSL, in metrology and non-destructive testing. As well, Ferraro's work on viewing through smoke and flames will be analyzed.

Finally, the **research of this Master's thesis** on thermal infrared holography using **incoherent self-emission** will be presented. This approach should effectively eliminate the need for external coherent illumination, thus opening new possibilities in this field.

4.1 Planck's law for black bodies and wavelength considerations

It is first important to understand how self-emission works and what a black body is. Black body radiation refers to the theoretical concept of an idealized body that absorbs all incident electromagnetic radiation without any dependency on the wavelength or angle of incidence. In thermal equilibrium, the black body emits radiation that only depends on its temperature. At a given temperature, T, and wavelength, λ, Planck's law describes the spectral radiance of the radiation emitted by the black body as follows

$$B(\lambda, T) = \frac{2hc^2}{\lambda^5} \frac{1}{e^{\frac{hc}{\lambda KT}} - 1}. \tag{4.1.1}$$

With $k = 1.3806 \times 10^{-23}$ J/K the Boltzmann's constant.

Following this, Wien's displacement law shows at which wavelength the black body emits most of its radiation, for a given temperature, as:

$$\lambda_{\max} = \frac{b}{T}. \tag{4.1.2}$$

Where $b = 2.898 \times 10^{-3}$ m K, is Wien's constant.

Hence, as the temperature increases, the peak wavelength tends to shift to a shorter wavelength.

Self-emitting sources are inherently incoherent. Indeed, they output radiation at various wavelengths. In addition to that, in thermal emission sources, photon emission is due to the random vibration of atoms and molecules within the source. These motions are chaotic by nature, therefore, this leads to a superposition of waves with varying phases and amplitudes. Hence, this chaotic motion yields radiation that lacks a fixed phase relationship, which leads to incoherence. Finally, in self-emitting sources, each photon is emitted independently with a random phase. This means that, once again, there is a lack of a fixed phase relationship between photons, leading to temporal and spatial incoherence [26]. This can be demonstrated by using Planck's (Equation 4.1.1) and Wien's (Equation 4.1.2) laws, assuming a black body. Indeed, the intensity with respect to the wavelength can be plotted as depicted in Figure 6.7.1. It can be observed that the intensity is larger than zero over a wide range of wavelengths, depending on the temperature. Therefore resulting in a short coherence length, compared to a CO_2 laser.

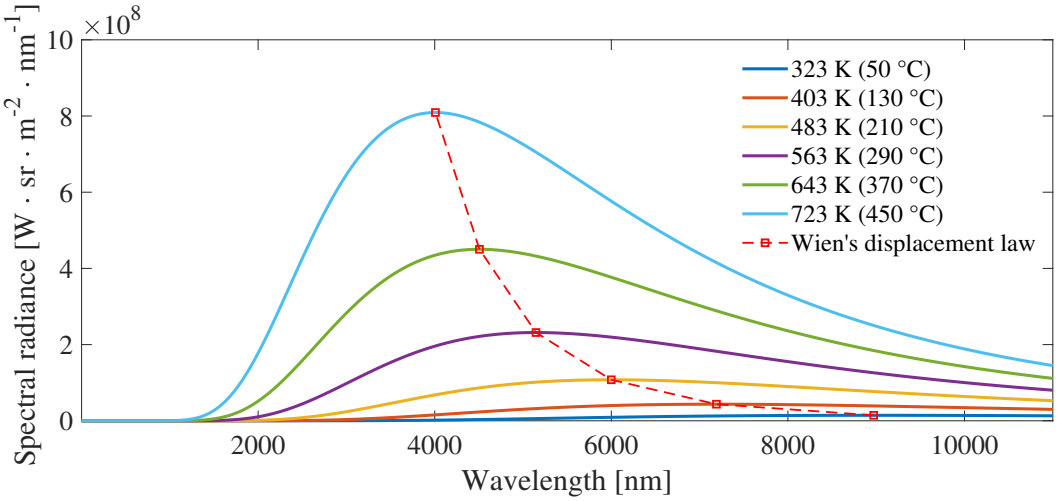

Figure 4.1.1: Spectral radiance with respect to the wavelength for a black body using Planck's law (Equation 4.1.1). Wien's displacement law (Equation 4.1.2) is also shown.

Taking as an example the curve for 450 °C, it is evident that the wavelength range covered is very large, i.e., $\lambda \in [2000; > 10000][\text{nm}]$. Therefore, some wavelength considerations must be made.

Holography can be performed in various wavelengths, however, the focus of this Master's thesis will be on the visible and infrared domains. In particular, it is necessary to define the sub-domains of the infrared. In this context, a standardized nomenclature is applied to differentiate distinct infrared spectral bands, each identified by a specific acronym corresponding to its unique wavelength range. These acronyms serve as succinct labels for categorizing various regions within the infrared spectrum:

- **NIR:** Near-Infrared;
- **SWIR:** Short-Wave Infrared;
- **MWIR:** Mid-Wave Infrared;
- **LWIR:** Long-Wave Infrared.

Figure 4.1.2 shows the wavelength range for each spectral band.

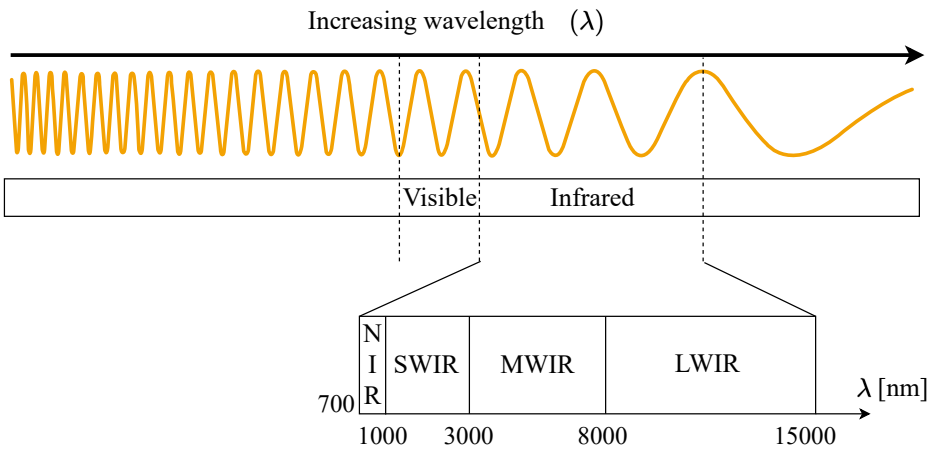

Figure 4.1.2: Infrared spectral bands.

4.2 Thermal infrared (LWIR) holography with coherent sources

Long wavelength infrared lasers, such as CO_2 lasers, allow to have interesting features while developing holography. These were advantageously used in the development of Marc Georges at the CSL and in parallel by the group of Ferraro in Italy. The first advantage is that, at long wavelengths, the stability requirements of the holographic setup are significantly reduced. Indeed, it is usually considered that the setup must be stable at a fraction of the wavelength during the whole hologram capture. Moreover, if a series of holograms is captured, for comparing their phase, stability must be ensured for long periods. Holographic experiments aiming at following the thermo-mechanical deformation of large structures, which were carried out with visible laser at the CSL, proved to be not working until switching to LWIR wavelengths. The other advantage of the work performed at CSL is that it was shown that the measurement range of phase variations was also larger than in the visible domain. This corresponds to the observation of larger deformations, which are more typical of what the space environment induces on the instruments and space platforms, due to large temperature variations. In view of metrology and nondestructive testing, two developments of the CSL will be briefly presented. Additionally presented hereafter, long wavelengths also have the ability to penetrate some gases, smoke, or even flames. Ferraro's group advantageously used this to perform holography to observe objects occluded in such circumstances.

4.2.1 Metrology and non-destructive testing

Metrology

LWIR digital holography, developed by the CSL in the frame of a European Space Agency (ESA) program, can monitor deformations (1 - 250 μm) of large space reflectors (1-4 m) during thermal cycling tests. While interferometry requires expensive and carefully aligned null-lenses, holography on the other hand uses cost-effective and off-the-shelf components.

The setup includes a laser, a camera, and components placed outside a vacuum chamber, with particular lenses allowing a beam to pass through, as depicted in Figure 4.2.1.

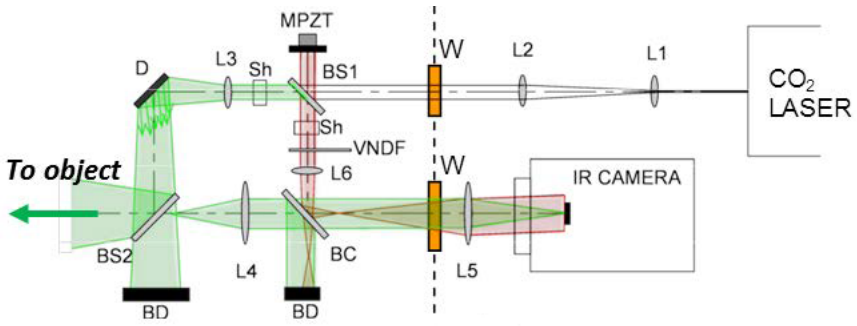

Figure 4.2.1: LWIR digital holography setup[27].

As explained in [27], the object beam reaches a diffuser D (a thick metal plate with scattering coating) which illuminates the object through BS2. The light is backscattered by the object towards the camera and is recombined with the reference beam through the beam combiner (BC). An afocal system (L4-L5) is used for placing the image plane out of the vacuum chamber. The dashed line represents the limit of the vacuum chamber with ZnSe windows (W). In the reference beam, an afocal system enlarges the beam to cover the entire sensor (L6 combined with L5 of object afocal). Sh represents a shutter, BD beam dumps, VNDF a variable neutral density filter for decreasing the reference beam intensity. MPZT is the reference mirror mounted on a piezo translator. The setup successfully measured deformations of aspheric reflectors, demonstrating its adaptability and effectiveness as shown in Figure 4.2.2.

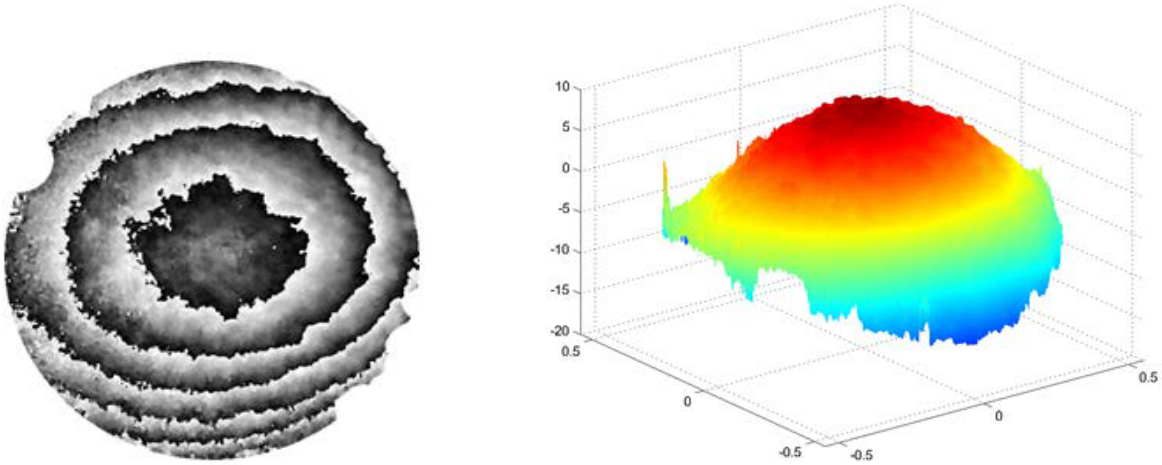

(a) phase difference due to deformation between two temperatures

(b) 3D plot of deformation after phase unwrapping of Figure 4.2.2a.

Figure 4.2.2: Obtained phase difference and 3D deformation plot [27].

LWIR digital holography was also used to measure deformations in the NIR Spectrometer and Photometer (NISP) focal plane array (FPA) for the Euclid mission. This FPA required de-

tailed deformation measurements of each detector, as well as their relative displacements [27].

To conclude, LWIR digital holography provides a cost-effective solution for deformation assessment in large space structures, or segmented FPAs. It provides high resolution and adaptability to various reflector shapes and sizes.

Non-destructive testing

In the aerospace sector, advanced techniques to enhance interferometric non-destructive testing (NDT) were developed. Compared to holographic methods, thermographic NDT methods are straightforward and provide easy-to-interpret results. Nevertheless, holography remains important as it offers unique insights into deformations, while thermography provides quick identification of defects.

A unique technique combining thermography and holography using LWIR electronic speckle pattern interferometry (ESPI) was developed at CSL. Together, these allow the capture of both temperature variations and deformations, which are of crucial importance for NDT applications.

ESPI works by recording the interference pattern obtained for a laser-illuminated object and the corresponding reference beams. However, for thermal infrared wavelength, the intensity of the recorded hologram includes both an interference pattern and an incoherent thermal background. Therefore, the goal was to capture both the object's thermal background and the phase information at each pixel. For that purpose, an image-plane holographic setup, where the thermal background corresponds to the surface temperature, was used. The combined results of the hologram and thermogram are depicted in Figure 4.2.3. In particular, the hologram or speckle-gram recorded at thermal wavelengths (a) with the thermal and interference part shown in (b) and (c).

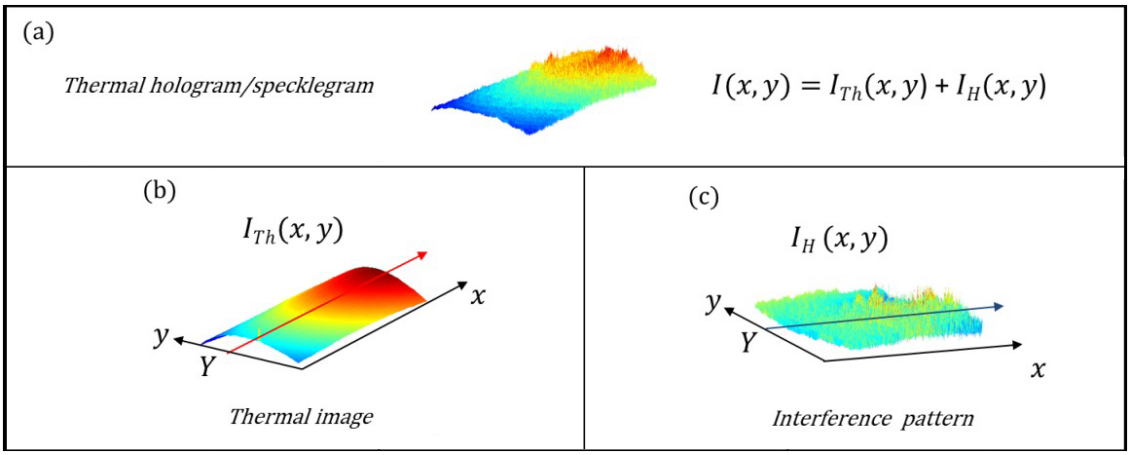

Figure 4.2.3: Combined results of the hologram and thermogram [27].

For industrial NDT applications, a mobile interferometer was developed. It consists of a lower bench with the laser and beam separation assembly, with an upper bench with the

beam combiner and thermographic camera, as shown in Figure 4.2.4.

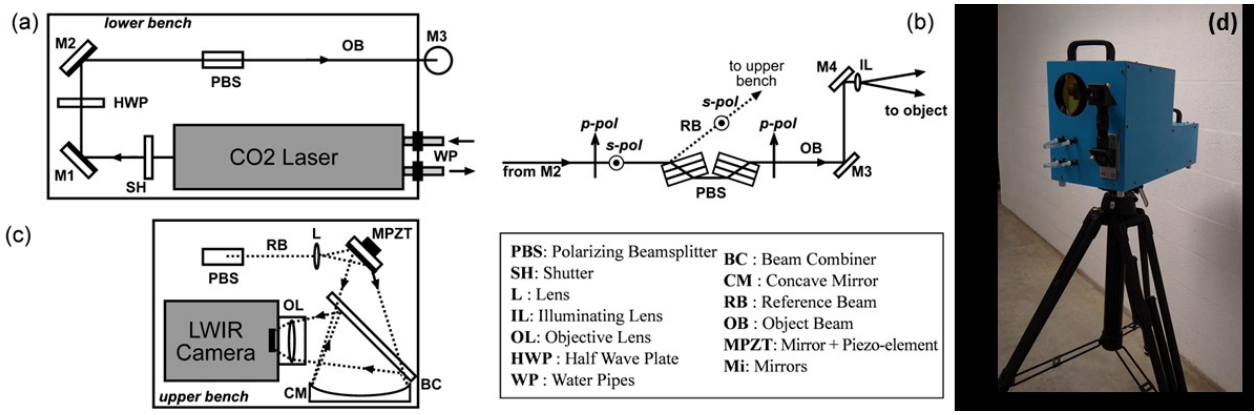

Figure 4.2.4: Sketch of the mobile LWIR speckle interferometer: (a) lower bench, (b) separation of beams, (c) upper bench, (d) mobile instrument [27].

For field testing, the instrument's use in aeronautical facilities for defect detection in large composite structures was demonstrated. Figure 4.2.5(a) shows the mobile ESPI system inspecting a fuselage. Despite workshop conditions, defect detection was successful as the phase difference shows deformation in (b), and (c) shows the thermal difference image.

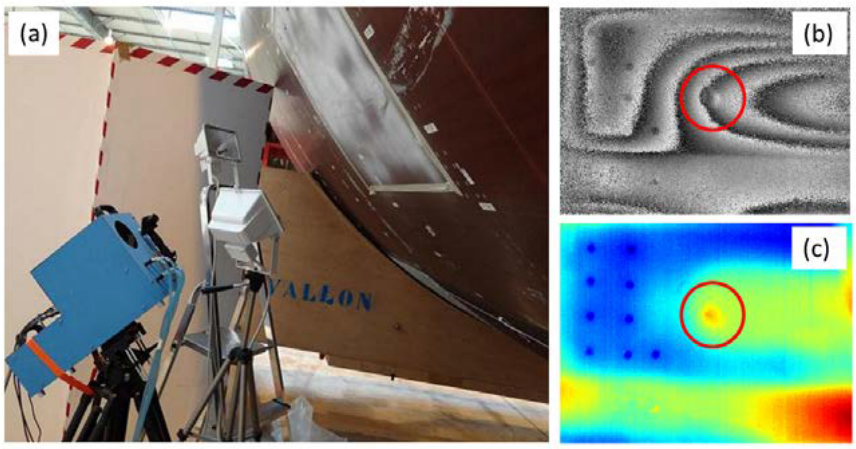

Figure 4.2.5: Observation of delamination in CFRP structure in workshop condition with the mobile LWIR system [27].

4.2.2 LWIR digital holography for imaging through smoke and flames

It was demonstrated that LWIR digital holography can capture images of objects hidden behind, or within, smoke, provided that this medium is transparent to the wavelength of the laser used. In this case, the setup involves a CO_2 laser, for which the emission lines are not absorbed by smoke, or fire. The experimental interferometric setup in lensless off-axis configuration is shown in Figure 4.2.6. It involves beamsplitters, BS, lenses, L1 and L2, a variable attenuator, VA, and two mirrors, M1 and M2.

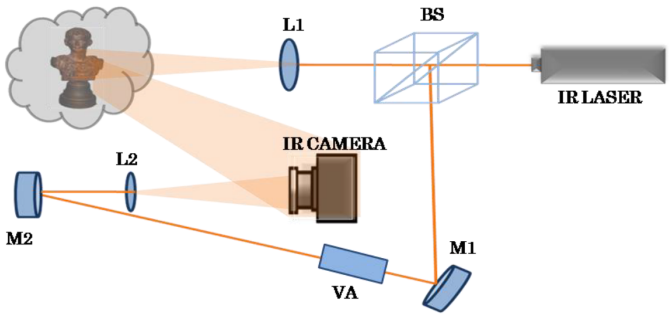

Figure 4.2.6: Experimental interferometric setup in lensless off-axis configuration [28].

This allowed for the recording of holograms and objects that are invisible to the naked eye, as depicted in Figure 4.2.7. A statuette in a Plexiglas box was filled with smoke to render it invisible to the naked eye (Figure 4.2.7(a)). The thermographic image and the one obtained by reconstructing it using digital holography are compared in Figure 4.2.7(b)-(c).

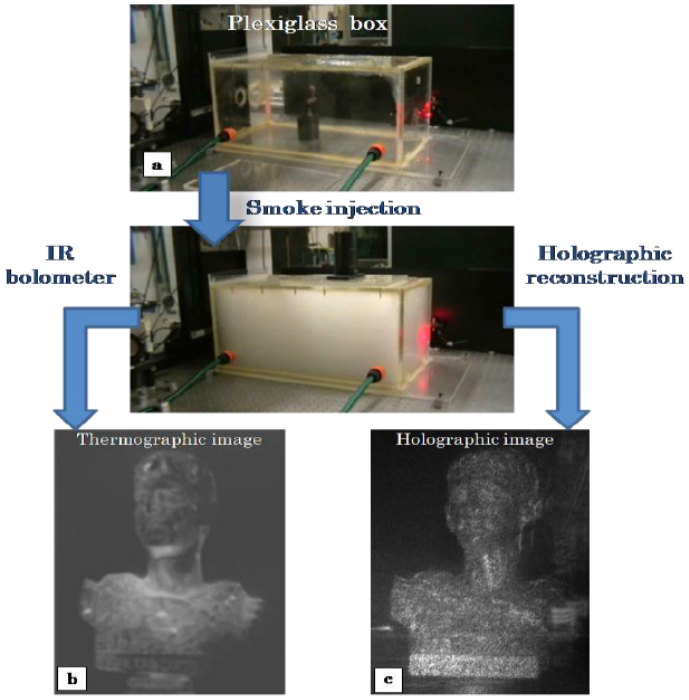

Figure 4.2.7: Experimental results of the imaging of statuette hidden by smoke [28].

In a similar experiment, objects were obstructed by flames. However, in this case, traditional thermography fails due to saturation of the sensor. However, in LWIR digital holography, this limitation is bypassed, as shown in Figure 4.2.8.

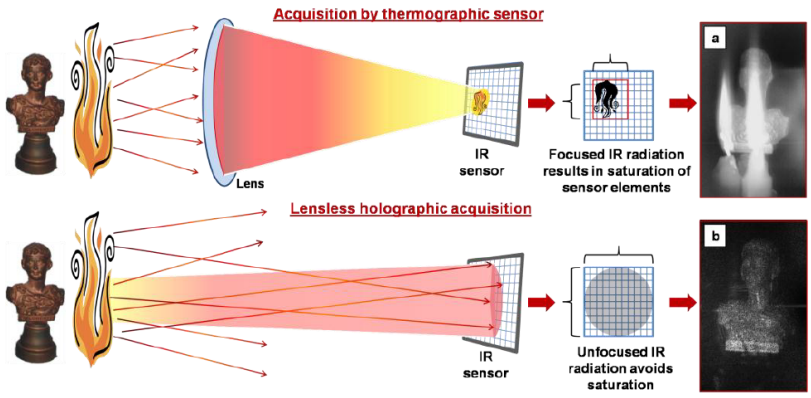

Figure 4.2.8: Imaging of a metal object seen through flames of candles [28].

Finally, Figure 4.2.9 shows that LWIR digital holography was used to image living persons through flames, which demonstrates the potential applications where conventional imaging fails. These in turn open new paths for imaging in challenging environments.

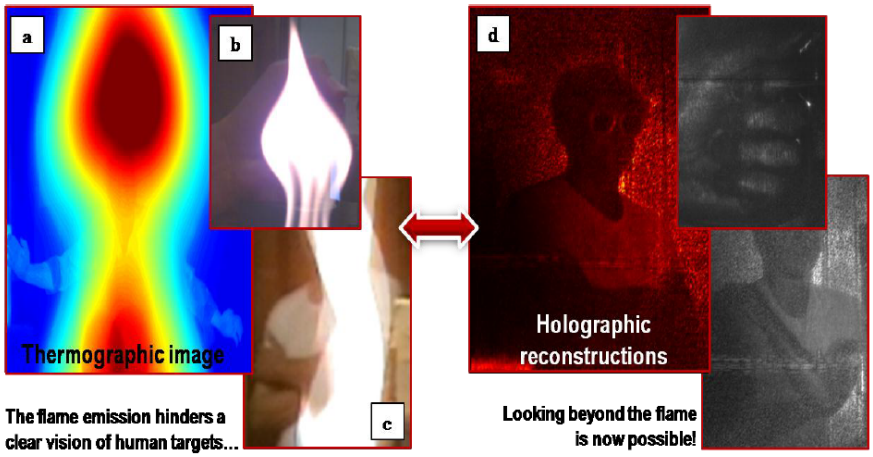

Figure 4.2.9: Imaging of a live human seen through flames [28].

4.2.3 Self-referenced setup

Recently, in view of improving their setup, Ferraro's group ([29]) developed a self-referenced setup for digital holography, shown in Figure 4.2.10(a). In the provided schematic, z and z' correspond to the object and image distance, respectively while d represent all positive distances between optical elements. L are the one-inch diameter doublets, L_{sph} and L_{pl} correspond to spherical and plane mirrors, BS are the beamsplitters, and CAM is the camera, along with the interference filter SF. Figure 4.2.10(b) shows a detail of the L_2 camera space.

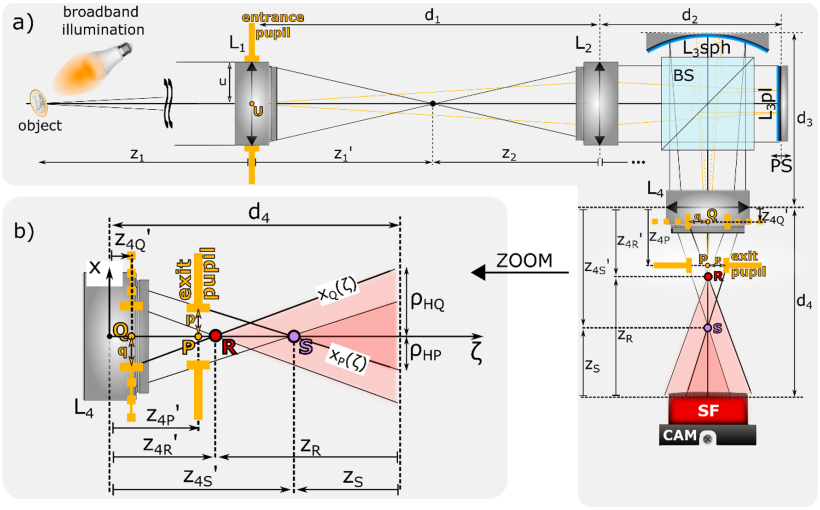

Figure 4.2.10: Experimental configuration and zoom on the camera space [29].

In particular, their focus was on creating a refocusable wavefront using self-interference digital holography (SIDH) with various low-coherence light sources, e.g., sunlight, low-coherence IR laser, etc. The reference and object beam for such a setup emanates from the object. Moreover, due to the broadband illumination, the light source in the visible is inherently low-coherent. With that, the team was able to demonstrate the focusing capabilities in the visible domain, as depicted in Figure 4.2.11. In particular, (a) shows the refocusing capability of a single holographic acquisition where a driller hole is illuminated by an incandescent light bulb with wire filament blocked by the target. The holographic reconstruction of a wooden pinecone and a ceramic statue of a shaman illuminated by white light LEDs, where the image was saturated for better visualization is shown in (b).

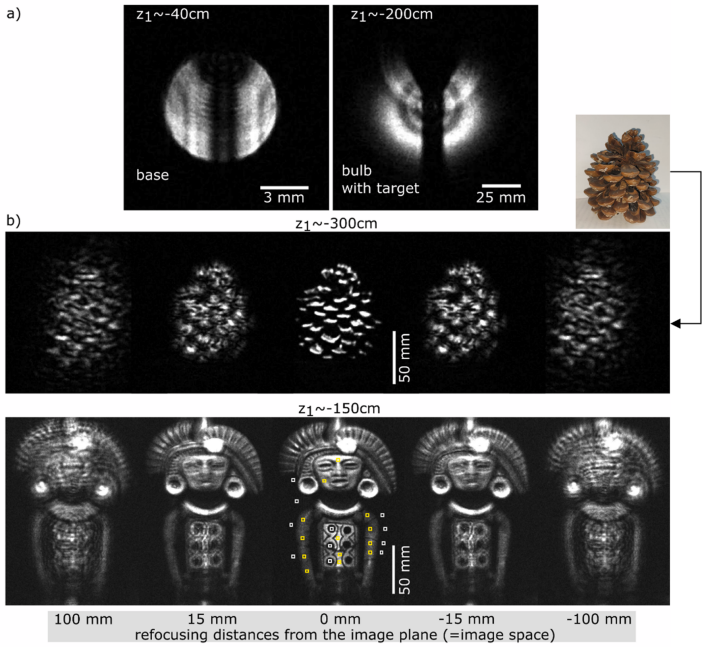

Figure 4.2.11: Refocusing capability [29].

Following this, an infrared SDIH system similar to the one presented in Figure 4.2.10 was implemented. As shown in Figure 4.2.12(a), an expanded infrared laser ($\lambda = 10.6\ \mu$m) was used to illuminate the object. A set of phase-shifted interference recordings with a mutual phase step of $2\pi/2$ (4.2.10(b)) allowed the retrieval of complex amplitudes (4.2.10(c)-(d)). These were then numerically propagated to show the propagated amplitude for which the lateral-axial cross-section is shown in 4.2.10(e). As well, the lateral cross-section in proximity of the focal plane is depicted in 4.2.10(f). It is important to understand that this is the first reported proof of SIDH in the far infrared spectrum, where the capability to obtain and refocus complex wavefronts was demonstrated.

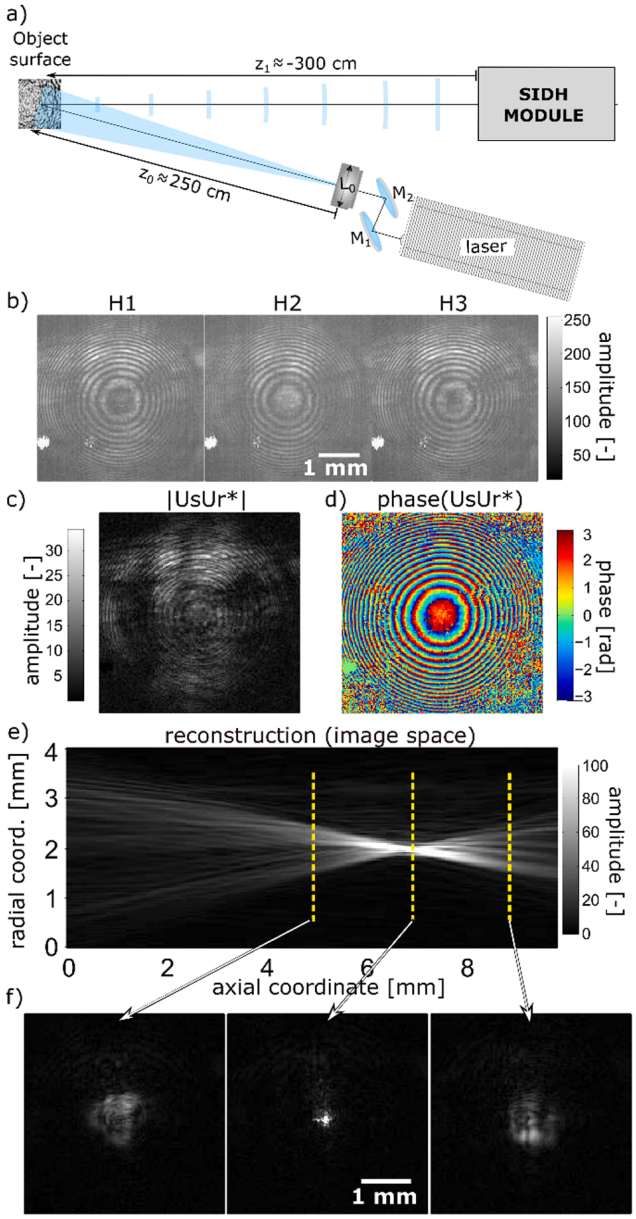

Figure 4.2.12: SIDH in the infrared region [29].

Finally, there remain challenges for imaging larger objects. low-coherence IR lasers require

careful alignment to avoid sensor saturation. Moreover, high-sensitivity IR cameras are necessary but not widely available.

Although of high interest for this work, these experiments have not been applied so far with a self-emitting source. Instead, it still uses a self-reference from an object illuminated by a coherent source.

Based on these, the objective is to perform SIDH in the infrared spectrum, using self-emitting objects. Therefore, instead of lasers illuminating an object, the object will be heated up to a given temperature, thus generating thermal infrared radiations. The goal is then to make that light travel into an interferometric setup and obtain an interference pattern which in turn will enable hologram reconstruction. In particular, the setup will be first aligned using a coherent red laser, and the coherence will then be progressively diminished up until reaching an incoherent source. Once the setup is correctly aligned with the incoherent source, the experiment can shift to the thermal infrared self-emitted radiation from an arbitrary object. This work therefore differs from experiments previously presented as there is no incoherent illumination of an object but the object is indeed self-emitting, thus producing inherently incoherent radiation.

5 | Preliminary study of the experimental setup

Before delving into any practical implementation, a **preliminary study** is conducted to establish the concept and configuration for an infrared SIDH system. This involves a **comparison of** the potential common-path **interferometer configurations**, in particular the Mach-Zehnder and the Michelson setups. Additionally, the main **optical components used for LWIR** interferometry will be determined.

The optical components determined, such as mirrors and beamsplitters are **characterized**, along with their useful **governing equations**. These were evaluated for their behavior, particularly concerning their effect on **polarization**. In addition to that, **ray tracing simulations** were developed in Matlab to demonstrate the **feasibility** of both setups. Based on these, the Mach-Zehnder setup was deemed suitable for the experiment. This preliminary study therefore ensures that the interferometer is correctly chosen, along with its optical components.

5.1 Main optical components

5.1.1 beamsplitters

One of the most commonly used materials for beamsplitters in the infrared is Zinc Selenide (ZnSe). Compared to Germanium, ZnSe is transparent to certain visible wavelengths, i.e., red and higher. This poses a significant advantage for the alignment of any setup intended to work in the infrared spectrum, as it first allows for the alignment in the visible domain.

Within the experimental framework, three beamsplitters made of ZnSe optimized for the infrared (i.e., $\lambda = 10.6\ \mu$m) are available. Despite their design tailored for optical performance in the infrared, the exact properties of the first three optical elements, such as their transmission and reflection percentages, as well as their polarization characteristics were not known prior to the experimentation. Therefore, empirical analysis is necessary to accurately determine the properties of each beamsplitter. Throughout this Master's thesis, the beamsplitters are referred to as BS, the ones with unknown properties are shown in Figure 5.1.1.

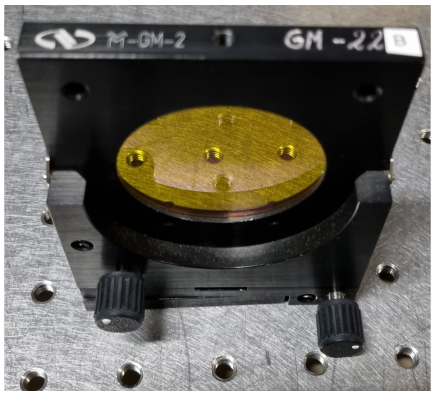

(a) BS1.

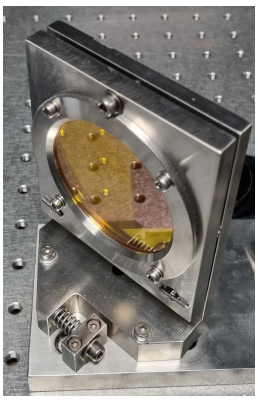

(b) BS2.

(c) BS3.

Figure 5.1.1: Available beamsplitters in the optical laboratory.

The beamsplitters currently optimized for use in the 10.6 μm range may function with a visible laser of 633 nm wavelength, but the performance is not ideal. The specific characteristics of the beamsplitters, such as reflectance, transmittance, and polarization, remain unknown. Consequently, it is crucial to establish these properties. Initially, a power-meter is employed to assess the transmittance and reflectance of each beamsplitter. This involves measuring the irradiance, resulting in the data shown in Table 5.1.

		Irradiance [μW/cm^2]	**Percentage** [%]	$\sum$ [%]
Original beam		535	100	100
BS1	Transmission	263	49.16	72.43
	Reflection	124	23.27	
BS2	Transmission	225	41.78	79.34
	Reflection	201	37.57	
BS3	Transmission	232	43.36	86.35
	Reflection	230	42.99	

Table 5.1: Optical Characteristics of Original Beam and beamsplitters (BS1, BS2, BS3).

The data in Table 5.1 reveals that the cumulative percentages of the beamsplitters do not reach 100% due to the laser wavelength being smaller than the specified optimized value. Consequently, there are some losses, causing a shortfall in the cumulative percentages.
It is however possible to compare the experimental data to values available on Thorlabs' website [30]. Indeed, this company offers beamsplitters made of ZnSe, optimized for specific wavelength ranges and incident angles. The back surface features an anti-reflection coating to enhance transmission and minimize reflection losses, which is typical of ZnSe optics. Hence, the average reflectance is reduced to less than 7% on the back surface. Additionally, these beamsplitters have a 6-10 arcmin wedged back surface that helps mitigate interference effects by preventing parallel propagation of reflected light. In Figure 5.1.2 are provided the transmission and reflection percentages with respect to the wavelength and the polarization state of the light, i.e., unpolarized, s-polarized, and p-polarized. Where s-polarized light is

characterized by an electric field vector, $\vec{E}$, oscillating perpendicular to the plane of incidence. Conversely, p-polarized refers to light where $\vec{E}$ oscillates parallel to the plane of incidence.

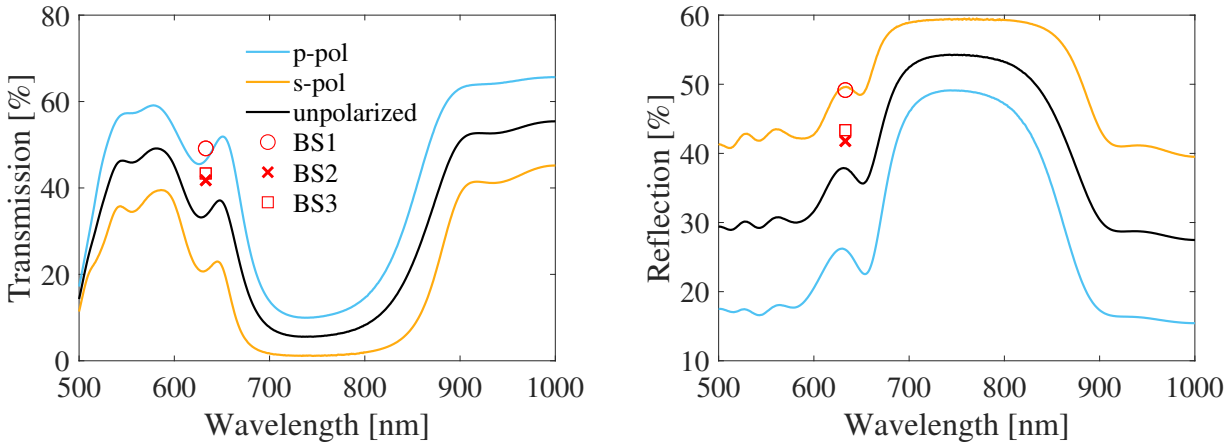

(a) Transmission. (b) Reflection.

Figure 5.1.2: Transmission and reflection of Thorlabs' ZnSe beamsplitters as a function of the wavelength, considering s- and p-polarized, as well as unpolarized light [30].

Examining Figure 5.1.2 reveals that the first beamsplitter was likely manufactured by Thorlabs as it aligns with both the transmission (Figure 5.1.3a) and reflection (Figure 5.1.3b) curves. For the other two beamsplitters, their manufacturer remains uncertain, despite illustrating an approximate 10% difference in both cases. Nevertheless, comparing reflection and transmission, a 90-degree shift in the polarization state is evident. In particular, the p-polarized transmitted light transitions to s-polarized upon reflection, which is consistent with expectations.

Additionally, beamsplitters with given properties were found after a lengthy search in the laboratory. These are depicted in Figure 5.1.3.

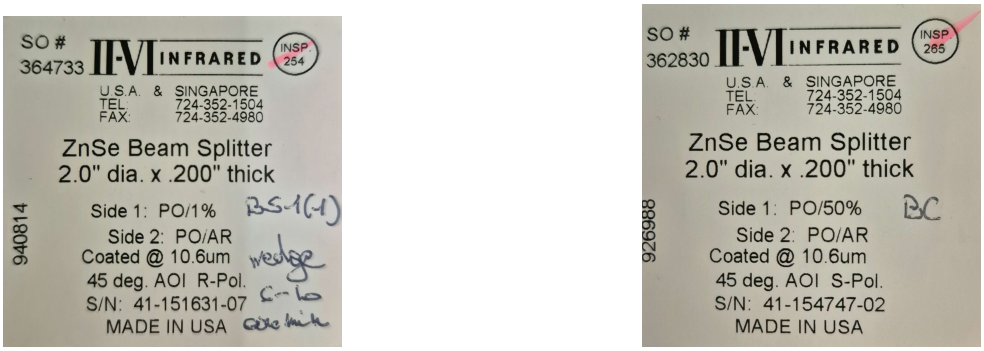

(a) BS4. (b) BS5.

Figure 5.1.3: Additional beamsplitters found in the optical laboratory.

Despite the low reflectivity of BS4, these beamsplitters ensure similar wedges and thicknesses.

Governing equations for wedged beamsplitters

Using Snell's law (see Appendix), it is possible to understand the wedged beamsplitter shown in Figure 5.1.4, which will be used throughout the simulations and experiments.

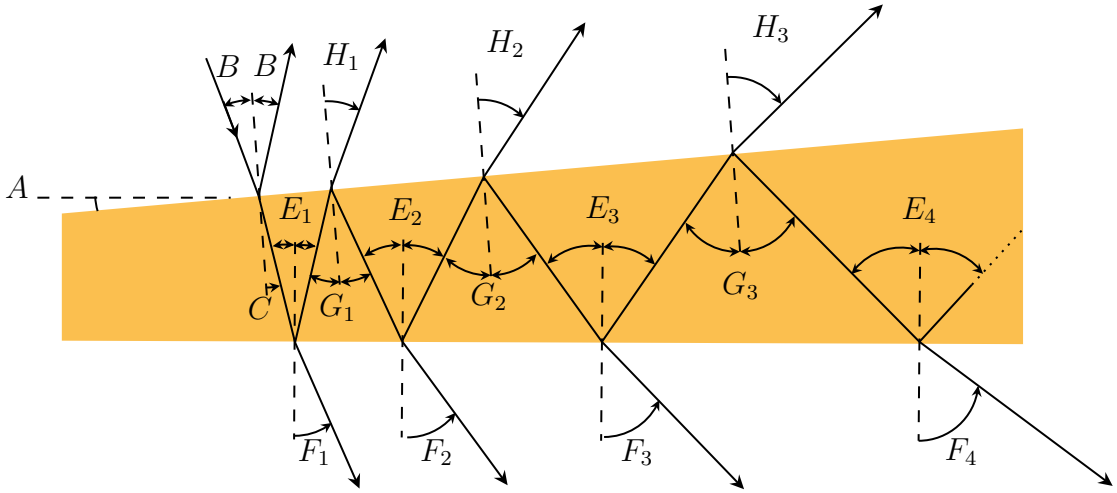

Figure 5.1.4: Ray tracing for the wedged beamsplitter (adapted from [31]).

Using triangle identities, it can be shown that

$$\begin{cases} E_1 = A + C \\ G_1 = 2E_1 - C. \end{cases} \tag{5.1.1}$$

Then using the refraction law and assuming small angles yields

$$F_1 = B_1 + n_{\text{ZnSe}} A, \tag{5.1.2}$$

In this instance, only the first order of transmission and reflection were computed, to avoid unnecessary complexity in the simulations. Where ZnSe's refractive index, n_{ZnSe}, is shown in Figure 5.1.5.

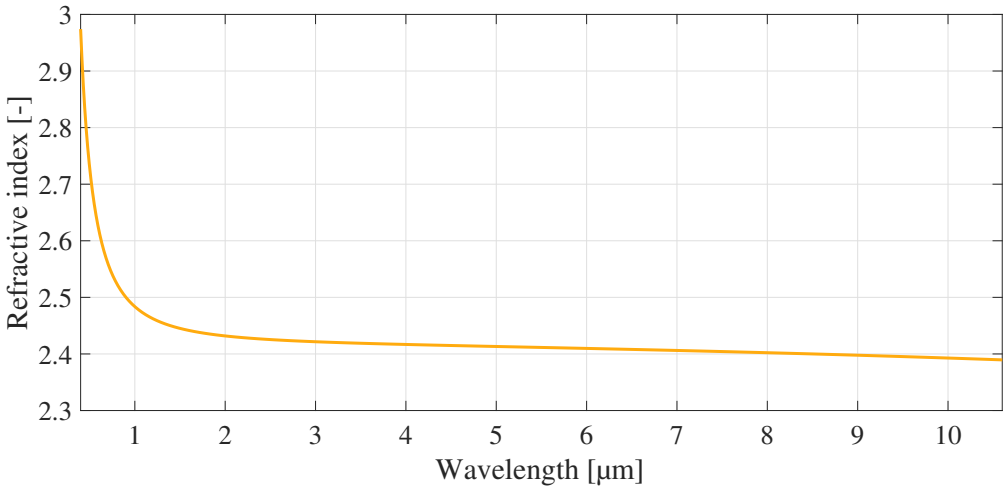

Figure 5.1.5: Refractive index of ZnSe for $\lambda \in [0.4, 10.6]$ μm [32].

5.1.2 Mirrors

Similarly, the mirrors integrated into the experimental setup are coated with gold. While their coating suggests favorable reflective properties within the infrared spectrum, the mirrors' specific properties are unknown. Therefore, further investigation, especially concerning the polarization state shift, are required. The mirrors used in the experiment are denoted as M and shown in Figure 5.1.6.

(a) M1. (b) M2.

Figure 5.1.6: Mirrors used in the experimental setup.

5.1.3 Polarization

For interferometry, polarization is very important. It is indeed required that both beams have the same polarization state to interfere [33]. In order to perform polarization measurements, two polarizers with adjustable angles are used. By manipulating the polarization states of incident light, a systematic characterization of the polarization behavior within the experimental setup is conducted. Both polarizers used have the same characteristics and are shown in Figure 5.1.7.

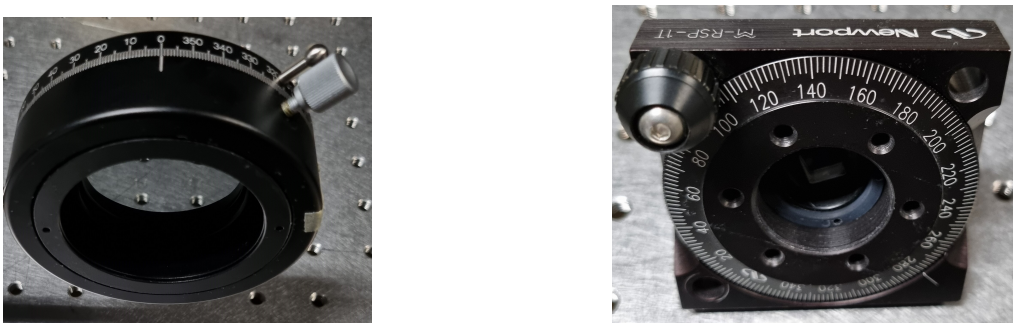

(a) Polarizer 1. (b) Polarizer 2.

Figure 5.1.7: Polarizers used in the experimental setup.

Supplementing the optical components, a red laser emitting at a wavelength of 633 nm is used. This is the primary light source of the experimental setup, providing a consistent and stable beam for the various measurements. Nevertheless, the initial polarization state of the laser is not known, such that additional measurements must be made as well.

The goal of this preliminary study is to determine the optical properties of the components and understand how light interacts within the setup, through systematic measurements and analysis.

The initial step consists in identifying the polarization of the laser employed, which may vary and is not predetermined, encompassing linear, elliptical, circular, or random polarization. For the interferometer, it is crucial to ensure uniform polarization throughout the system. The determination of the polarization follows the flowchart outlined in Figure 5.1.8.

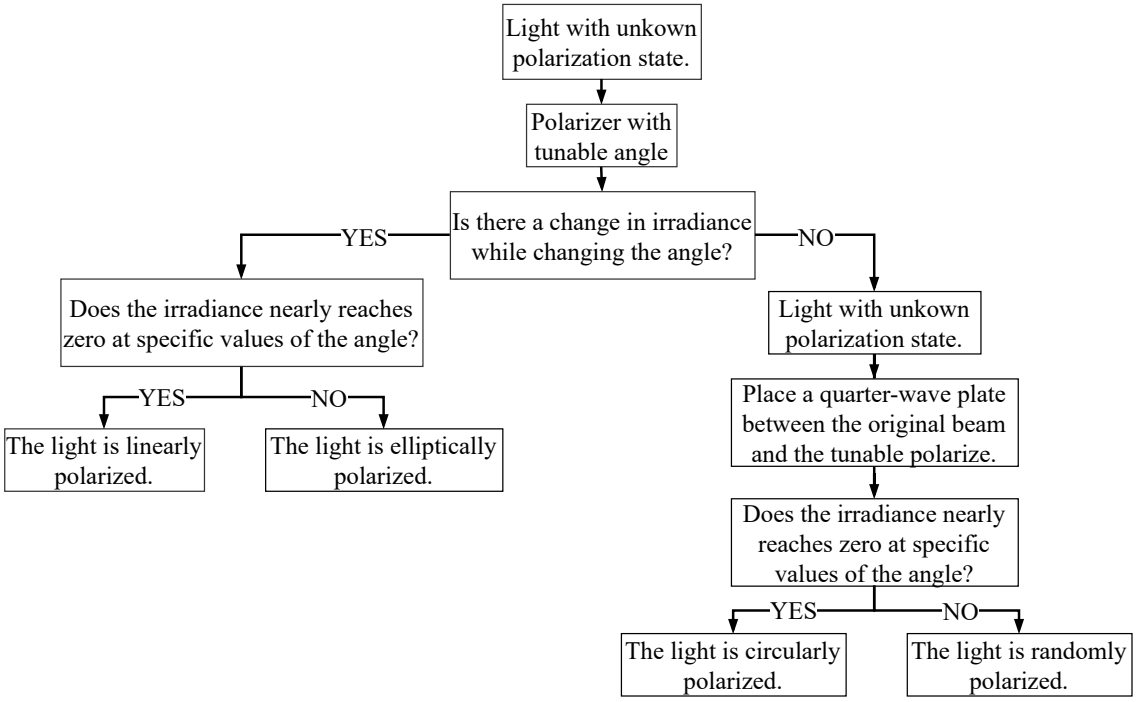

Figure 5.1.8: Flowchart to determine the polarization state of the original laser beam.

In addition to that, it is of interest to compare experimental results with the theoretical Malus law expressing the irradiance for linear polarized light as

$$I(\theta) = I_0 \cos(\theta). \tag{5.1.3}$$

Where $I(\theta)$ is the irradiance of the transmitted light, I_0 is the maximum irradiance of the incident light, i.e., when the analyzer and polarizer are aligned, and θ is the angle between the transmission axis of the analyzer and the polarization direction of the incident light. Finally, the Malus law is shifted by 5 degrees to fit better the experimental data. Consequently, the outcomes are depicted in Figure 5.1.9b, where the setup outlined in Figure 5.1.9a was used to determine the irradiance values of the original beam.

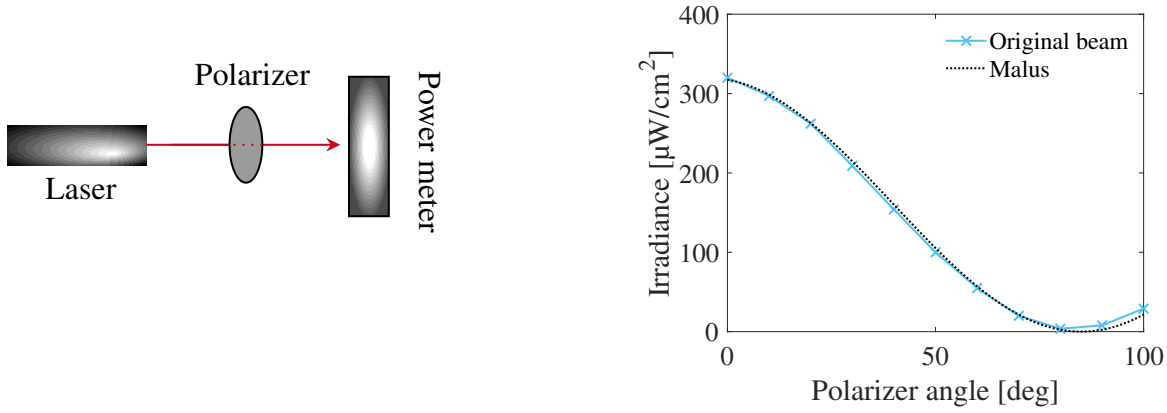

(a) Experimental setup (b) Results

Figure 5.1.9: Setup for determining the polarization state of the original beam and associated results.

It is quite clear that the Malus law shifted by 5 degrees is graphically well correlated with the experimental results. However, it is still of interest to plot the error between the experimental and theoretical results. Nevertheless, since the irradiance reaches zero at some point for the Malus law, the relative error, defined as

$$\delta_{\text{rel}} = 100 \cdot \left| \frac{\text{Experimental} - \text{Theoretical}}{\text{Theoretical}} \right| \ [\%], \tag{5.1.4}$$

cannot be used. Indeed, while the theoretical irradiance tends to zero, the relative error will tend to infinity, which is undesired. Therefore, the root mean square error (RMSE), defined as

$$\text{RMSE} = \sqrt{\frac{1}{n} \sum_{i=1}^{n} (\text{theoretical}_n - \text{experimental}_n)^2} \ , \tag{5.1.5}$$

can be used. Moreover, taking into account the data range involved, it can be expressed as a percentage, i.e.:

$$\delta_{\text{RMSE}} = 100 \cdot \frac{\text{RMSE}}{\max(\text{experimental}) - \min(\text{experimental})} \ [\%]. \tag{5.1.6}$$

The percentages obtained are illustrated in Figure 5.1.10. With a maximum error of approximately 2.5%, it is evident that the experimental data closely aligns with the theoretical values obtained with the Malus law shifted by 5 degrees. Therefore, one could conclude that the initial polarization state of the light is linear.

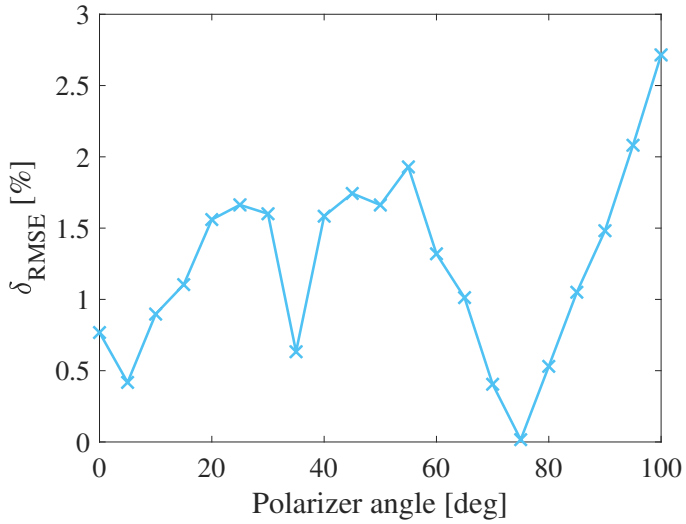

Figure 5.1.10: RMSE between the theoretical Malus law shifted by 5 degrees and the experimental data for the original beam.

However, to confirm the linearity of the polarization state, and thus validate the previous results, the configuration depicted in Figure 5.1.11 can be used. The initial setup involves obtaining irradiance values through the setup shown in Figure 5.1.11a. Then, in the second setup presented in Figure 5.1.11b, the angle of the first polarizer is tuned in to maximize the irradiance at its output, ensuring the beam to be linearly polarized. Hence, the reflection occurs with a purely linear polarized beam. Following this, the angle of the second polarizer is modified to gather irradiance values.

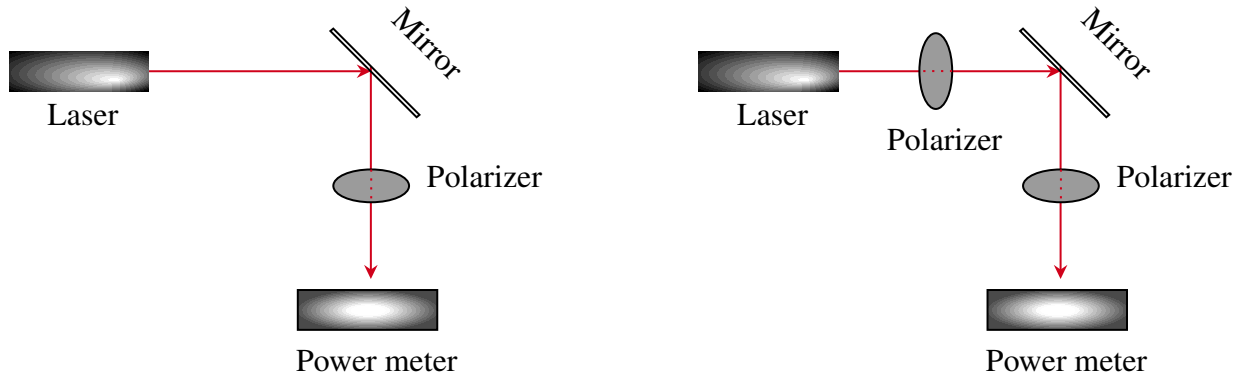

(a) Case 1. **(b)** Case 2.

Figure 5.1.11: Reflection setups for asserting the polarization state of the original beam.

The irradiance values obtained with both setups are then compared in Figure 5.1.12. Evidently, the curves exhibit a strong correlation, allowing to find a mean multiplicative factor, ζ, underlining the correlation between the two sets of data, i.e.:

$$\zeta = \frac{\overline{I_{1,i}}}{I_{2,i}} \approx 0.92. \tag{5.1.7}$$

Where i is the index corresponding to each angle, and the overline indicates that the mean value is taken for each element i.

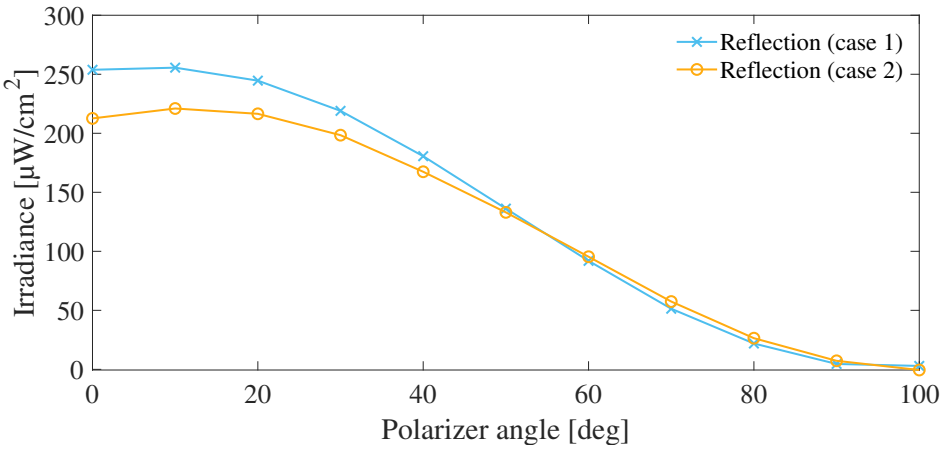

Figure 5.1.12: Comparison of the irradiance values for the setups depicted in Figure 5.1.11.

This ensures that the incoming light is indeed linearly polarized. To further assert this, it is quite clear that the irradiance reaches approximately zero for the same angle. However, it is now important to check that the beamsplitters are non-polarizing. This can easily be done by checking the behavior in reflection and transmission using the setup from Figure 5.1.13.

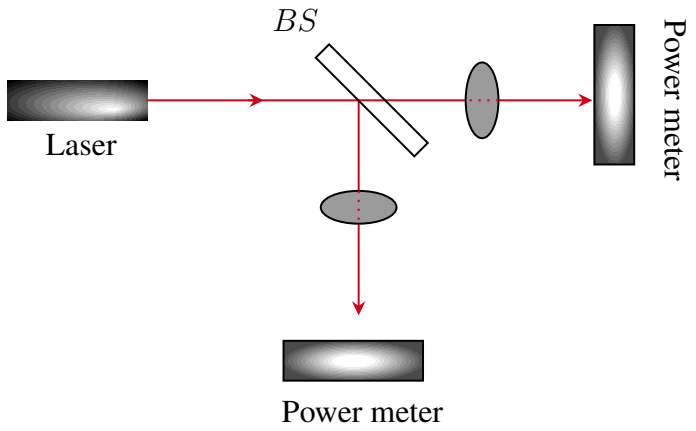

Figure 5.1.13: Setup to verify the polarization behavior of the beamsplitters.

The results obtained for all the available beamsplitters, in transmission and reflection, are then compared to the case without beamsplitter, i.e., Figure 5.1.9a and Figure 5.1.11a. These results are outlined in Figure 5.1.14.

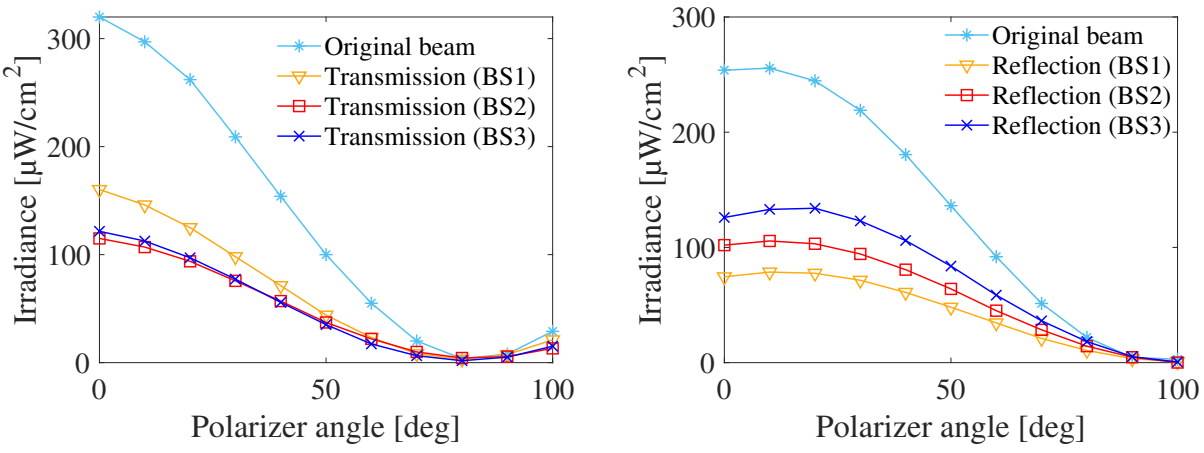

(a) Transmission (b) Reflection

Figure 5.1.14: Reflection setups to very the beamsplitters' behavior regarding polarization in both transmission and reflection.

In Figure 5.1.14a, the trend observed for both the original beam and all beamsplitters in transmission is that the irradiance swiftly diminishes to nearly zero at an angle of 80 degrees. The behavior in reflection is distinct, indeed, it reveals a complete drop in irradiance at an angle of 100 degrees, as illustrated in Figure 5.1.14b. Consequently, a comparative analysis of both reflection and transmission for the original beams is imperative to confirm the observed 20-degree disparity in polarization angles between the two cases. This discrepancy is clearly evident in Figure 5.1.15.

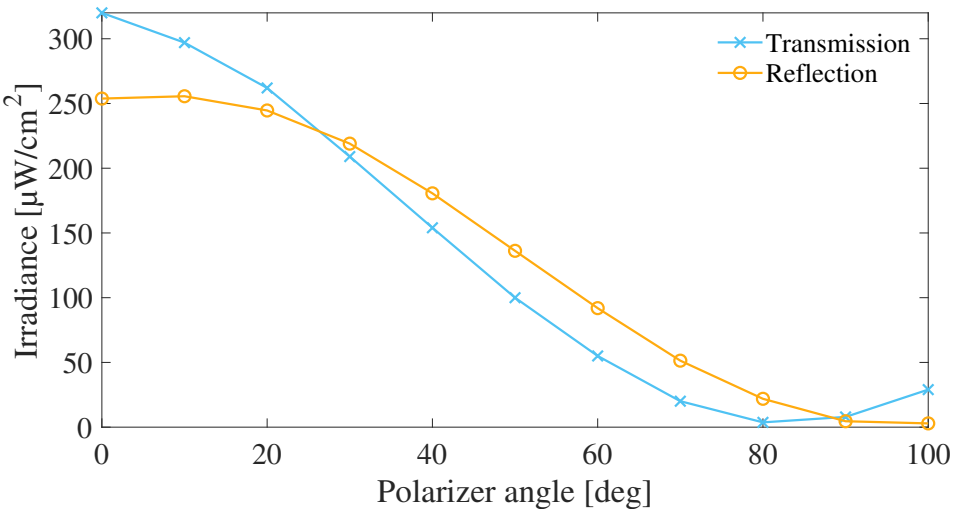

Figure 5.1.15: Comparison of the polarizer's angles leading to a zero irradiance in both transmission and reflection.

With knowledge of the polarization states in transmission and reflection, it is straightforward to predict the polarization state of each beam, anywhere in the interferometric setup. However, to confirm this, the setup depicted in Figure 5.1.16 can be used.

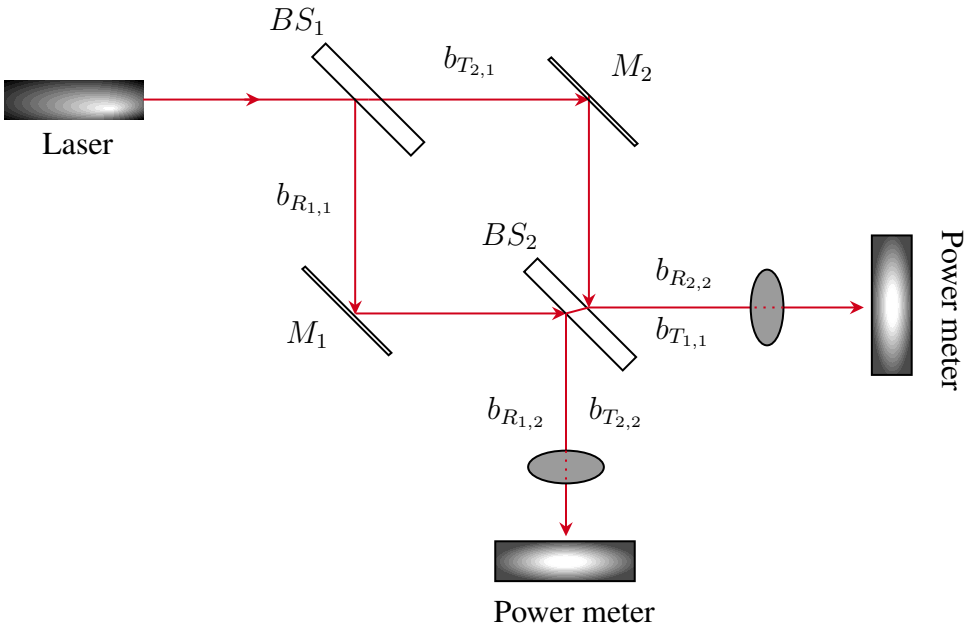

Figure 5.1.16: Complete interferometer setup illustrating the beams, denoted by $b_{T/R_{i,j}}$, either transmitted (T), or reflected (R), with the indices i, j representing the beam path (1 or 2) and the beamsplitter (1 or 2), respectively.

To ensure the same polarization state it is possible to predict that the measurements should be done in the $b_{R_{1,2}}$ and $b_{T_{2,2}}$ paths. Indeed, in this path, the polarization state of both beams should be the same.

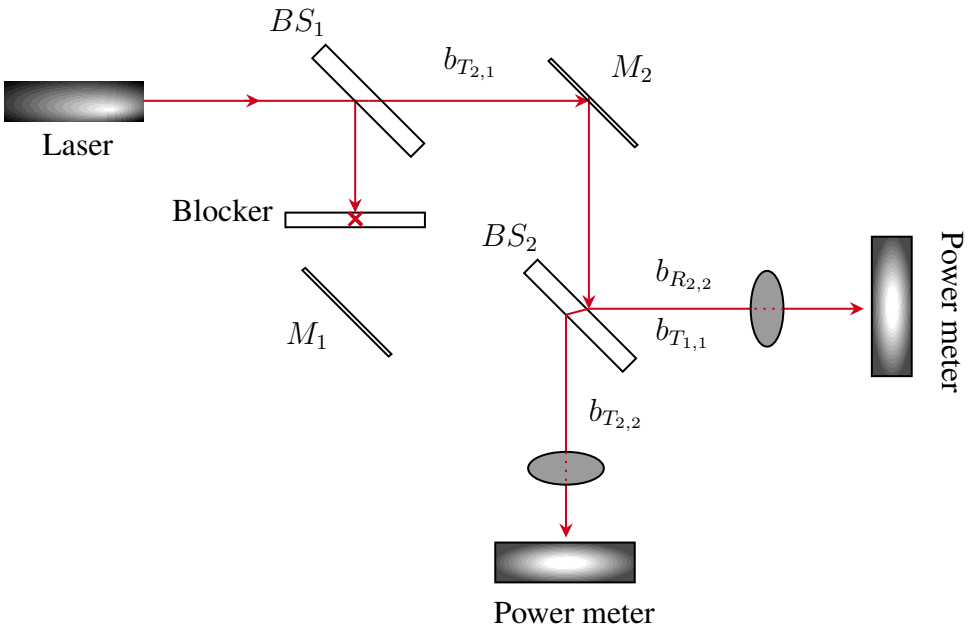

Figure 5.1.17: Example setup for polarization measurements.

Nevertheless, this prediction can be confirmed through measurements conducted by obstructing one ray path, e.g., as depicted in Figure 5.1.17. Subsequently, the irradiance values of each path, with respect to the polarizer angles, for both the transmitted and reflected beams, are measured. These results are shown in Figure 5.1.18, notably, in Figure 5.1.18a a shift of 10 degrees in the polarization can be observed. Whereas no shift is observed in the predicted *correct* path, as demonstrated in Figure 5.1.18b.

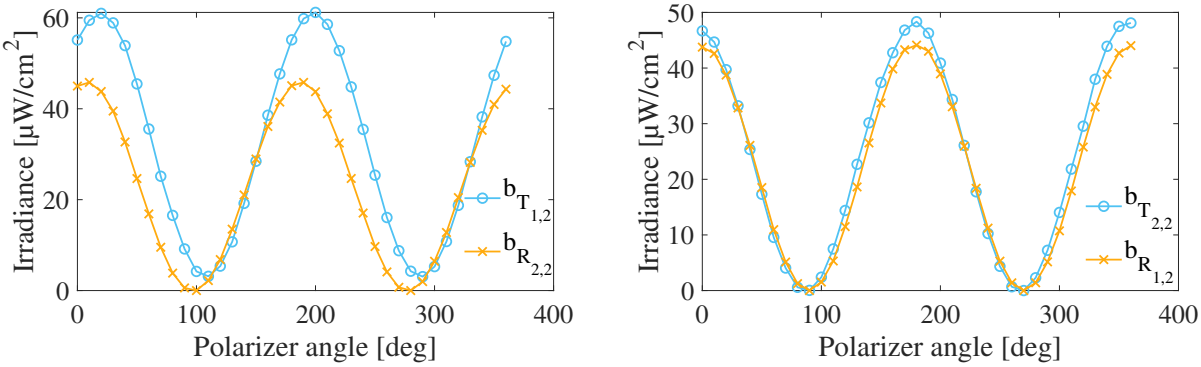

(a) Path of $b_{T_{1,2}}$ and $b_{R_{2,2}}$.

(b) Path of $b_{R_{1,2}}$ and $b_{T_{2,2}}$.

Figure 5.1.18: Irradiance values with respect to the polarizer angle for both ray paths.

5.2 Experimental setup simulations

Now that the beamsplitters' properties and the arms where measurements are performed are known, it is essential to perform simulations and sensitivity analysis of the different interferometers.

5.2.1 Ray-tracing

To verify the practicality of the experiments, conducting simulations is essential. Simulations will focus on optimizing the positions and angles of each optical component to ensure equal paths in the arms of interest. This step will determine the feasibility of the experiment. Following that, a sensitivity analysis of various parameters will be carried out.

Mach-Zehnder interferometer

Now that everything can be computed, it is possible to perform simulations and fine-tune the positions and angles of the components. The goal is to ensure that the optical paths are balanced within the coherence length. To achieve this, the MATLAB function *fmincon()* is used as an optimization tool, aiming to meet the zero-Optcial Path Difference (OPD) constraints by automatically adjusting the input parameters iteratively.

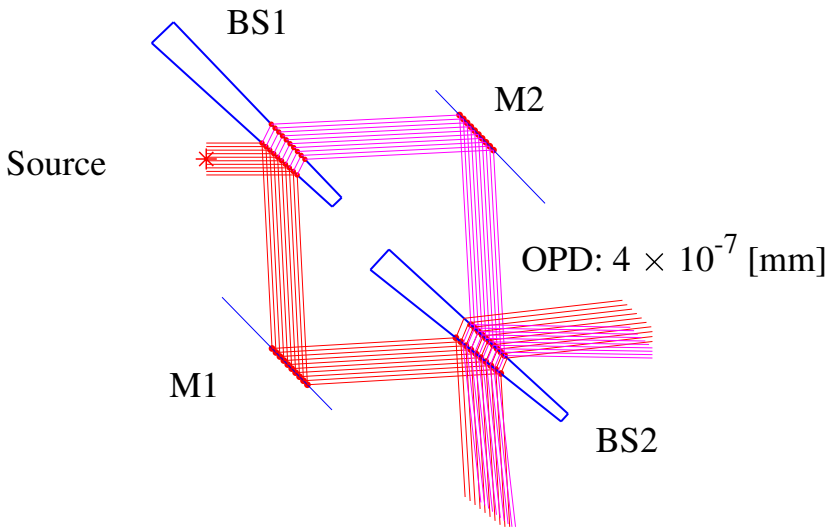

Figure 5.2.1: Ray-tracing for the Mach-Zehnder interferometer.

From Figure 5.2.1, one can observe that, in the arms of interest, nearly zero-OPD is reached, therefore rendering the experiment feasible. Nevertheless, it is still important to note that this simulation was performed in two dimensions. Hence, three-dimensional effects are not taken into account. Even though this represents a limitation, the simulations provide a good approximation of the positions and angles required to satisfy the constraints. Additionally, it is important to note that optical path difference was computed by subtracting one path from the other, i.e.:

$$\text{OPD} = |\text{Magenta path} - \text{red path}| \tag{5.2.1}$$

Obviously, concerning the beamsplitters, the governing equations presented in Governing equations for wedged beamsplitters were used to compute the ray path through and after the beamsplitters. One can easily observe that in any path, the beams superimpose, which renders the interference possible. Nevertheless, it must be considered that variations in height, such as pitch were not taken into account. Intuitively, such variations of the beamsplitters' angles could help co-align the beams.

Michelson interferometer

Concerning the Michelson interferometer, the same equations as for the Mach-Zehnder one are used. Even though the optical paths are very similar, it is quite clear the light rays are not superimposed, as can be observed in Figure 5.2.2. Therefore, no interference can be reached since the waves are not interacting with one another. More precisely, the waves do not interact at a reasonable distance, it was shown that it would be the case several meters away from the beamsplitter. Therefore, this renders this setup impractical. Moreover, even though compensating plates could be used, none are available at the laboratory such that this potential setup is discarded from the practical implementation.

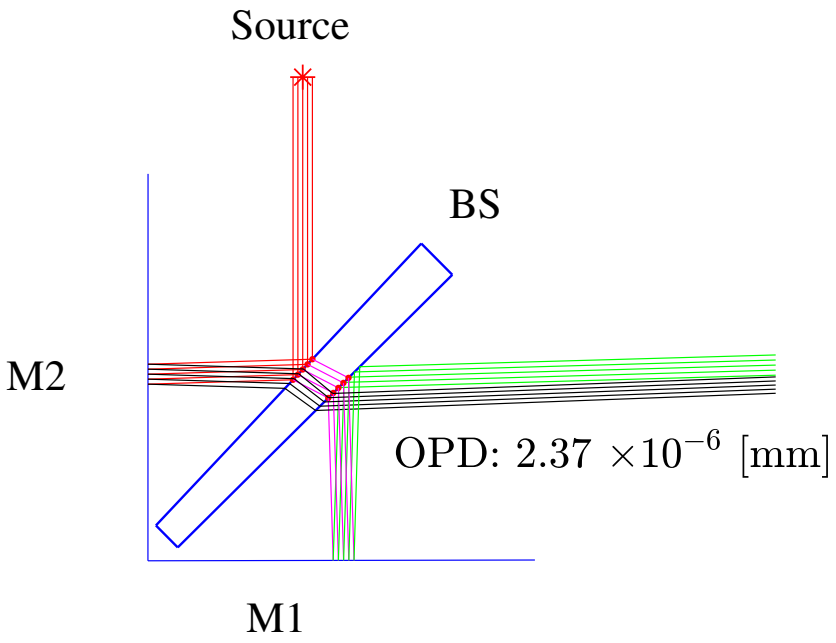

Figure 5.2.2: Ray-tracing for the Michelson interferometer.

5.2.2 Conclusion on the first simulations

Even though the Mach-Zehnder setup is theoretically feasible, it is important to understand that in practice, the correct alignment will be much harder. Indeed, the degree of precision required to achieve zero-OPD is impossible to reach by simply placing the optical components on the optical bench, but by pure luck. Therefore, the positions of the various components merely give an approximate of their position for the practical implementation.

5.3 Sensitivity analysis for the Mach-Zehnder interferometer

Considering that the beamsplitters' angles are fixed, only the mirrors can be tuned. Figure 5.3.1 shows the influence on the OPD with varying mirror angles.

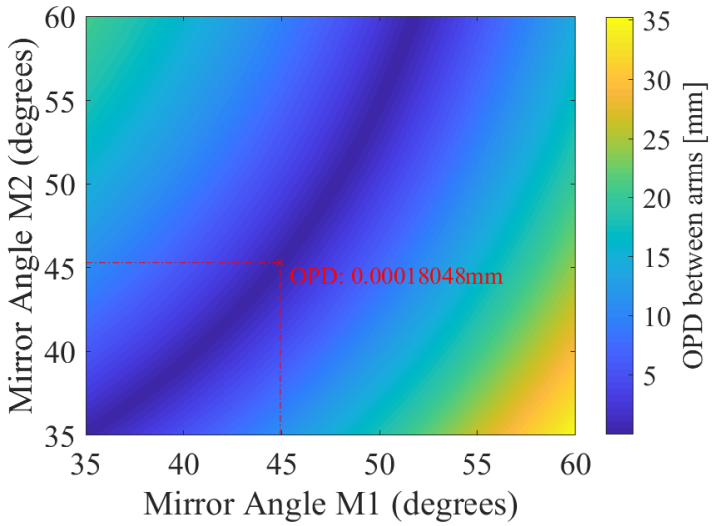

Figure 5.3.1: Influence of the mirrors' angles on the optical path difference.

It is quite clear that only a certain range of angles is admissible to ensure an OPD near zero, denoted by the dark blue area. In addition to that, it is important to mention that even if the OPD is near zero everywhere in that area, not every angle combination yields sufficient low-OPD while working with white incoherent light. Therefore, the minimum that satisfies the coherence length requirement was identified with a red cross, as well as the corresponding OPD. Indeed, 10^{-4} mm is sufficient and satisfies the constraints on the OPD. However, reaching such a degree of accuracy without directly measuring the resulting interference pattern on a camera is impossible by hand. Nevertheless, it is theoretically possible and thus gives a good approximation of the angles required to ensure minimum OPD.

In addition to that, fringe patterns were simulated with respect to the angle between the rays. The rays were considered to be collimated with an arbitrary diameter. The angles were first equalized to produce a constant intensity pattern over the simulated detector. Small increments from this position were then performed such that the angle difference between the rays is $\Delta\alpha \neq 0$, as depicted in Figure 5.3.2.

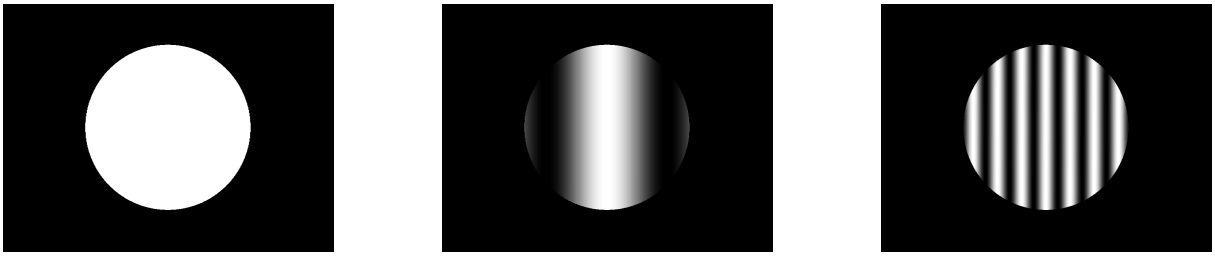

(a) $\Delta\alpha = 0°$. (b) $\Delta\alpha = 0.02°$. (c) $\Delta\alpha = 0.1°$.

Figure 5.3.2: Simulated fringe patterns for various angle differences between the waves, $\Delta\alpha$.

It is quite obvious that the phase shift induced by the varying angle influences the number of fringes. In this case, the sensor was simulated to show that the number of fringes increases significantly when the phase shift is not close to zero. This occurs because the varying angles introduce different optical path lengths for the beams. Therefore, this leads to phase differences across the interference pattern.

In practice, when the two beams are perfectly co-aligned, only the white fringe should be visible (Figure 5.3.2a). That is because, supposing that the optical paths are equal, the beams are perfectly superimposed on one another. Therefore, there is no phase difference between the beams, which leads to a single white fringe. This will be explored in depth in the practical implementation.

6 | Practical implementation

Now that simulations have proven the theoretical possibilities, it is possible to start mounting the optical elements onto the optical bench. The goal of this section is to explain how to **pre-place the elements** on the bench, and how to **fine-tune** them in order to fulfill OPD requirements.

First, a setup with beamsplitters $BS2$ and $BS3$ was tested but yielded inconclusive results. This inconclusive experiment will then be explained later on. Secondly, a setup with beamsplitters with identical wedges and thicknesses was opted for. Even though several key parameters need to be taken into account, this new configuration worked flawlessly. Therefore, to explain how a setup can be deemed conclusive or not, it is important to understand how to calibrate and align the setup for incoherent white light interferometry. This section will explain the alignment of the successful setup, which will provide insight into why the first setup was bound to fail.

6.1 Definition of an optical axis

After choosing the correct optical components, it is first essential to ensure that the source will follow a straight line. This can be done by defining an optical axis. To do so, it is required to have a mount for the source that will allow for the fine-tuning of its orientation. In this case, the support shown in Figure 6.1.1 was used.

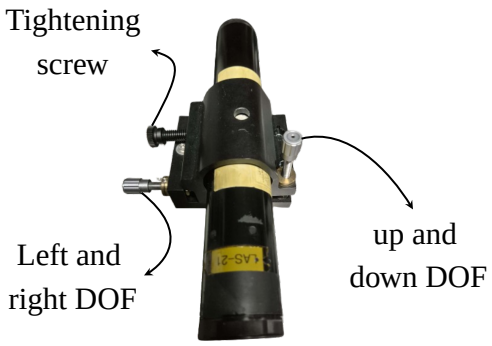

Figure 6.1.1: Laser mount with the corresponding degrees of freedom (DOFs).

To define the optical axis that will be used throughout this experiment, diaphragms must also be used. Indeed, these will allow to verify if the laser is indeed following the path of interest. Figure 6.1.2 shows the importance of using more than a single diaphragm.

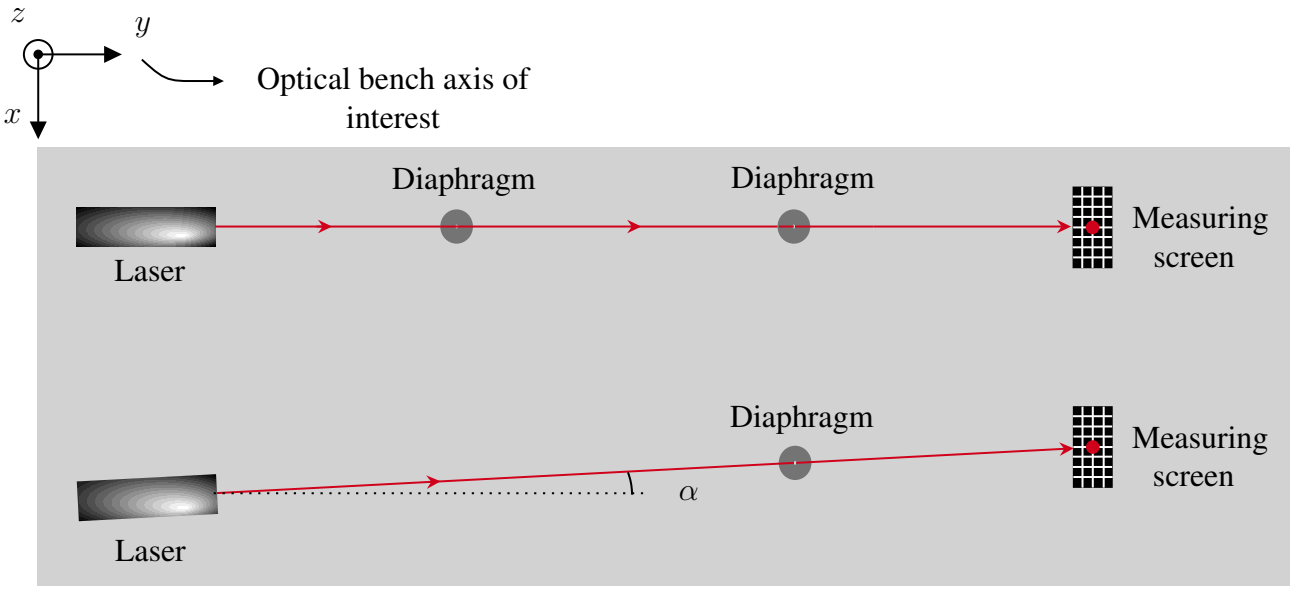

Figure 6.1.2: Illustration of the importance of using two diaphragms.

It is quite clear that the impact point on the measuring screen is the same in both cases. However, when using a single diaphragm, the optical axis is not well defined. Indeed, it follows a line with an angle $\alpha \neq 0$, with respect to the optical bench. This can easily be avoided by using a pair of diaphragms placed at a long distance from one another. Indeed, this will ensure that the optical axis is perfectly aligned with the optical bench, ensuring a 0-degree ray with respect to it.

In addition to that, the source is placed on an elevation platform to grant a degree of freedom perpendicular to the optical bench (z-direction). This addition enables the choice of a height. In this case, a height of $h = 10$ cm was chosen to match the height of the other optical elements mounted on the various platforms, as shown in Figure 6.1.3.

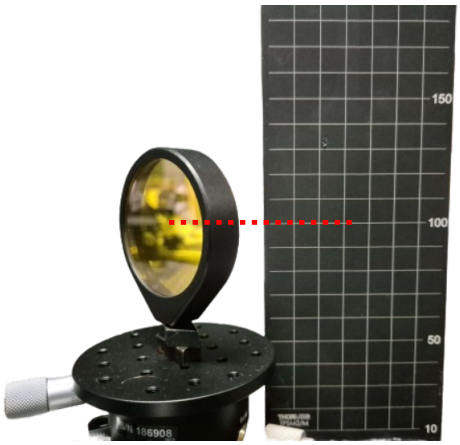

Figure 6.1.3: Height of the first beamsplitter. The other components sit at the same height. The height $h = 100$ mm is indicated by a red dahsed line.

6.2 Preliminary steps

6.2.1 Translation, rotation, tip, and tilt platforms

After simulating using various optical elements, it is possible to obtain a rough estimate of where the components should be placed. Therefore, the first step is to allow some freedom on the position and orientation of the optical components after fixing them to the table. To do so, translation and tip/tilt/rotation platforms must be used. As well, the mounts for the mirrors were selected to allow for a change of angle at any time. This step is very important since it gives more degrees of freedom for each component used in the setup. Nevertheless, in close alignment with the coherence length, and therefore the OPD requirements, it is important to choose platforms that will give sufficient precision. Since these platforms work with a knob, it is important to ensure that the rotation of the knob is precise enough. Finally, to enable the translation in the $x-y$ directions shown in Figure 6.1.2, it is essential to assemble two translation platforms together, with their moving axis perpendicular to one another.

In the case of the translation platforms used, a full rotation yields a 0.5 mm difference with respect to the initial position. Therefore, with the help of the graduation present on the knobs, it is possible to determine that each tick will change the component's position by 10 µm. This precision is thus lower than the coherence length, such that the translation platforms are suitable for this experiment, allowing fine-tuning of the components.

Concerning the tip, tilt, and rotation platforms made by Thorlabs, the resolution provided by each graduation is 0.036° and 0.03° for tip/tilt, and yaw, respectively. Therefore, these also allow for fine-tuning of the optical setup.

To facilitate the alignment and calibration of the setup, the translation platforms are used in combination with the mirrors. This choice was of course not made randomly since a fixed beamsplitter and two mirrors define the length of an arm of the interferometer. Therefore, fixing the beamsplitter, only allowing for tip/tilt/rotation, and ensuring xy freedom for the mirrors allows for fine-tuning the length of each arm.

6.2.2 Placement of the optical components onto the optical bench

The first placement of the optical components onto the optical bench must be precise. First, all the platforms must set to an initial position, that is to give the maximum freedom in all directions. This means that if the translation platforms can travel 10 cm, the initial position will be considered to be where it can travel 5 cm in each direction. The same freedom is thus granted to the tip/tilt/rotation platforms.

6.2.3 Tuning of the first beamsplitter

First, one must ensure that the incoming beam strikes the first beamsplitter exactly in the center. Moreover, it is also of paramount importance to ensure that the incident angle is

indeed of 45 degrees. This can easily be done by placing the beamsplitter at a given position, and checking if the reflected ray is perfectly perpendicular to the incoming ray. This is of course performed by using two diaphgrams, i.e., the optical axis defined previously is simply shifted by 90 degrees, as seen in Figure 6.2.1.

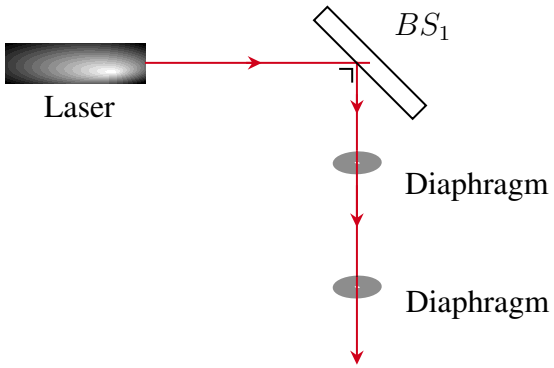

Figure 6.2.1: Simplified schematic of the optical axis defined in the reflection of BS1.

However, as shown in Figure 5.1.4, the wedged beamsplitter produces some unwanted reflections and transmissions as well. Therefore, the orientation of the wedge is crucial to ensure correct alignment and calibration. Moreover, the orientation chosen for the first beamsplitter must be exactly the same for the second beamsplitter. There are two possibilities to efficiently orient the wedge, i.e.:

1. Option 1: The wedge is placed so that the parasitic reflections and transmissions lay in a plane parallel to the optical bench, as presented in Figure 6.2.2.

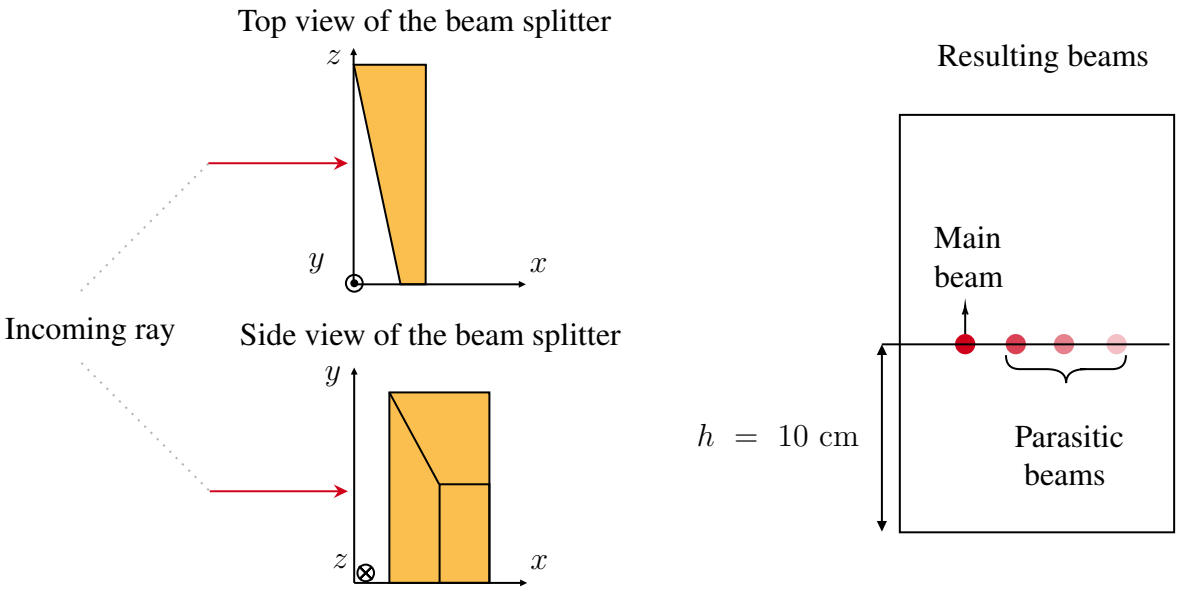

Figure 6.2.2: Illustration of the wedge orientation and the resulting beams for option 1.

With this orientation, only the z and y-positions of the impacting beam must be carefully tuned to ensure that the incoming beam strikes the beamsplitter exactly at its

center. Nevertheless, for an incoming beam striking at a given z position, the y-position is less important since the same thickness is guaranteed for any y and given z-positions. Moreover, this orientation ensures that the parasitic beams indeed lay in a horizontal plane with respect to the optical bench.

2. Option 2: The wedge is placed so that the parasitic reflections and transmission lay in a plane perpendicular to the optical bench, as shown in Figure 6.2.3.

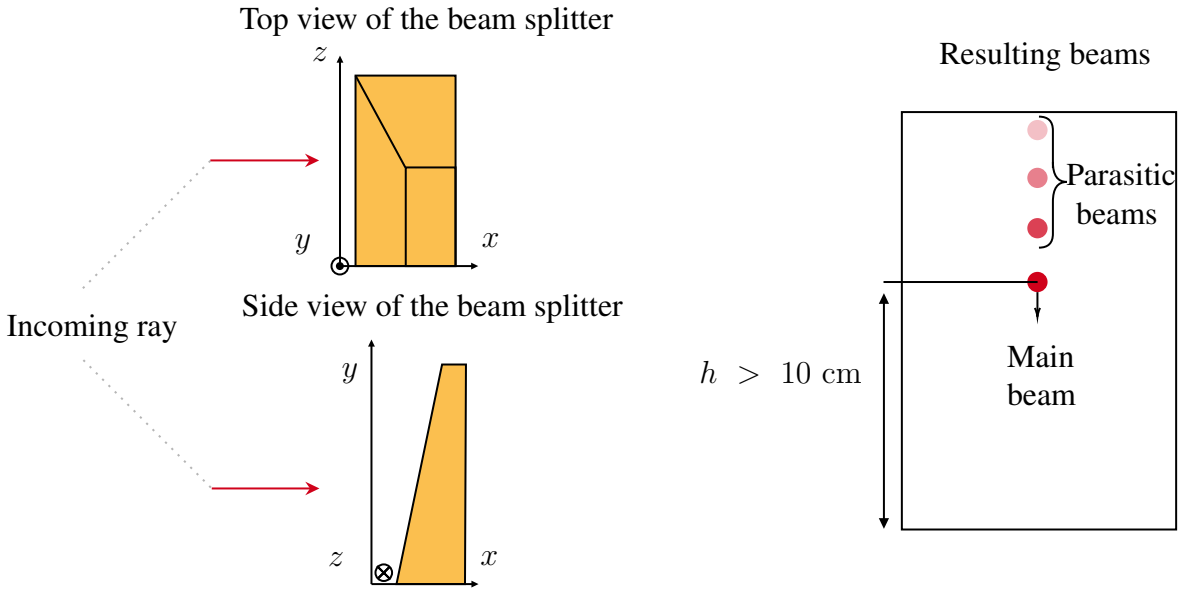

Figure 6.2.3: Illustration of the wedge orientation and the resulting beams for option 2.

Opposite to the first orientation, here, the z-position is less important since the same thickness is guaranteed for any z and given y. Nevertheless, with this option, the parasitic beams are in a plane perpendicular to the optical bench.

Both options yield the same result in terms of optical path length. However, to simplify the setup, option 1 is the most suitable. That is because the optical axis' height remains at $h = 10$ cm. Indeed, during the experiment, it was deemed impossible to use option 2 and get the main beam impact at a height of 10 cm. Therefore, to keep everything leveled at h, option 1 is chosen for the orientation of the beamsplitters' wedges.

Finally, since the orientation of the beamsplitter is governed by the reflection to ensure a perfect 45 degrees incidence, the transmission path of this first beamsplitter remains untouched. Therefore, it is important to note the deflection angle, α, with respect to the original optical axis. There are two methods to do so, either analytically, or experimentally. The easiest one is to place a screen at a distance sufficient enough to ensure that the parasitic beams and the main beam do not overlap. Then, one must note the deflection with respect to the original optical axis and keep this data for the next steps. The resulting beams are shown in Figure 6.2.4.

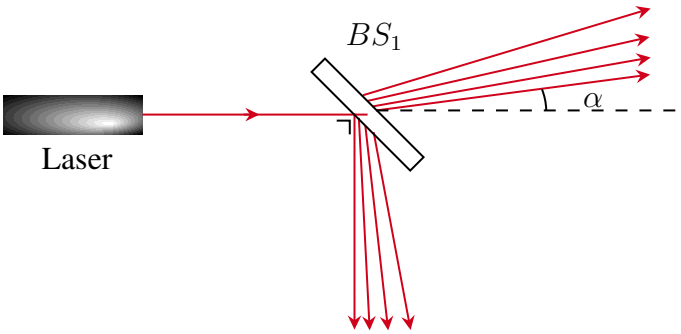

Figure 6.2.4: Resulting beams' paths in reflection and transmission of the first beamsplitter.

In practice, the beams obtained are stopped by a screen shown in Figure 6.2.5.

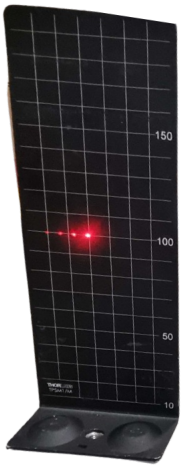

Figure 6.2.5: Beams obtained after transmission by BS_1.

The deflection can easily be computed by considering the scheme depicted in Figure 6.2.6.

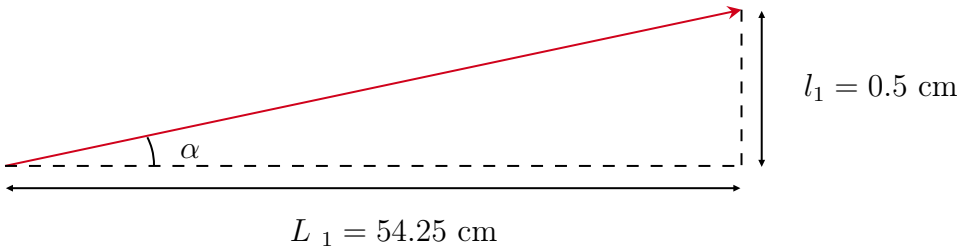

Figure 6.2.6: Schematic for the computation of the deflection angle α.

Indeed,

$$\alpha = \arctan\left(\frac{l_1}{L_1}\right) \approx 0.53 \text{ [deg]}\,. \tag{6.2.1}$$

Preliminary tuning of the second beamsplitter

For the second beamsplitter, it is imperative to exactly ensure the same orientation of the wedge. This is of paramount importance, otherwise, the optical paths could be slightly different, leading to no visible interference pattern. Therefore, the same steps and same results as for the first beamsplitter must be performed.

6.2.4 Tuning of the first mirror

The first mirror, M_1, must be tuned in order to reproduce exactly the same behavior than the beamsplitter in transmission. Therefore, the deflection angle α must be reproduced in that part of the arm as well. This is easily done by placing a screen at a distance L_1, and computing the deflection along that length, at two points, where diaphgrams will be placed. Nevertheless, it is important to consider that the beam travels first in the reflection, covering a given distance L_2. This allows to follow the exact deflection from the original optical axis, as shown in Figure 6.2.7.

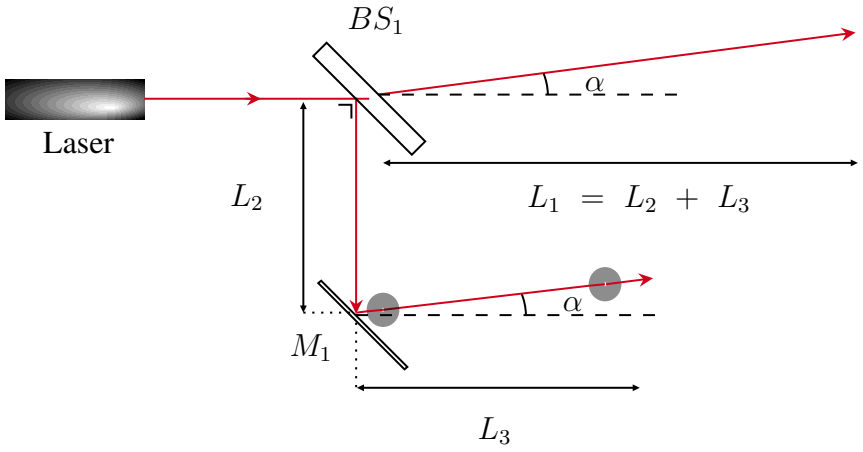

Figure 6.2.7: Alignement of the first mirror, M_1, to ensure the same path as the ray transmitted by BS_1.

The pattern obtained at a distance $L_2 + L_3$ is therefore the same as the one shown in Figure 6.2.5, which ensures that the rays of interest are parallel. It is however important to note that the distance L_1 is longer than the arms themselves. That is to ensure that the parasitic reflections are well separated and all visible.

6.2.4.1 Tuning of the second mirror

The second mirror, M_2, is placed in the transmission path of the first beamsplitter. A good starting point is to place it exactly at a distance L_2 from BS_1 along the optical axis, which ensures a good starting point for further alignment. When the mirror is placed on the optical bench, it is necessary to tune its angle so that it will provide a reflection exactly similar to the one emanating from BS_1. Hence, the ray emanating from the reflection of M_2 must be perpendicular to the original optical axis defined in the beginning. Once again, this is done by using two diaphragms, as shown in Figure 6.2.8.

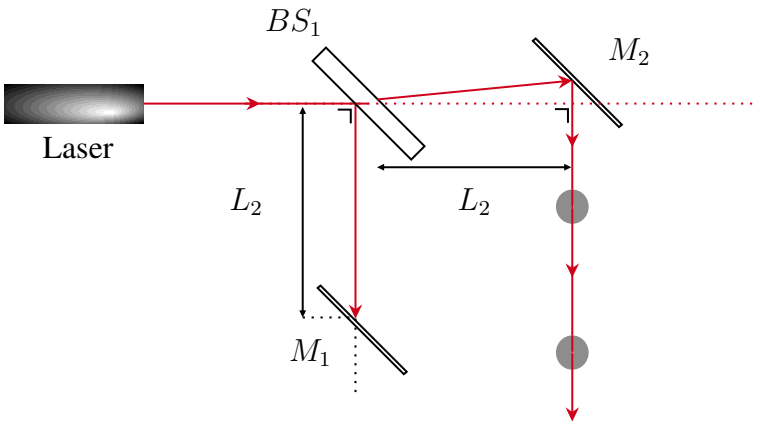

Figure 6.2.8: Alignment of the second mirror to ensure a ray perpendicular to the original optical axis.

This will ensure that only the rays emanating from the transmission of BS_1 and M_1 have a deflection with respect to the original optical axis.

6.2.5 Refinement of the tuning of the second beamsplitter

The second beamsplitter exactly provides the same behavior as the first one. Therefore, a good guess for the placement is at a distance L_2 from both mirrors. This will guarantee that the optical paths are already roughly the same. Nevertheless, the alignment of this beamsplitter is not finished yet. Indeed, a deflection angle α will appear in the transmission path of BS_2. While in reflection, this angle depends on the angle of incidence of the incoming rays. Therefore, it is of capital importance to tune the angle of BS_2 so that the rays in transmission and reflection are co-linear, i.e., they are superimposed on one another. Hence, the angle of this second beamsplitter must yield a deflection α as well.

In addition to that, it is also important to ensure that the beams coming from M_1 and M_2 impact the beamsplitter exactly in the middle, i.e., at the impact point of BS_1. This will ensure that the optical paths through the beamsplitters are the same. However, there is no pre-determined technique to do so, it must be placed on the table to ensure both conditions, i.e., distant of L_2 from both mirrors and impact exactly in the middle. Therefore, the best way that was found to do so was to place it on the table and move it, by hand, until reaching both conditions.

Finally, to ensure that the deflection angle will indeed be of α, one must tune the pitch/roll/yaw knobs until reaching the perfect co-linearity of the beams. This is verified by first hiding one path, i.e., the path of BS_1 in reflection, and placing diaphragms as far as possible. The blocked path is switched to the one of BS_1 in transmission and the angles of BS_2 are tuned to ensure that the emanating ray indeed goes correctly through all the diaphragms. The final schematic is displayed in Figure 6.2.9, only the path of interest, i.e., where the polarization angles are the same, is taken into account. It is nevertheless important to understand that the beams are perfectly co-aligned with the level of precision used during these steps, i.e., it

is a rough co-alignment. Further co-alignement will be reached by analyzing fringe patterns later on.

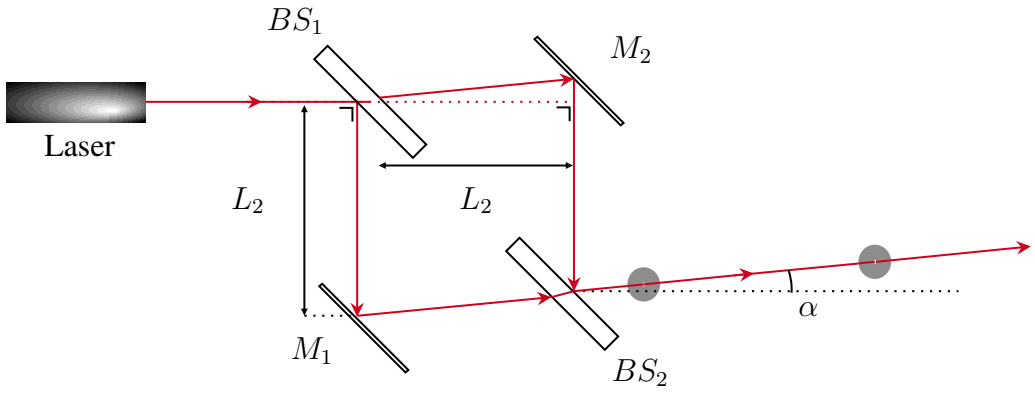

Figure 6.2.9: Final setup with the rough placement ensuring approximate equal length.

6.2.6 Supplementary considerations

Now that the setup is roughly aligned, it is of interest to eliminate the parasitic reflections from the beamsplitters. Indeed, since BS_1 yields four parasitic reflections, in turn, BS_2 will yield sixteen, hence in the end, 32 beams would be visible in the final path of interest. Therefore, eliminating them nearly becomes necessary. Fortunately, suppressing these can be done relatively easily by using diaphragms once again. These must be placed as shown in Figure 6.2.10.

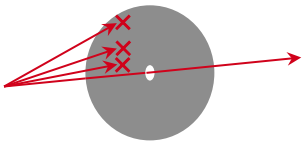

(a) Schematic of the straylight elimination.

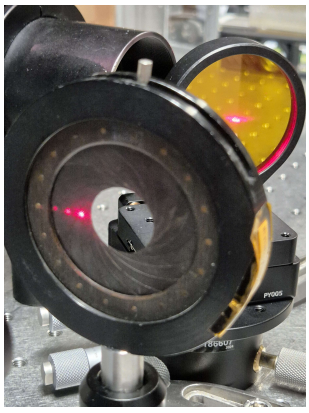

(b) Practical implementation of the diaphragm to efficiently suppress any unwanted light.

Figure 6.2.10: Schematic and practical implementation of effective straylight suppression for visible wavelengths.

The same process is used in both the reflection and transmission of the first beamsplitter, enabling to only get eight beams in the final ray path. Since the beams in reflection and

transmission of BS_2 are co-linear, only four rays are visible to the naked eye. The final setup with the diaphragms is depicted in Figure 6.2.11.

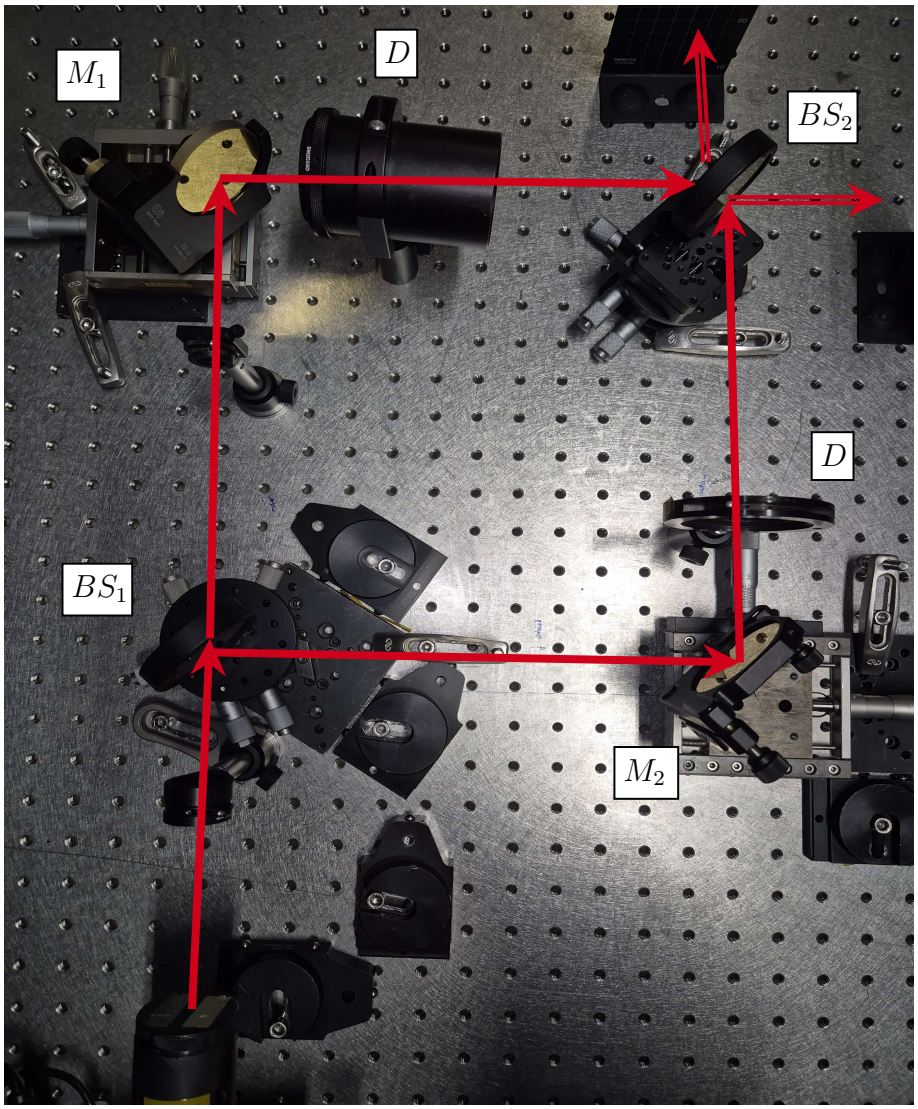

Figure 6.2.11: Final setup with effective straylight reduction. The diaphragms are denoted as D.

6.3 Theoretical visibility of the fringes with a Helium-Neon laser

Following this, a power meter is used to measure the intensity in each arm. In particular, the power meter is placed in the path of interest, and one arm is hidden after the other, as depicted in Figure 6.3.1.

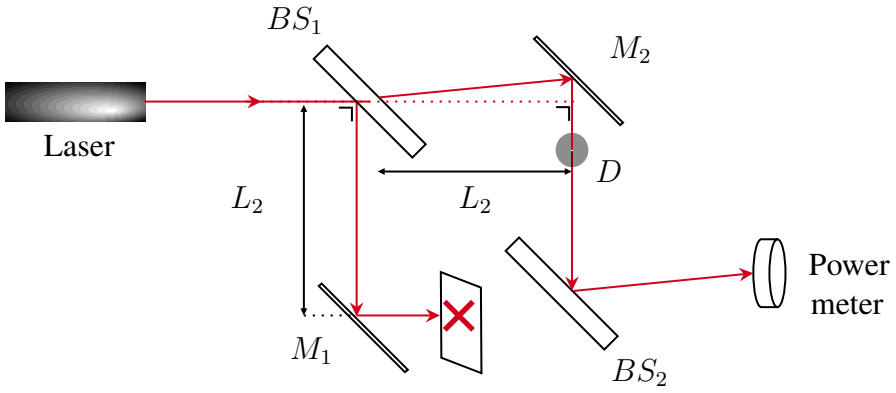

Figure 6.3.1: Position of the power meter and example of one ray path blocked.

The other path is then blocked and each of the intensities is measured. In the case of unequal intensities, one should use a neutral density filter, NDF. This will allow to have the same intensity for each beam, and thus, one path is not *blinding* the other. This of course is necessary, otherwise, there will be no contrast in the fringe pattern. Indeed, considering the visibility equation, it is possible to prove it graphically, as shown in Figure 6.3.2.

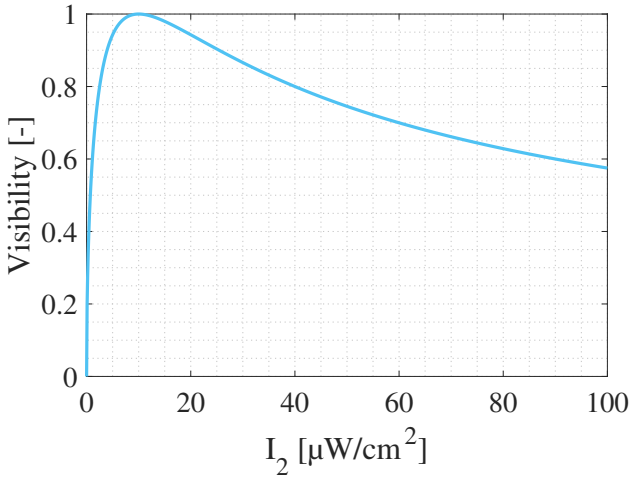

Figure 6.3.2: Analytical visibility as a function of the intensity of the second arm, I_2, for a fixed I_1.

Therefore, it was empirically determined that a visibility of 70% or higher is good enough. In this particular case, the intensity in each arm is

$$\begin{cases} I_1 = 5.36\ [\mu\text{W}]\,; \\ I_2 = 7.75\ [\mu\text{W}] \end{cases} . \tag{6.3.1}$$

Therefore, it is possible to compute the ratio of the two such that

$$\frac{I_2}{I_1} = 1.446\,. \tag{6.3.2}$$

Hence, using the definition of the optical density, OD, yields

$$OD = \log_{10}\left(\frac{I_2}{I_1}\right) = 0.16\,. \tag{6.3.3}$$

It is thus possible to conclude that a neutral density filter with $OD = 0.16$ is required to reach the same intensities in both arms. However, such absorptive filters are not available in the laboratory. Therefore, an optical density of 0.2 is placed in the path of the second arm. Hence, this leads to a new intensity of

$$I_{2,NDF} = 4.93\ [\mu\mathrm{W}]\,. \tag{6.3.4}$$

With this, it is possible to compute the visibility of the fringes that will be obtained with the Helium-Neon laser such that

$$V_{\text{He-Ne}} = \frac{2\sqrt{(5.36)(4.93)}}{5.36 + 4.93} = 0.9991 \Rightarrow V_{\text{He-Ne}} = 99.91\%\,. \tag{6.3.5}$$

The visibility with the Helium-Neon laser is excellent, nearly reaching its maximum, i.e., 100%. This means that bright and dark fringes will be visible without image post-processing.

6.4 Interferometry using a Helium-Neon laser

Using a Helium-Neon laser, providing a coherent light source at $\lambda = 633$ nm, is necessary to refine the alignment previously done. Indeed, it is quite certain that fringes will be obtained with such a source since the coherence length is very large. Nevertheless, as shown in the simulations, the angles of the mirrors, and therefore the angles between the beams in the path of interest, have a significant influence. Indeed, if the beams are perfectly co-aligned, the maximum of each beam emanating from the second beamsplitter will superimpose perfectly. However, if the angle between both beams is not zero, a slight phase shift may appear. Thus creating more and more fringes, as demonstrated by the simulations. This means that to perfectly co-align both beams, a flat fringe, resulting from a constant phase relation between the beams, is required.

6.4.1 Flat fringe

Typically situated between two interference fringes, the flat fringe is a region that appears uniformly bright, without any variation in intensity. There, maximum constructive interference happens, due to the constant phase relation between the light waves. However, obtaining the flat fringe does not ensure that the optical path difference is zero in the interferometer. It merely ensures that the beams are perfectly co-aligned. Therefore, reaching the flat fringe, or at least, getting close to it, is necessary to continue the tuning of the interferometer.

In order to obtain the flat fringe, it is important to choose which components to move. In this particular case, one arm was considered to be the reference length, such that only one mirror had to be moved, in only one direction. Indeed, this renders the alignment much

easier since instead of multiple degrees of freedom on each component, only one is required to correctly align the setup. The moving axis for the second mirror is shown in Figure 6.4.1.

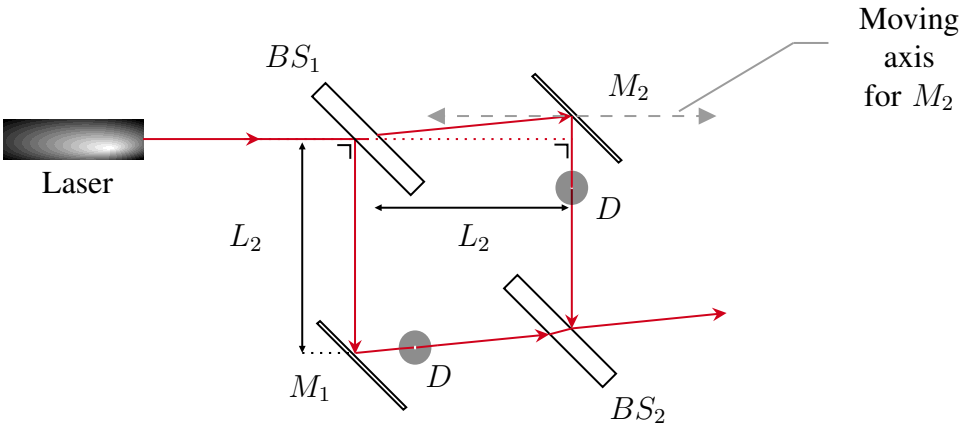

Figure 6.4.1: Moving axis for M_2 to obtain co-aligned beams.

However, moving the mirror in this way implies that the reflected beam does not strike the second beamsplitter exactly in the center, therefore inducing an optical path difference large enough to get independent wave trains in white light. Hence, it is mandatory to modify the angle of M_2 to ensure that the reflected beam indeed strikes the center of BS_2.

6.4.2 Tuning of the second mirror's position and angle

The first step to obtain a flat fringe is to find a starting position for M_2, i.e., a position where fringes are obtained. If the setup is well aligned as described previously, fringes should directly appear with the red coherent source. In this case, the fringes depicted in Figure 6.4.2 are obtained. This starting position is denoted as 00.

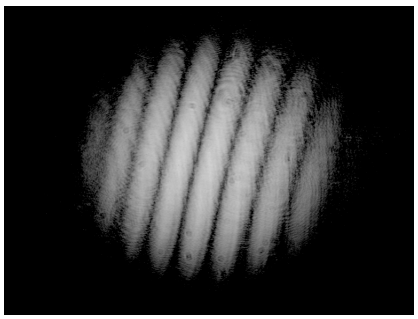

Figure 6.4.2: Initial fringes at the starting point 00 for M_2.

It is quite clear that several fringes are present, i.e., destructive and constructive interferences are happening. Nevertheless, as explained in the simulations, several fringes are present while only the flat fringe is wanted. Therefore, it is imperative to modify the knob of the platform supporting the mirror to co-align the beams. Hence, there are two possibilities, i.e., the mirror can either be moved to the left, or to the right. It is not possible to know apriori in which direction to move it, therefore, trial and error is necessary. In this case, moving

the mirror to the right proved to create more fringe, while moving it 50 microns to the left yielded the fringes shown in Figure 6.4.3.

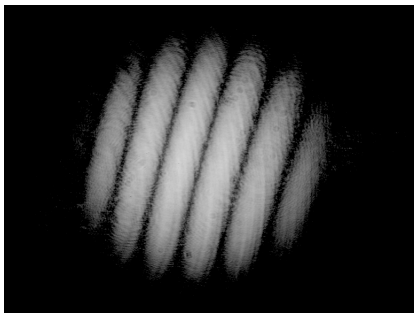

Figure 6.4.3: Fringes obtained by moving M_2 50 μm to the left.

Compared to the initial position, one can observe that six white fringes are obtained, instead of eight. Therefore, moving the mirror to the left, even more, will yield less and less fringes, up until reaching the flat fringe. After that milestone, more and more fringes will appear. Therefore, the flowchart depicted in Figure 6.4.4 must be precisely followed.

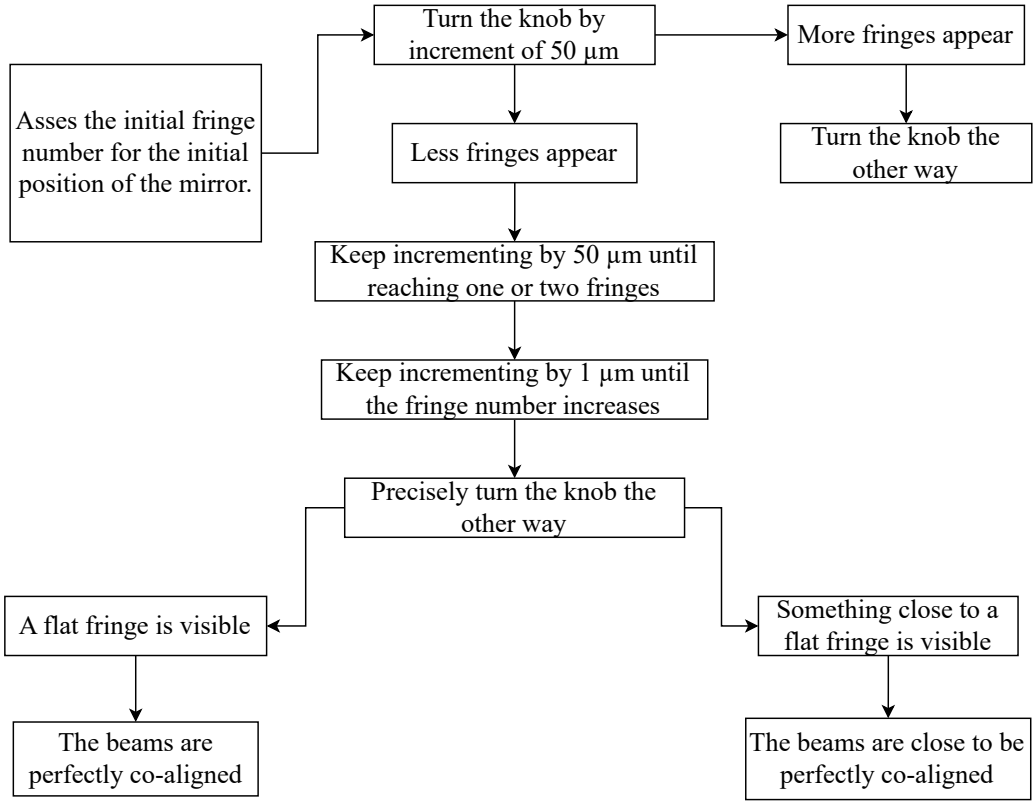

Figure 6.4.4: Flowchart of the methodology to obtain a flat, or nearly flat, fringe.

Moving the mirror 200 microns from its initial position yields nearly a flat fringe, as depicted in Figure 6.4.5.

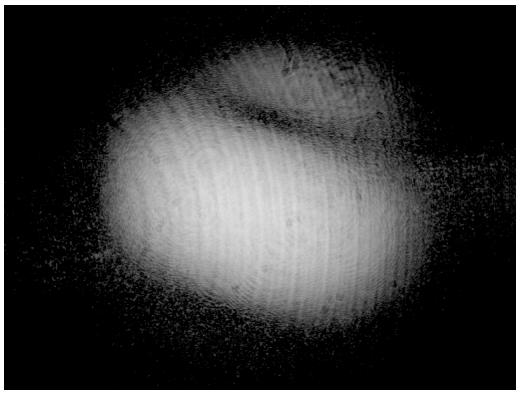

Figure 6.4.5: Fringe pattern for a 200 μm increment from the initial position.

At this point, the setup becomes very sensitive to anything, even a small move or even the voice of anyone close to the setup. Therefore, it is imperative to modify the position of the mirror with extreme care and precision. The knob increments are now 5 microns to prevent any unwanted change of behavior in the fringe pattern. That is, obtaining more fringes, i.e., over-incrementing leading to a position of the mirror beyond the position required for the flat fringe. Figure 6.4.6 shows that more than two fringes are visible, even with that small of an increment. In addition to that, the central fringe appears less large than the 200 microns increment.

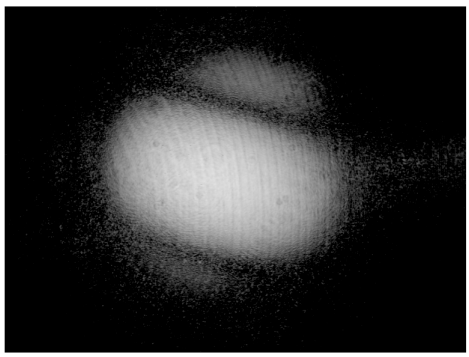

Figure 6.4.6: Fringe pattern for a 205 μm increment from the initial position.

Thus, one must turn the knob the other way, by an even smaller increment, i.e., 1 micron in this case. Figure 6.4.7 shows that the fringe pattern changes significantly, even with this small of an increment. However, it can observed that the fringe pattern for an increment of 203 microns is promising.

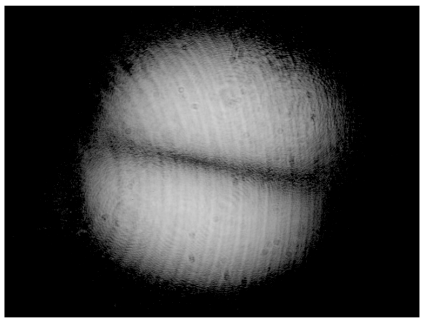

(a) Fringe pattern resulting from an increment of the knob by 201 μm.

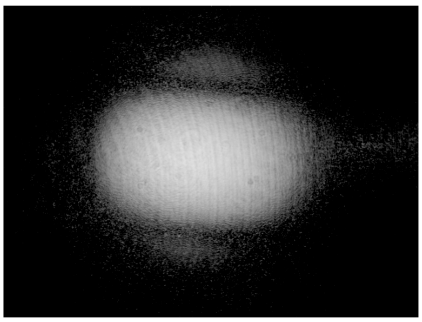

(b) Fringe pattern resulting from an increment of the knob by 203 μm.

Figure 6.4.7: Fringe patterns resulting from an increment of 201 and 203 μm, with respect to the initial position.

Observing the various patterns leads to some minor adjustments of the position around 203 microns. In particular, it is possible to place the knob in between two thicks, such that the increment is 0.5 μm. Moreover, by approximating the distance between each thick, it is possible to estimate more or less an increment of 0.1 microns. Following this, the closest configurations to a flat fringe is shown in Figure 6.4.8.

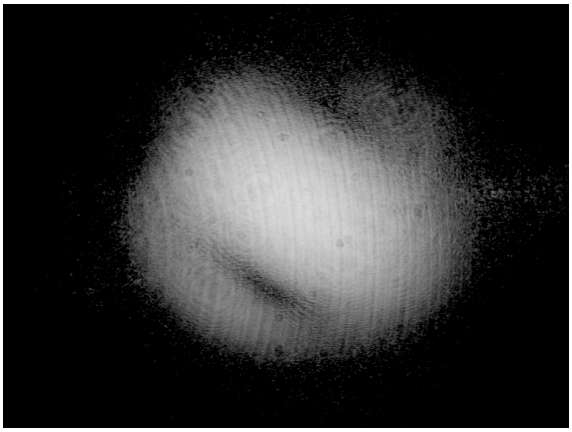

Figure 6.4.8: Fringe pattern resulting from an increment of the knob by 203.3 μm.

Finely tuning the knob to an approximate value of 203.3 μm yields an ever better behavior of the fringe pattern. Further refinement of the position of the mirror, close to a value of 203.3 μm led to the fringe pattern depicted in Figure 6.4.9. In this case, the flat fringe is obtained.

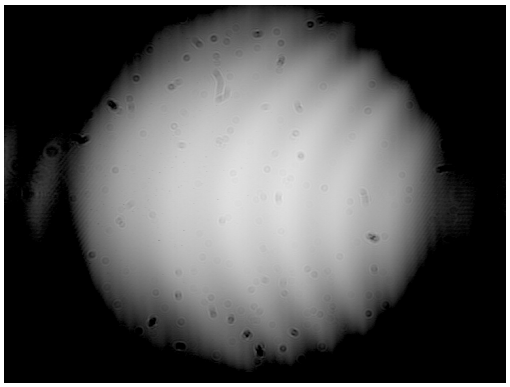

Figure 6.4.9: Flat fringe obtained around an increment of 203.3 μm with respect to the initial position of M_2.

It is still possible to identify some fringe patterns that appear slightly curved. Moreover, in the bottom right of the flat fringe, straight interference fringes can be observed. These patterns are likely due to internal reflection inside the camera, therefore, they are to be ignored.

The next step is to verify that the acquired image is indeed a flat fringe. This is done by considering a vertical and a horizontal band on the original image, delimited by a red rectangle. An average value of each pixel column (resp. line) is taken for the horizontal (resp. vertical) band. This value is then normalized such that the maximum possible intensity is $\overline{I} = 1$. Plotting the normalized and averaged intensity over Figure 6.4.8 yields the results depicted in Figure 6.4.10.

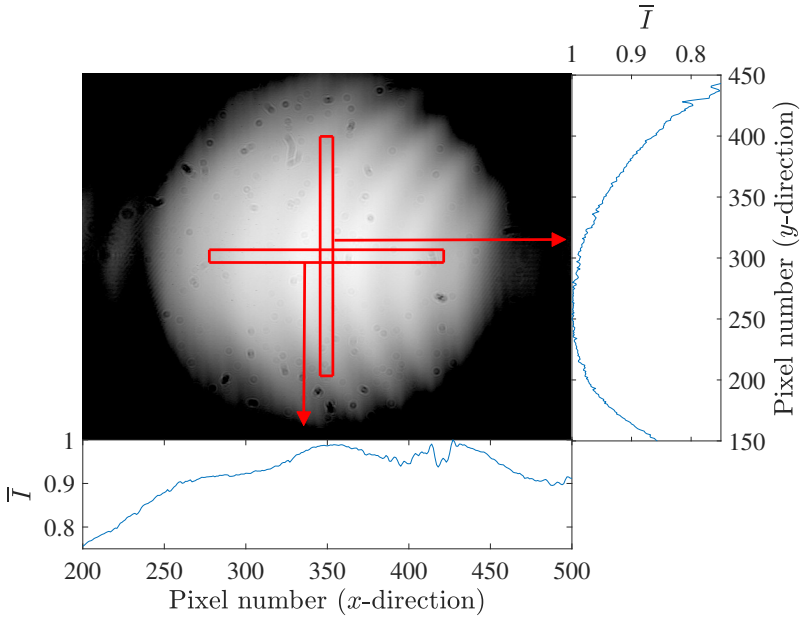

Figure 6.4.10: Normalized average intensity plotted over Figure 6.4.8.

It is quite clear that due to the several interference patterns resulting from various reflections inside the camera, the intensity profile is not as constant as could be expected. However, it is possible to illuminate the sensor with less intense light, either by placing a diverging lens in the beam's path, or by moving the camera away, which in both cases makes the beam's diameter larger. Hence, the incoming intensity is spread over a wider diameter. In this case, a lens was used to minimize the space used on the optical bench. This new approach, along with the normalized average intensity is depicted in Figure 6.4.11.

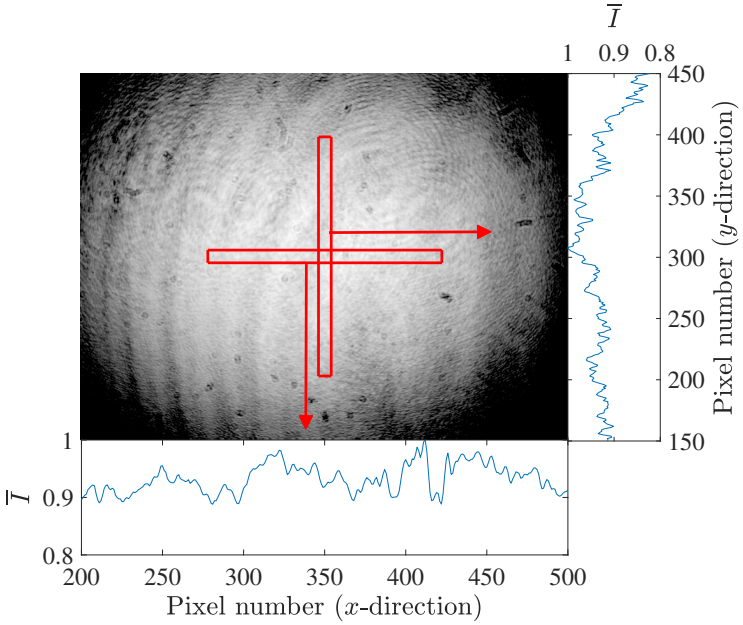

Figure 6.4.11: Normalized average intensity plotted over Figure 6.4.8 with a larger diameter.

From Figure 6.4.11, it is clearer that the intensity profile is more constant than without the lens. This is because, even though the internal reflections causing additional interference are reduced, some bent fringes can still be observed. The variations observed are therefore due to these parasitic fringes. Also, some dust particles on the sensor are visible in the image, which can cause intensity variation. Nevertheless, the intensity profile can still be considered constant, with an approximate of $\overline{I}_{\text{mean}} \approx 0.95$.

This flat fringe behavior for the intensity can finally be compared to a drastically different case, i.e., an interference pattern with numerous fringes, e.g., Figure 6.4.2. It is indeed of interest to do so to observe that the intensity will have extrema, varying over the pixel's direction. The results for such a case are shown in Figure 6.4.12.

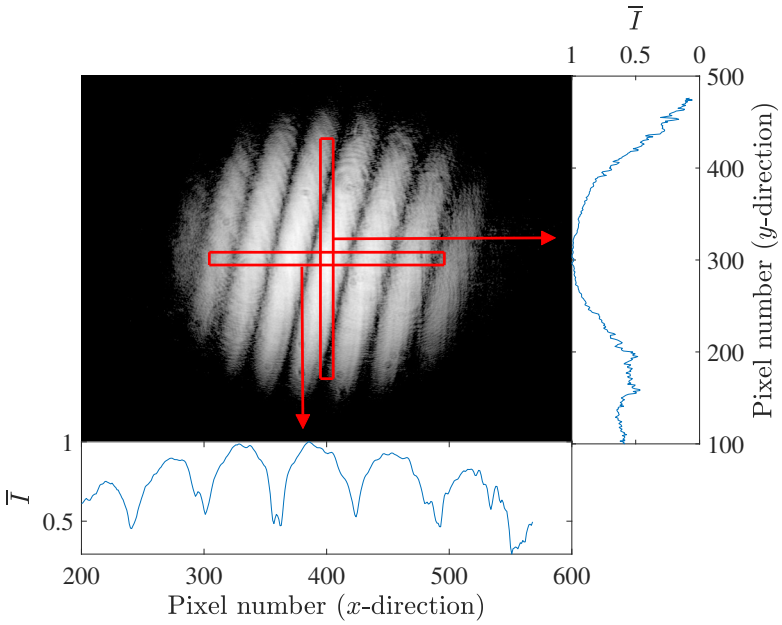

Figure 6.4.12: Normalized average intensity for the starting position of M_2 (Figure 6.4.2).

6.4.3 Additional considerations

Now that the flat fringe is obtained, it is crucial to consider that the wave trains might not be interfering perfectly with one another. That is, two maxima are interfering but these might not be the same maximum. This behavior is further explained in Figure 6.4.13.

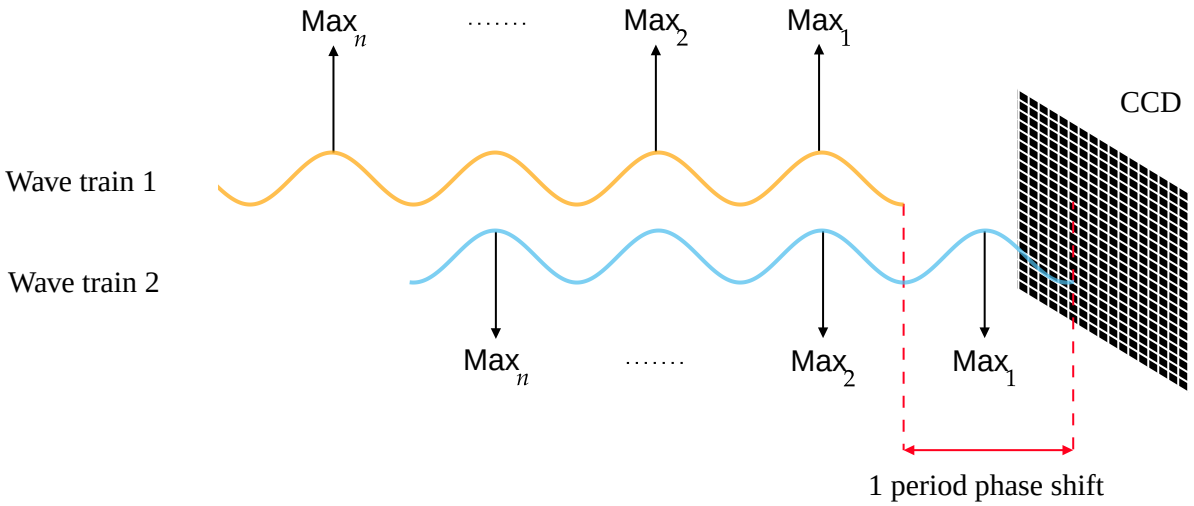

Figure 6.4.13: Phase shift between two wave trains leading to a flat fringe on the detector.

In this case, as an example, one period was considered for the phase shift between the wave trains. However, this phase shift could be of n-period, while still resulting in a flat fringe, given the fact that the maxima are perfectly interfering with one another. This shift is obviously due to unequal optical path lengths between the arms. Therefore, further tuning

of the position and angle of M_2 might be required when using a white incoherent source. Unfortunately, due to the huge coherence length of the He-Ne laser, it is hard to predict apriori this behavior. Therefore, trial and error using another source is required.

The final aim of this Master's thesis is to have a Mach-Zehnder setup with an incoherent broadband source in order to perform holography, particularly in the thermal infrared region. For that purpose, a suitable visible source with roughly the same coherence properties will be searched. In the next section, the potentialities of broadband visible sources will be analyzed, along with the use of selective filters. These filters will narrow the broadband source, thus increasing the coherence length. Through various filters, this coherence length will be progressively decreased up until reaching a configuration without filter, i.e., with very low coherence.

6.5 Interferometry using a white incoherent source

The first step to performing interferometry with a white incoherent source is to find a source suitable for the experiment. A light source powerful enough, i.e., with a sufficient intensity, is required. At first, the *Solis High Power LEDs* from Thorlabs (Figure 6.5.1a) was selected. This source provides an incoherent light in the range of $\lambda \in [350; 850]$ nm. However, it proved to be impossible to obtain any interference pattern with such a source, due to collimation problems. Therefore, an alternate light source was selected, i.e., the *SuperK Compact* (Figure 6.5.1b), providing collimated light in the range of $\lambda \in [400; 2400]$. Therefore, supplementary considerations will be taken into account for that particular source.

(a) Solis High Power LEDs from Thorlabs [34].

(b) SuperK Compact from NKT Photonics [35].

(c) Collimated source powered by the SuperK Compact [35].

Figure 6.5.1: Various high-power white light sources used in the experiments.

6.5.1 Solis High Power LEDs

This Thorlabs' source provides white incoherent light with sufficient power, however, with the material available in the optical laboratory, it was not possible to create a collimated beam. Indeed, the only possible collimation that was reached was by using a lens and a diaphragm. That is, one-to-one imagery of the diaphragm was performed. However, the intensity was too low to image a beam approximately as large as the one provided by the He-Ne laser. This is due to the diaphragm greatly reducing the intensity of the source. A schematic of one-to-one imagery with a convex lens is shown in Figure 6.5.2.

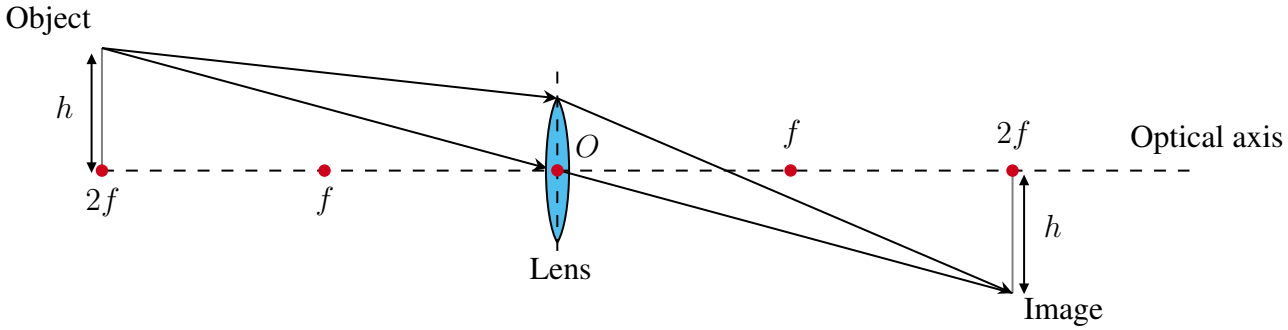

Figure 6.5.2: Schematic of the one-to-one imagery of an arbitrary object.

It can indeed be shown using the lens formula, i.e.:

$$\frac{1}{f} = \frac{1}{u} + \frac{1}{v}\,, \tag{6.5.1}$$

that by placing an object at two times the focal length of the lens, $2f$, the image is also located at $2f$. That is

$$\begin{cases} u = 2f \\ v = 2f \end{cases} \Rightarrow \frac{1}{f} = \frac{1}{2f} + \frac{1}{2f} \iff \frac{1}{f} = \frac{1}{f}\,, \tag{6.5.2}$$

which confirms that placing the object at $2f$ yields an image of the same size at a distance $2f$ from the lens.

Therefore, since the diameter of the diaphragm must be greatly reduced, almost all of the intensity is lost. Hence, due to the use of a spectral filter, the intensity, which reduces the intensity even more, will almost be zero after passing through the interferometer. This is not acceptable, thus, another light source must be chosen.

6.5.2 SuperK compact

The superK compact provides an incoherent collimated source within a large spectral band, i.e., from 400 to 2400 nm, as shown in Figure 6.5.3. It achieves this through a combination

of mode-locking and nonlinear optical effects in a specialized fiber. Ultrashort pulses of light with high peak powers are produced by the mode-locking, this ensures intense bursts of energy. These are then directed into a nonlinear optical fiber, thus inducing various nonlinear processes, and broadening the spectrum of each pulse. The output obtained is a continuum of wavelengths featuring a lot of spectral lines across the spectrum. In particular, these lines correspond to the specific frequencies generated through the nonlinear interactions in the fiber [35]. Therefore, it is necessary to get rid of any infrared radiation emanating from the source. This will provide a clean white incoherent source, which in turn will enable the alignment of the interferometer in white incoherent light.

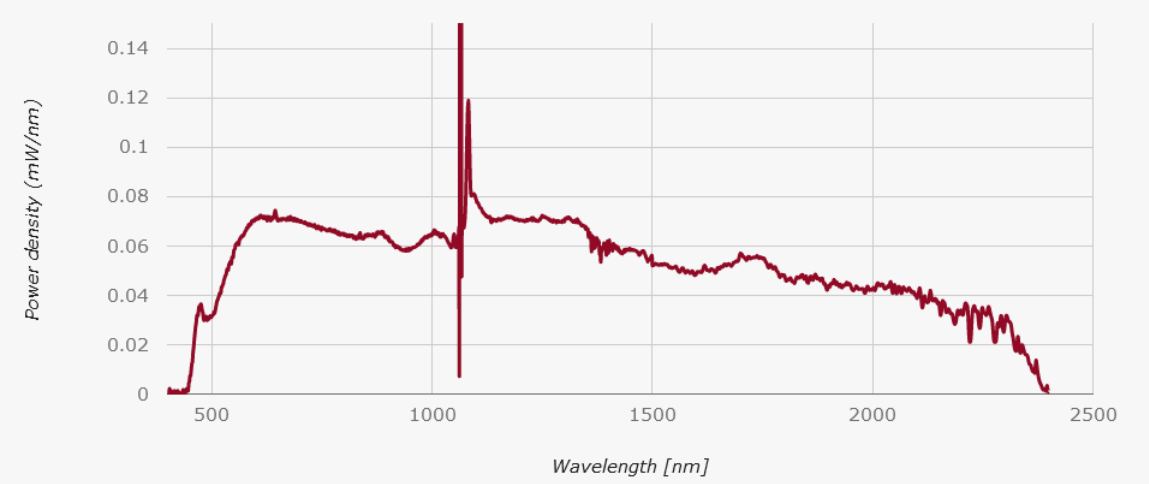

Figure 6.5.3: SuperK Compact typical spectrum [35].

The collimated beam is unpolarized and its diameter varies with respect to the wavelength, as depicted in Table 6.1.

Wavelength [nm]	Beam diameter [mm]
532	1
1100	2
2000	3

Table 6.1: Beam diameter with respect to the wavelength for the collimated source powered by the SuperK Compact.

6.5.2.1 Elimination of the infrared radiations

To eliminate the infrared radiation while keeping most of the visible wavelength, it is possible to use a dichroic mirror. Thankfully, one was available at the laboratory.

The dichroic mirror is coated with multiple layers of dielectric materials. When hit by light, some wavelengths are reflected, while others can pass straight through. This is because the thickness and refractive index are designed to produce constructive interference for the reflected wavelengths of interest. On the other hand, destructive interference are produced for

the transmitted wavelengths. Therefore, specific wavelengths of light are reflected while others are transmitted. This type of optical component has high selectivity and efficiency, as it can reflect up to 99% of the desired wavelengths while transmitting all the other wavelengths.

In this case, the Dichroic Mirror Short Pass (DMSP) 1000 was used. Its transmission and reflectance properties are given in Figure 6.5.4.

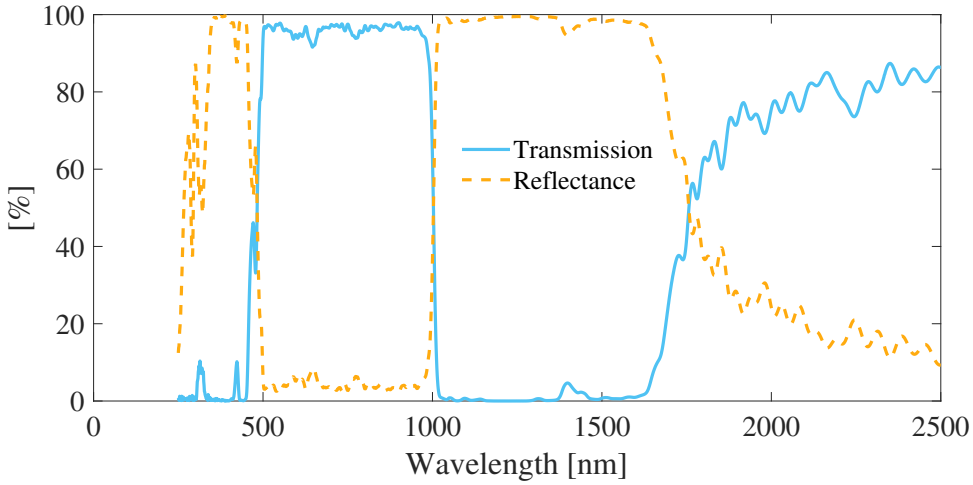

Figure 6.5.4: Transmission and reflectance with respect to the wavelength for the DMSP1000, considering unpolarized light (data obtained from [36]).

Therefore, visible and NIR wavelengths will successfully be transmitted, roughly from 500 to 1000 nm. That it, the superK compact produces a white collimated source, i.e., a white laser. However, due to the wavelength range, the source is incoherent! Hence, interferometry can now be performed with a white incoherent source. The setup with the dichroic mirror and the white laser is presented in Figure 6.5.5. In addition to that, the light going into the light trap is shown in Figure 6.5.6.

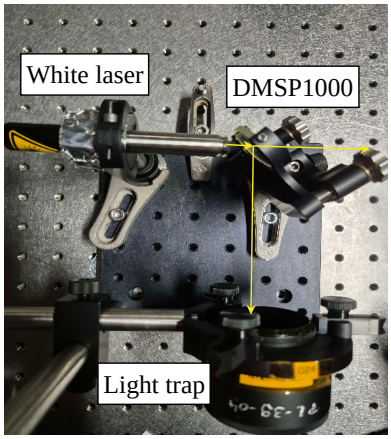

Figure 6.5.5: Ray path of the white laser impacting the dichroic mirror, leading to light being transmitted and, reflected then trapped.

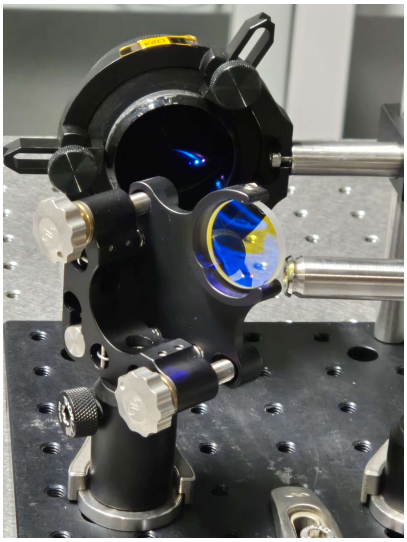

Figure 6.5.6: Unwanted light directed into the light trap.

After the setup shown in Figure 6.5.5, a mirror is placed before the interferometer, such that the incoming ray follows exactly the same path as the one obtained with the He-Ne laser. This is done, once again, by using two diaphragms.

6.5.2.2 Safety considerations

The reflected part of the light, which mostly sits in the infrared, is directed into a light trap for safety purposes. Nevertheless, it is important to wear glasses suitable for such wavelength ranges. Even though light with $\lambda > 1000$ nm falls into a light trap, it is important to cover all the wavelength ranges to avoid any radiation reaching one's eyes. For this purpose, the transmission and reflectance shown in Figure 6.5.4 are plotted along with the optical density of the LG11 glasses in Figure 6.5.7. These glasses provide effective protection against wavelength in the range of $375 \geq \lambda \geq 600$ [nm]. For a reminder, the optical density, OD, is a measure of the attenuation of light as it passes through a medium. In particular, one can write

$$OD = -\log_{10}\left(\frac{I_{\text{transmitted}}}{I_{\text{incident}}}\right). \tag{6.5.3}$$

Hence,

$$I_{\text{transmitted}} = I_{\text{incident}} \cdot 10^{-OD}. \tag{6.5.4}$$

For example, considering an incident intensity of

$$I_{\text{incident}} = 100 \text{ W/m}^2\,, \tag{6.5.5}$$

and an optical density of

$$OD = 7.5\,, \tag{6.5.6}$$

the transmitted intensity is

$$I_{\text{transmitted}} = 3.16 \times 10^{-6} \text{ W/m}^2. \tag{6.5.7}$$

Therefore, the LG11 glasses are suitable for the wavelength ranges considered, as proven by Figure 6.5.7.

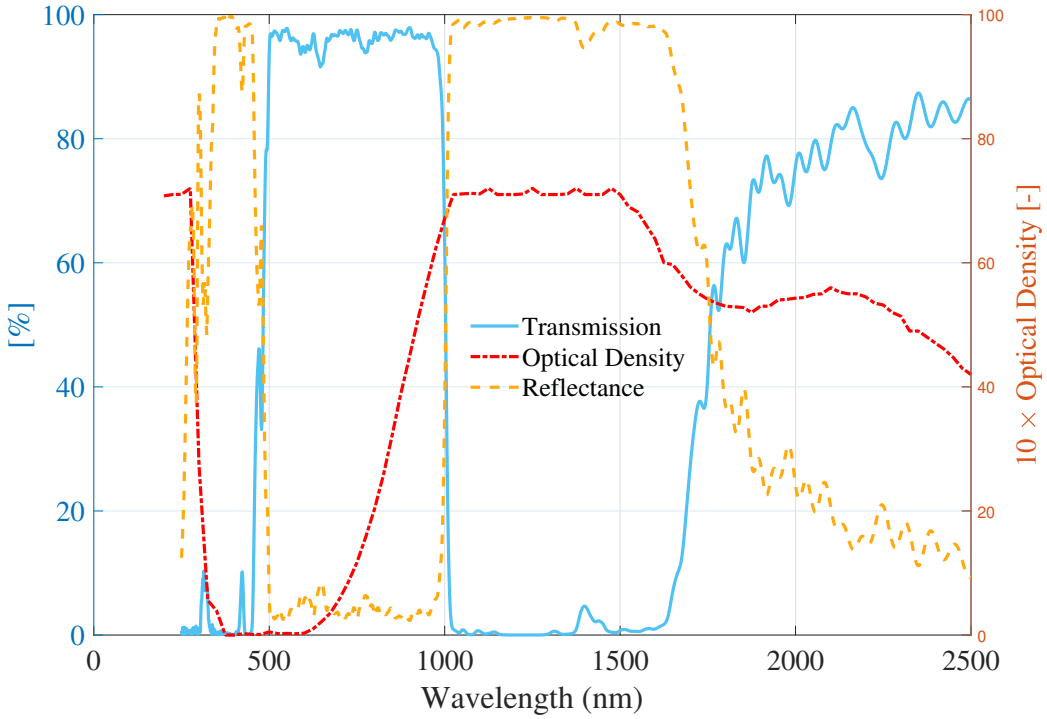

Figure 6.5.7: 10 × Optical density of the LG11 glasses compared to the transmission and reflectance of te DMSP1000, considering unpolarized light (data from [36, 37]).

It is evident that the LG11 glasses are indeed suitable for this experiment as they exhibit the largest optical density in the 1000-2500 nm wavelengths.

6.5.2.3 Interferometry with a narrow band spectral filter

Due to the presence of a wedge, as well as the thickness of the beamsplitters, obtaining interference patterns with white incoherent light directly proved to be difficult, if not impossible. The white incoherent light emits over a large band, in this case, in the range of 500-1000 nm. Therefore, this requires a nearly zero-OPD in the arms. This is due to the low temporal coherence, indeed, one could compute the coherence lengths for the transmitted light, i.e.:

$$L_c = \frac{\lambda_0^2}{\Delta\lambda} \Rightarrow \begin{cases} L_{c,1} \approx \dfrac{750^2}{1000-5000} & = 1125 \text{ [nm]} \\ L_{c,2} \approx \dfrac{2125^2}{2500-1750} & = 6021.67 \text{ [nm]} \end{cases} . \tag{6.5.8}$$

Since $L_{c,1}$ is the most restrictive wavelength, it must be considered such that the OPD should be as

$$\text{OPD}_{\text{SuperK}} \leq L_{c,1} = 0.001725 \text{ [mm]}. \tag{6.5.9}$$

Thus, to facilitate the alignment, a spectral filter centered at $\lambda_{0,\text{filter}_1} = 672.4$ nm was chosen. Moreover, it has a bandwidth of $\Delta\lambda = 3$ nm. Therefore, the coherence length is

$$L_{c,\text{filter}_1} = \frac{672.4^2}{3} = 150707 \text{ [nm]} = 0.15 \text{ [mm]}. \tag{6.5.10}$$

This is much more flexible than working directly without any filter, i.e., with a larger spectrum. The light beam emanating from the filter is shown in Figure 6.5.8.

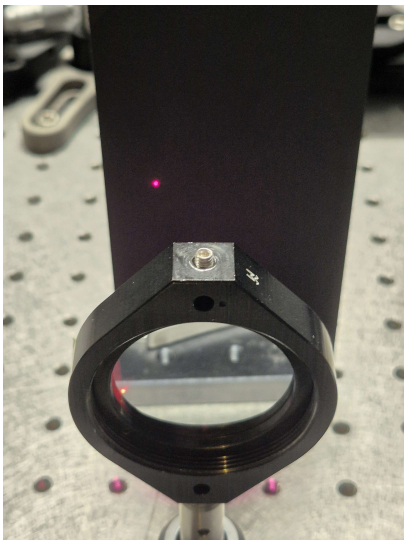

Figure 6.5.8: Red beam ($\lambda = 672.4$ nm) transmitted by the narrow band ($\Delta\lambda = 3$ nm) filter.

This red-filtered beam then goes through the interferometric setup, onto the camera. However, the filter greatly reduces the intensity, and, in addition to that, the interferometric setup will reduce it even more.

To obtain the interference pattern, the knob of M_2 must be turned, one way or the other, in a trial-and-error fashion. However, if the setup was close to a flat fringe beforehand, fringes should appear immediately, without any tuning. In this case, small adjustments were required to obtain the interference pattern. This means that the perfect co-alignment of the beams is not respected anymore. Hence, more fringes than the ones obtained with the He-Ne laser are visible. In addition to that, even with high camera gain, the interference pattern is hard to visualize due to the low intensity at the output of the interferometric setup. A first step to enhance the visibility of the fringes was to slightly separate the beam, i.e., they are not superimposed on the camera. These results are depicted in Figure 6.5.9.

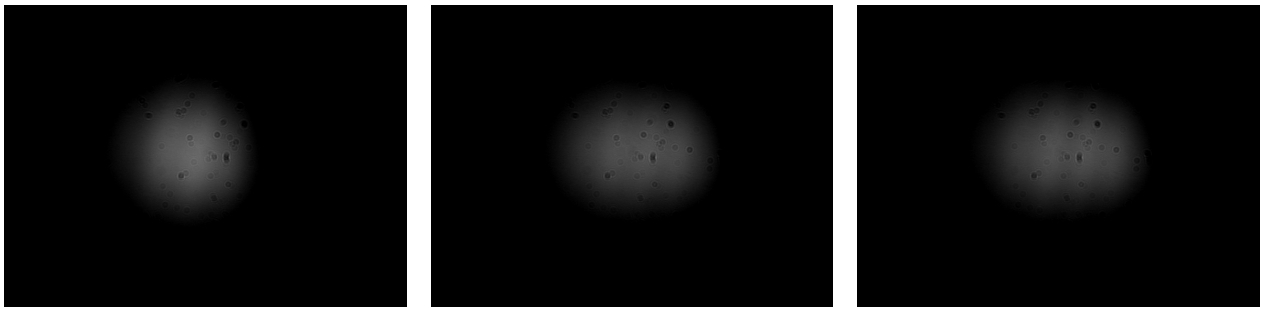

(a) Superimposed beams. (b) Slightly separated beams. (c) Fully separated beams.

Figure 6.5.9: Interference patterns obtained with the narrow band filter. The patterns show superimposed, slightly and totally separated beams.

It is however possible to post-process the image and enhance the visibility. This is done by acquiring a flat field of one beam and then subtracting it from the original image. This was done for Figure 6.5.9c, the results direct comparison between the two is made in Figure 6.5.10.

(a) Original acquisition of the separated beams. (b) Post-processed image.

Figure 6.5.10: Direct comparison between the original image from Figure 6.5.9c and the post-processed image.

The fringes are clearly visible on the post-processed image.

6.5.2.4 Interferometry with a large band spectral filter

The second filter used possesses a central wavelength of $\lambda = 633$ nm, with a bandwidth of $\Delta\lambda = 50$ nm. Therefore, the coherence length of the light emanating out of this filter is given by

$$L_{c,\text{filter}_2} = \frac{633^2}{50} = 8813.7 \text{ [nm]} = 0.008\text{[mm]}. \tag{6.5.11}$$

This coherence length is less permissive than for the previous filter, hence, it will allow further alignment of the interferometric setup. However, with such a filter, the intensity at the output is larger than for the previous one. Therefore, the camera saturates. To avoid

this saturation, it is possible to use, once again, neutral density filters. However, since the beamsplitters' properties vary with the wavelength, and since the wavelength used is far from the optimized wavelength, it is hard to choose neutral density filters that will be suited for various wavelength ranges. Therefore, this choice of filters is based on trial and error, considering how much light will reach the camera. This process is based on the flowchart depicted in Figure 6.5.11.

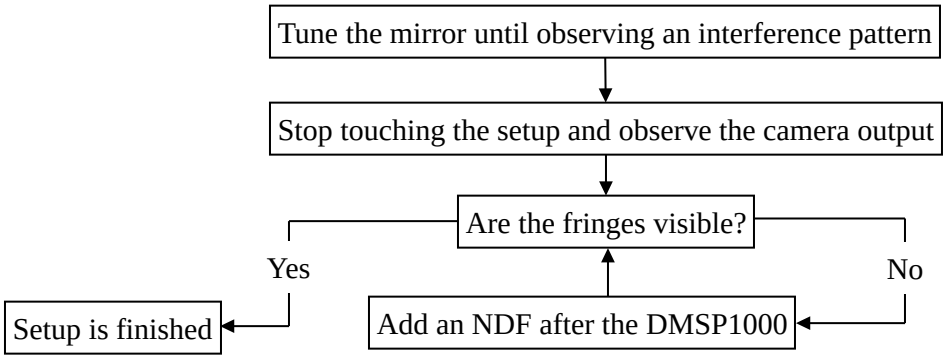

Figure 6.5.11: Flowchart to obtain better visibility of the fringes.

Adding neutral density filters proves to work because the wavelength changes, hence, the intensity in each arm is not close to being the same as previously. Therefore, one of the beams is *blinding* the other. This results in a nearly invisible interference pattern. Of course, the visibility is not perfect, such that post-processing, i.e., flat field removal, is necessary. The fringes obtained with the appropriate NDFs, along with the post-processed result are shown in Figure 6.5.12.

(a) Original acquisition. (b) Post-processed image.

Figure 6.5.12: Fringe pattern obtained with the larger band spectral filter.

6.5.2.5 Interferometry in full-spectrum white light

Concerning the interferometry in white light, the filters are not used anymore. Therefore, the interferometry is performed within the 500-1000 nm wavelength range, where the coherence

length is given by $L_{c,1}$ (Equation 6.5.8). To achieve any fringes, the position of the second mirror must be finely tuned, with extreme care and precision. Indeed, the coherence length is very small. The patterns obtained, before and after suppression of the flat field are shown in Figure 6.5.13.

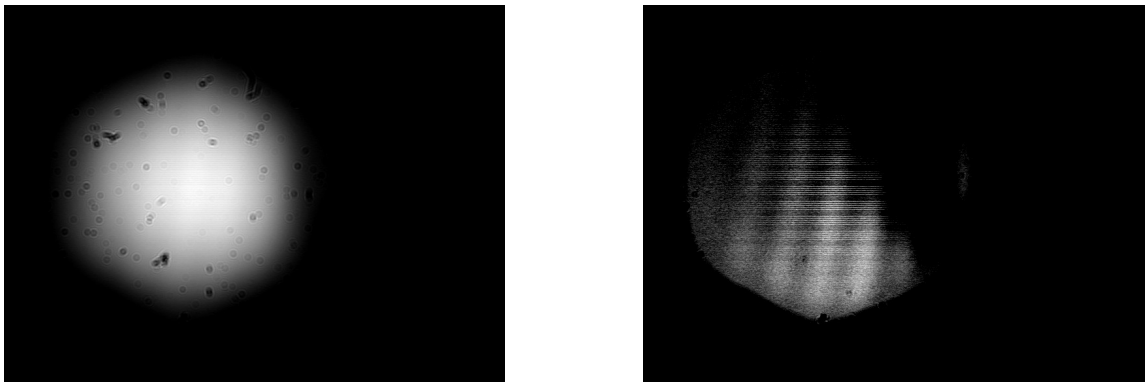

(a) Original acquisition. **(b)** Post-processed image.

Figure 6.5.13: Comparison of the Fringe patterns obtained with the full spectrum white light before and after post-processing.

6.6 Conclusion on the alignment

Overall the alignment of the interferometer was successfully performed. Nevertheless, it is worth noting that in white light, filtered or not, the fringe patterns are not as visible as before. This is because the beamsplitters are not manufactured to work at that particular wavelength but in the LWIR, and therefore, the intensity in each arm is not equal or close to equality. Therefore, neutral density filters were used to try to reduce this phenomenon. This was not successful, however, removing the flat field from the pattern proved to work very well. Therefore, flat field acquisition is necessary with the beamsplitters used. This means that, in the infrared, this will also have to be done.

In addition to that, it is interesting to understand that, compared to the fringes obtained with the He-Ne laser, the patterns acquired in white light contain more fringes. This is because small adjustments were made to the position of the second mirror. Therefore, the beams are not co-aligned perfectly anymore. Due to time constraints, the setup was left with nearly co-aligned beams. Indeed, interference patterns can easily be acquired, they will just not be perfect. Hence, the optical path difference is close to zero, which means that the setup was successfully aligned.

This departure from the perfect co-alignment also explains that some parts of the light of each beam do not interfere with the other. This is likely due to small optical path variations, caused by the small angle between both beams. Therefore, this results in background noise, which is removed with the flat-field post-process. Nevertheless, this noise causes the visibility

to swiftly diminish, which explains why the interference patterns on the original images are hard, or impossible, to visualize.

6.7 Interferometry in the infrared

To perform interferometry in the infrared, there are two possibilities, i.e., use a coherent source (e.g., CO_2 laser), or an incoherent one (e.g., self-emitting object).

Concerning the coherent sources, these are not of interest to this Master's thesis. Indeed, the coherence length of a CO_2 laser, considering a central wavelength of 10.6 μm, and an arbitrary bandwidth of 0.1 nm is

$$L_{c,CO_2} = \frac{10600^2}{0.1} = 1123.6 \text{ [m]}. \tag{6.7.1}$$

This length is enormous, therefore, the interferometric setup will produce fringes, no matter the alignment. Hence, these types of sources are not of interest.

On the other hand, self-emitting sources are inherently incoherent. Indeed, they output radiation at various wavelengths. This can be demonstrated by using Planck's (Equation 4.1.1) and Wien's (Equation 4.1.2) laws, assuming a black body. Indeed, the intensity with respect to the wavelength can be plotted as depicted in Figure 6.7.1. It can be observed that the intensity is larger than zero over a wide range of wavelengths, depending on the temperature. Therefore, this results in a short coherence length, compared to the CO_2 laser. In addition to that, in thermal emission sources, photon emission is due to the random vibration of atoms and molecules within the source. These motions are chaotic by nature, therefore, this leads to a superposition of waves with varying phases and amplitudes. Hence, this chaotic motion yields radiation that lacks a fixed phase relationship, which leads to incoherence. Finally, in self-emitting sources, each photon is emitted independently with a random phase. This means that, once again, there is a lack of a fixed phase relationship between photons, leading to temporal and spatial incoherence [26].

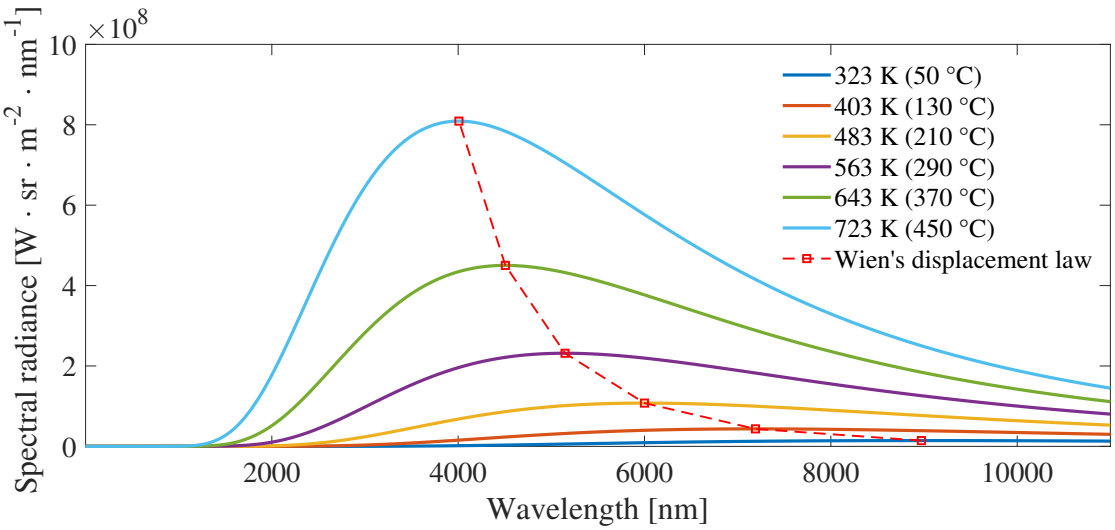

Figure 6.7.1: Spectral radiance with respect to the wavelength for a black body using Planck's law. Wien's displacement law is also shown.

Therefore, a self-emitting source, producing incoherent light over a broadband of wavelengths will be used. For the sake of this experiment, a welding iron, with a surface temperature of 450°C will be used. In addition to that, to reduce the wavelength range, a filter will be used. This filter has a central wavelength of 10600 nm and a bandwidth of 500 nm. Therefore, the coherence length resulting from these considerations is

$$L_{c,\mathrm{IR}} = \frac{10600^2}{500} = 224720 \text{ nm} = 0.225 \text{ [mm]}. \tag{6.7.2}$$

It is worth noting that this coherence length is larger than the one obtained for white light, i.e.:

$$L_{c,\mathrm{IR}} = 0.225 \text{ [mm]} >>> 0.0017 \text{ [mm]} = L_{c,1}. \tag{6.7.3}$$

Hence, as expected, fringes should be visible right away in the infrared. This setup is then supplemented by a converging lens and a pinhole, as it has been done in the visible domain by Pedrini et al. [22]. To that, it is necessary to consider the incoming flux coming from the object itself. To understand this concept, the emission of radiation from a surface into the surrounding hemispherical space is depicted in Figure 6.7.2.

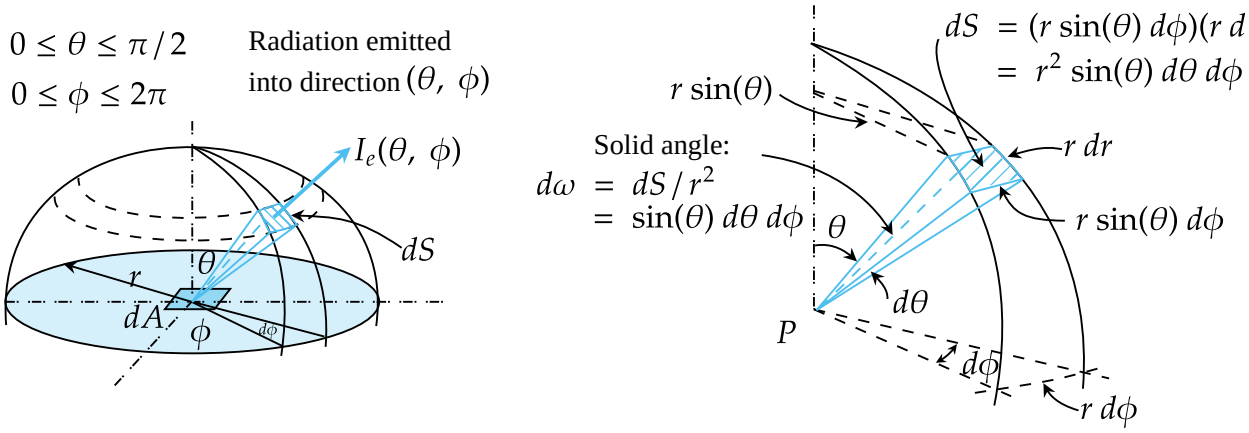

Figure 6.7.2: Emision of radiation from a differential surface element into the surrounding hemispherical space through a differential solid angle (adapted from [38]).

The differential solide angle, $d\omega$, subtented by a differential area dS on a sphere of radius r can be expressed as

$$d\omega = \frac{dS}{r^2}. \tag{6.7.4}$$

Since dS is viewed from the center of the sphere, it is normal to the direction of viewing. More generally, the differential solid angle subtended by a differential surface dA when viewed from a point at a distance r from dA is expressed as

$$d\omega = \frac{dA}{r^2}. \tag{6.7.5}$$

Small surfaces viewed from relatively large distances can approximately be treated as differential areas in solid angle calculation such that

$$\omega \approx \frac{A}{r^2}. \tag{6.7.6}$$

Considering the emission of radiation by an area element dA of a surface, as depicted in Figure 6.7.2, radiation is emitted in all directions into the hemispherical space. The radiation emanating from the surface area dS is proportional to the solid angle subtended by dS. The radiation intensity for emitted radiation, $I_e(\theta, \phi)$, is defined as the rate at which radiation energy is emitted in the $(\theta,\ \phi)$ direction per unit area normal to this direction and per unit solid angle about this direction. In simpler terms, it is the power per unit area per unit solid angle emitted in the direction $(\theta,\ \phi)$. Therefore, for the whole sphere, the total power is given by

$$\begin{aligned} P &= \int_\Omega I_e(\theta,\phi)\,d\omega \\ \omega = \sin(\theta)\,d\theta\,d\phi \rightarrow &= \int_0^{2\pi}\int_0^{\pi} I_e(\theta,\phi)\sin(\theta)\,d\theta\,d\phi. \end{aligned} \tag{6.7.7}$$

The differential power emitted into the differential solid angle $d\omega$ is

$$dP = I_e(\theta, \phi)\, d\omega. \tag{6.7.8}$$

Hence, substituing $d\omega$ in spherical coordinates (see Equation 6.7.4) yields

$$dP = I_e(\theta, \phi)\frac{dS}{r^2} \tag{6.7.9}$$

Since the differential power is spread over an area $dS = dA$ at a distance r, the intensity at the same distance from the source is the power per unit area, i.e.:

$$I = \frac{dP}{dA} = \frac{I_e(\theta, \phi)}{r^2}. \tag{6.7.10}$$

This shows that the radiation intensity decreases with the square of the distance from the source. Quite logically, this happens because the same amount of emitted power is distributed over a larger surface as the distance from the source increases. This concept is of the utmost importance while working with self-emitting objects, as the intensity provided by the self-emitting source will rapidly decrease over the distance. Therefore, this must be considered in the choice of temperature and travel distance through the setup to the camera.

6.7.1 Camera

The camera chosen for this experiment was the Gobi Xenics 640 (Figure 6.7.3). This camera employs an uncooled microbolometer detector with a 640 x 480 pixel resolution. The use of an uncooled camera in this case is important since cooled cameras are subject to vibrations. In turn, this could be problematic for the acquisition of holograms.

Figure 6.7.3: Gobi 640 IR camera [39].

6.7.2 Setup and considerations

In order to create the setup for the self-emitting object in the thermal infrared, first, a lens must be chosen. The choice is based on the length of the arms of the interferometer. In this case, the arms are approximately 50 cm long. Therefore, based on the principle depicted in Figure 6.5.2, a lens of at least $f = 15$ cm is required. Indeed, this leaves space after and

before the setup to place the object and the camera, and successfully produces a one-to-one image of the object, as shown in Figure 6.7.4. A lens of $f = 200$ mm was found in the lab, therefore, to effectively provide a one-to-one image, the total length between the object and the camera through the interferometer is

$$L_{\text{Object - Camera}} \approx 800 \text{ [mm]}. \tag{6.7.11}$$

Thus, this leaves an approximate 30 cm length to place the object and the camera. It is however still important to ensure that the length between the object and the lens, and the length between the lens and the camera is $L = 2f$.

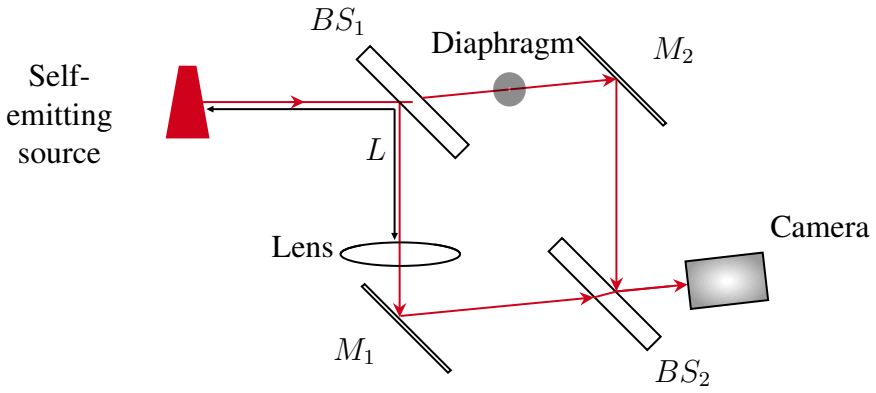

Figure 6.7.4: Setup for the thermal infrared.

Before M_2, the diaphragm is closed to its maximum such that it acts as a pinhole, thus producing a spherical wavefront in that arm. Hence, this arm serves as the reference beam for the holographic setup, while the other arm corresponds to the object beam. This choice was based on the properties of the beamsplitters, indeed, BS_1 transmit 99% of the incoming light, while reflecting the leftover percent. Therefore, since the pinhole greatly reduces the intensity, it must be placed in the most intense arm.

6.7.3 Alignment of the camera

The wavelength of the light emanating from the self-emitting object is different from that of visible sources. Thus, the refractive index of ZnSe is slightly different, causing the light rays to potentially hit different spots compared to the visible domain. Additionally, since infrared light is invisible to the naked eye, the camera must be correctly aligned with the beams. It is therefore important to align the camera such that a clear image of the self-emitting object is acquired. This can be done by blocking the reference arm and moving the camera on the optical bench until obtaining a clear image of the object. After careful alignment, the camera output is depicted in Figure 6.7.5. However, due to the beamsplitters used, the intensity reaching the camera is very low. Indeed, only one percent of the light emanating from the self-emitting object is going through the lens. Then, in the second beamsplitter, 50% of that light is transmitted such that the intensity varies as

$$I_0 \to 0.01 I_0 \to 0.005 I_0. \tag{6.7.12}$$

This intensity is very small but the choice of other beamsplitters was not possible. This renders this constraint impossible to overcome. Nevertheless, the first step for better visibility was to contour the object with white lines.

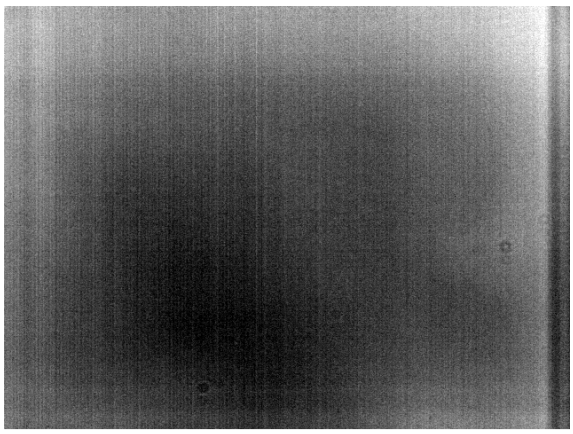

(a) Original acquisition of the self-emitting object.

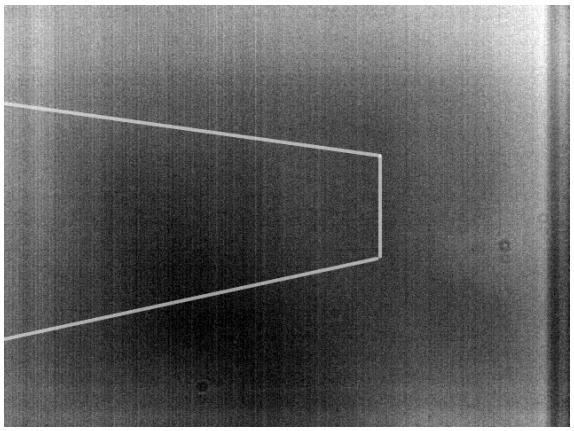

(b) Original acquisition with contouring of the self-emitting object for better visibility.

Figure 6.7.5: Original and contoured acquisition of the self-emitting object.

It is quite clear in Figure 6.7.5a that the object fades into the background noise. This is due to the low intensity outputted by BS_2. Another possibility to enhance visibility was to suppress the noisy background, as depicted in Figure 6.7.6. However, the intensity is so low that the object is still hard to visualize. Once again, the object is also contoured for better visibility.

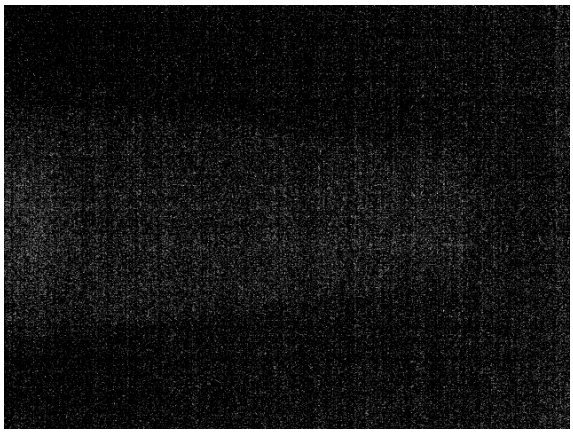

(a) Original acquisition after background suppression.

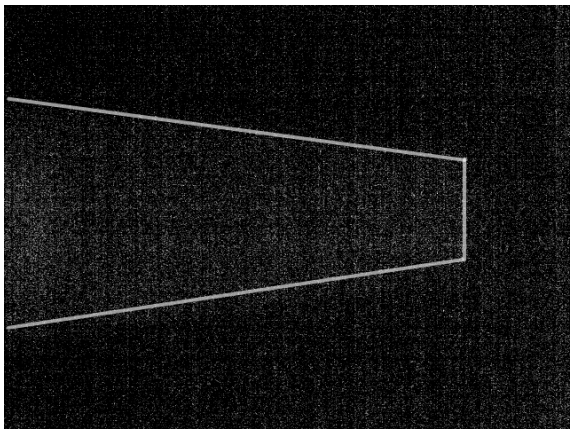

(b) Original acquisition after background suppression and contouring.

Figure 6.7.6: Original and contoured acquisition of the self-emitting object after background suppression.

From this, it is supposed that holographic reconstruction will be challenging, if not impossible due to the low intensity.

6.7.4 Results and analysis

For the setup shown in Figure 6.7.4, it was possible to capture the image presented in Figure 6.7.7.

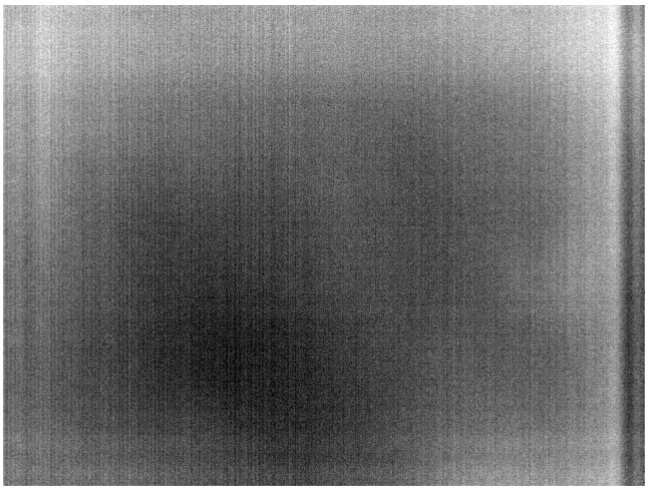

Figure 6.7.7: Image of the interaction of reference and object beams for a self-emitting object using the setup depicted in Figure 6.7.4.

Nothing is visible in that image, not even a faint interference pattern, which indicates that the signal of interest is mixed with the background noise. Therefore, the background was once again suppressed as depicted in Figure 6.7.8.

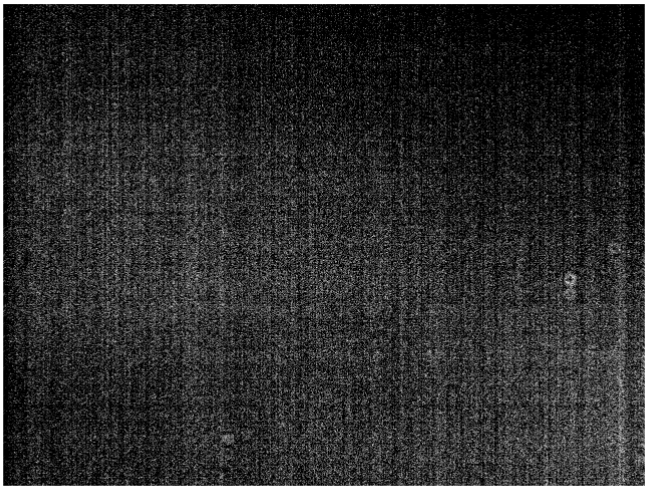

Figure 6.7.8: Figure 6.7.7 with the background suppressed.

In this case, even after background suppression and tuning of the camera's parameter to obtain better visibility of the scene, only noise appeared on the screen. No interference pattern is visible, most likely due to the low intensity after passing through the interferometric setup. Therefore, the beamsplitters might be the main problem in this case. The noise would not be as predominant if the first beamsplitter provided more than a single percent reflection. Thus, having a first beamsplitter reflecting more light, e.g., 10 or 30% could overcome this background noise problem. However, such beamsplitters were not available at the laboratory. Additionally, the camera itself emits heat, thus producing thermal infrared light as well, and the same is observed for the environment. Therefore, working with a cooled camera could also be a solution to provide better fringe visibility. However, the most interesting solution would be to change the first beamsplitter to allow more light to be reflected toward the first mirror. This would make the object beam more intense than the background noise, effectively reducing, or even suppressing it.

In addition to that, a complete radiometric study should be performed choose the beamsplitters correctly. In particular, the background noise should be considered, along with the noise emanating from the hot camera. With these, it could be possible to characterize how much flux, hence intensity, would be required to overcome these sources of noise. After that, it could also be of interest to choose beamsplitters with larger wedges, effectively driving the stray beams out of main beam's path. Finally, considering all these, the background noise would be completely blinded by the signal of interest and fringes should appear. With these, it will then be possible to perform holography.

7 | Discussion and conclusions

The topic of this Master's thesis was to study how it is possible to develop a holographic setup working in the thermal infrared wavelengths, specifically based on incoherent light coming from the thermal self-emission of objects.

First, it was necessary to understand how a classical holographic setup based on coherent light works and how to adapt it to a setup suitable for incoherent light. In a classical setup, temporal and spatial coherence is generally ensured by the use of laser sources, allowing the reference and object arms to have unequal lengths. However, in the case of naturally incoherent sources, through theoretical and bibliographic studies, it became evident that interferometric configurations with common paths need to be used, mainly Michelson and Mach-Zehnder interferometers. With such configurations, one of the arms is the object arm, and the other is altered to form a reference beam, which allows obtaining high spatial coherence.

From that, it was possible to determine how the Master's thesis was going to unfold. In particular, it was deemed interesting to align the potential setup in the visible domain and then switch to the infrared. This was nearly necessary as without previous experience in interferometry, aligning a setup without visualizing the beams is very difficult. In order to determine the feasibility of both interferometric setups, the ZnSe components available in the optical laboratory were first assessed. These components are transparent to red and longer wavelengths, making them suitable for initial alignment in the visible domain before switching to the infrared. Following this, numerical simulations, with a homemade ray tracing program coded on MATLAB, were performed. This demonstrated the feasibility of the Mach-Zehnder interferometer, unlike the Michelson, due to either unavailable components or practicality. Specifically, the Michelson configuration would have required a distance of a few meters between the setup and the camera. Additionally, due to the larger number of degrees of freedom in the optical components, the Mach-Zehnder configuration was deemed more practical.

Next, the practical implementation of the Mach-Zehnder interferometer could start. First, it was important to place the mirrors on translation mounts, which allowed more freedom on their position. In addition to that, after computing the most restrictive coherence length, i.e., the one of incoherent white light, it was proved that the kinematic optics mounts were able to yield a sufficient degree of accuracy to place the components precisely within that coherence length. Concerning the beamsplitters, these were mounted on tip/tilt/rotation mounts, and their position was fixed on the optical bench directly. These mounts also yield a degree of accuracy sufficient to fine-tune their position and rotation. This choice was motivated by the practicality of fixing the beamsplitters on the table while allowing the movement of the mirrors. Indeed, if the beamsplitters are fixed, moving a mirror in one direction varies the optical path length of one arm, which can be corrected by moving the other mirror. After these considerations, a coherent visible source, in this case a Helium-Neon laser, was chosen. This provided a coherent source of light to perform the alignment in the visible domain. Then, it was possible to roughly place the optical components on the optical bench, based

on the simulations. This required a precise methodology to follow in order to ensure that the optical components and the light beams were following the expected behavior. In particular, the wedges of the beamsplitters were manually modified to ensure the most practical behavior for the experiment. As well, diaphragms were used in pairs to ensure that the optical axis was followed correctly, and departures from it, due to the wedges, were accounted for.

After this first rough alignment of the components, a camera was placed in order to capture the interference patterns at the output of the interferometer. It was considered that only one component had to be moved in order to equalize the length of each arm, in this case, the second mirror was chosen. This led to a further refinement of the position and angle of the mirror, ensuring that the beams were perfectly co-aligned, thus producing a flat fringe. Nevertheless, this did not mean that the length of each arm was equal, or at least within the coherence length for white incoherent light interferometry. This is because the He-Ne laser has a very large coherence length, ensuring that an interference pattern will be visible, even if the lengths are not equal. Thus, to equalize the length of each arm, it was necessary to use another source that provides a lower coherence length. The superK Compact, providing incoherent light over the 400-2400 nm range was thus used. Nevertheless, a dichroic mirror was used to eliminate part of the infrared radiation. Following this, filters centered in close vicinity of the red wavelength were used. In particular, to progressively decrease the coherence length compared to the He-Ne laser, filters with a 3 and 50 nm bandwidth were used. The position and angle of the second mirror were tuned to obtain fringes for each filter, thus resulting in a more precise alignment of the optical components. After this, it was possible to obtain fringes without any filter, i.e., the setup was aligned for white incoherent light interferometry. Hence, the Mach-Zehnder configuration was ready to be used in the infrared domain as the coherence length in the infrared is larger than the one for broadband white light.

It was then necessary to find a self-emitting source, in this case, a welding iron at 450°C. Then, following Pedrini's experiment, a pinhole was placed in the arm providing the most intense light, effectively creating a spherical wavefront in that arm. In the other arm, a lens was carefully placed to yield a one-to-one image of the object on the camera. Images were then acquired but they prove to be very noisy. Even after post-processing, it was not possible to obtain fringes in the infrared domain. The assumption is that the first beamsplitter only provides a reflection of one percent of the incoming light, which is not enough. The consequence of this is that the object beam is mixed with the thermal noise of the surroundings, rendering any pattern invisible. It was therefore not possible to obtain any fringe pattern in view of holographic reconstruction as there were no other beamsplitters available in the optical laboratory. Nevertheless, the setup is ready and one can only change the beamsplitters that are already mounted on the platforms in order to overcome the intensity problem.

In the future...

In order to enhance the visibility of the fringes, and therefore allow for holographic reconstruction, the first beamsplitter should be replaced with one providing higher reflection. A good guess would either be a 10 or 30% reflection, instead of 1%. This would provide more flux in the object's arm which will overcome the noise emanating from the surroundings. However, a more precise radiometric study is necessary to correctly assess the current flux and the variation from it with higher reflection beamsplitters.

Even though the setup only proved to work in the visible domain, it opens the path for in-depth study to make it work in the infrared domain. In particular, supplementary studies, such as precise radiometric calculations and beamsplitter choice would be necessary. Being able to perform holography with a self-emitting object could be very useful in the space industry. Indeed, considering the non-destructive testing, any object emitting thermal infrared light could be tested without requiring any coherent source for the reference beam. More generally, this type of setup would be pioneering in achieving holographic reconstruction using self-emitted incoherent infrared light. Thus in could provide significant advancements for various future applications.

References

[1] Dennis Gabor. 'A New Microscopic Principle'. In: *Nature* 161.4098 (1948), pp. 777–778.

[2] E. N. Leith and J. Upatnieks. 'Wavefront Reconstruction with Diffused Illumination and Three-Dimensional Objects'. In: *Journal of the Optical Society of America* 55.11 (1965), pp. 1361–1369.

[3] J. W. Goodman and R. W. Lawrence. 'Digital Image Formation from Electronically Detected Holograms'. In: *Applied Physics Letters* 11.3 (1971), pp. 77–79.

[4] P. Hariharan. *Optical Holography: Principles, Techniques, and Applications*. Cambridge University, 1996.

[5] C.M. Vest. *Holographic Interferometry*. New York: John Wiley & Sons, 1979.

[6] T. Kreis. *Handbook of Holographic Interferometry – Optical and Digital Methods*. Wiley-VCH, 2005.

[7] P. Smigielski. 'General review on the investigations conducted at Institute Saint-Louis (ISL) in the field of holographic nondestructive testing'. In: *Proc. SPIE*. Vol. 349. 1982, pp. 72–90.

[8] C. Le Floc'h and B. Gagnage. 'Industrial application of holography in Aerospatiale'. In: *Proc. SPIE*. Vol. 349. 1982, pp. 118–129.

[9] R. Wuerker et al. 'Holography on the NASA Space Shuttle'. In: *AIP Conference Proceedings* 65 (1980), pp. 450–459.

[10] J. Trolinger, R. Lal and A. Batra. 'Holographic instrumentation for monitoring crystal growth in space'. In: *Opt. Eng.* 30.10 (1991), pp. 1608–1614.

[11] K.H. Sill, K. Heimann and M. Roth. 'HOLOP D-2, a holographic interferometer for microgravity research in space'. In: *Proceedings of the European Space Agency*. Vol. 295. ESA SP. 1989, pp. 575–580.

[12] F. Dubois et al. 'An integrated optical set-up for fluid-physics experiments under microgravity conditions'. In: *Measurement Science & Technology* 10 (1999), p. 934.

[13] M. Georges et al. 'Digital holographic interferometry with CO2 lasers and diffuse illumination applied to large space reflector metrology'. In: *Appl. Opt.* 52 (2013), A102.

[14] J.F. Vandenrijt et al. 'Digital holographic interferometry in the long-wave infrared and temporal phase unwrapping for measuring large deformations and rigid body motions of segmented space detector in cryogenic test'. In: *Opt. Eng.* 55.121723 (2016).

[15] F. Dubois et al. 'Digital holographic microscopy with reduced spatial coherence for 3D particle flow analysis'. In: *Appl. Opt.* 45 (2006), pp. 964–961.

[16] A. El Mallahi, C. Minetti and F. Dubois. 'Automated three-dimensional detection and classification of living organisms using digital holographic microscopy with partial spatial coherent source: application to the monitoring of drinking water resources'. In: *Appl. Opt.* 52 (2013), A68–A80.

[17] *Coherent and incoherent optics*. 2022.

[18] Myung K. Kim. 'Full color natural light holographic camera'. In: *Opt. Express* 21.8 (22nd Apr. 2013), p. 9636. ISSN: 1094-4087. DOI: 10.1364/OE.21.009636. URL: https://opg.optica.org/abstract.cfm?URI=oe-21-8-9636 (visited on 16/02/2024).

[19] E. N. Leith and J. Upatniek. 'Holography with achromatic-fringe systems'. In: *J. Opt. Soc. Am.* 57.8 (1967), p. 975.

[20] F. Dubois, L. Joannes and J. C. Legros. 'Improved three-dimensional imaging with a digital holography microscope with a source of partial spatial coherence'. In: *Appl. Opt.* 38.34 (1999), pp. 7085–7094.

[21] Nils H. Abramson and Kenneth G. Spears. 'Single pulse light-in-flight recording by holography'. In: *Appl. Opt.* 28.10 (15th May 1989), p. 1834. ISSN: 0003-6935, 1539-4522. DOI: 10.1364/AO.28.001834. URL: https://opg.optica.org/abstract.cfm?URI=ao-28-10-1834 (visited on 16/02/2024).

[22] Giancarlo Pedrini et al. 'Digital holography of self-luminous objects by using a Mach–Zehnder setup'. In: *Opt. Lett.* 37.4 (15th Feb. 2012), p. 713. ISSN: 0146-9592, 1539-4794. DOI: 10.1364/OL.37.000713. URL: https://opg.optica.org/abstract.cfm?URI=ol-37-4-713 (visited on 16/02/2024).

[23] Dinesh N. Naik et al. 'Spectrally resolved incoherent holography: 3D spatial and spectral imaging using a Mach–Zehnder radial-shearing interferometer'. In: *Opt. Lett.* 39.7 (1st Apr. 2014), p. 1857. ISSN: 0146-9592, 1539-4794. DOI: 10.1364/OL.39.001857. URL: https://opg.optica.org/abstract.cfm?URI=ol-39-7-1857 (visited on 16/02/2024).

[24] Masatoshi Imbe. 'Radiometric temperature measurement by incoherent digital holography'. In: *Appl. Opt.* 58.5 (Feb. 2019), A82–A89. DOI: 10.1364/AO.58.000A82. URL: https://opg.optica.org/ao/abstract.cfm?URI=ao-58-5-A82.

[25] Sarah Muzard. *Internship Report: Incoherent Digital Holography with Thermal Infrared*. 09/05/2022 - 12/08/2022. May 2022.

[26] Zhenong Zhang and Linxiao Zhu. 'Broadband Nonreciprocal Thermal Emission'. In: *Phys. Rev. Appl.* 19 (1 Jan. 2023), p. 014013. DOI: 10.1103/PhysRevApplied.19.014013. URL: https://link.aps.org/doi/10.1103/PhysRevApplied.19.014013.

[27] Marc P. Georges et al. 'An overview of interferometric metrology and NDT techniques and applications for the aerospace industry'. In: 2016. DOI: 10.1117/12.2240676.

[28] M. Locatelli et al. 'Imaging live humans through smoke and flames using far-infrared digital holography'. In: *Optics Express* (2013). DOI: 10.1364/OE.21.005379.

[29] Jaromir Behal et al. 'On the optical performance of incoherent digital holography for extended 3D objects'. In: *Optics Laser Technology* 170 (2024), p. 110286. ISSN: 0030-3992. DOI: https://doi.org/10.1016/j.optlastec.2023.110286. URL: https://www.sciencedirect.com/science/article/pii/S0030399223011799.

[30] *ZnSe Broadband Plate Beamsplitters for the Infrared*. https://www.thorlabs.com/newgrouppage9.cfm?objectgroup_id=4805. (Visited on 18/03/2024).

[31] Y Beers. *The Theory of the Optical Wedge Beam Splitter*. Vol. 146. NBS Monograph. Oct. 1974.

[32] Tatiana Amotchkina et al. 'Characterization of e-beam evaporated Ge, YbF3, ZnS, and LaF3 thin films for laser-oriented coatings'. In: *Appl. Opt.* 59.5 (Feb. 2020), A40–A47. DOI: 10.1364/AO.59.000A40. URL: https://opg.optica.org/ao/abstract.cfm?URI=ao-59-5-A40.

[33] Richard A. Smith, Robert J. Hocken and Michael J. Withford. 'Principles of Interferometry'. In: *Progress in Optics* 53 (2009), pp. 169–298.

[34] Thorlabs. *Solis® High-Power LEDs for Microscopy*. URL: https://www.thorlabs.com/newgrouppage9.cfm?objectgroup_id=8986 (visited on 25/05/2024).

[35] NKT Photonics. *SuperK COMPACT*. URL: https://www.nktphotonics.com/products/supercontinuum-white-light-lasers/superk-compact/ (visited on 25/05/2024).

[36] Thorlabs. *Dichroic Mirror - DMSP1000*. 2024. URL: https://www.thorlabs.com/newgrouppage9.cfm?objectgroup_id=9240&pn=DMSP1000 (visited on 25/05/2024).

[37] Thorlabs. *LG11 Certified Laser Safety Glasses*. URL: %5Curl%7Bhttps://www.thorlabs.com/newgrouppage9.cfm?objectgroup_id=762&pn=LG11#5593%7D (visited on 25/05/2024).

[38] Theodore L. Bergman et al. *Fundamentals of Heat and Mass Transfer*. 7th ed. John Wiley & Sons, 2011.

[39] Xenics. *Gobi+ 640 Series*. URL: https://www.exosens.com/system/files/2024-01/Xenics_LWIR_Gobi%2B%20640%20Series_Leaflet.pdf (visited on 27/05/2024).

8 | Appendix

8.1 Interferometry

Starting from

$$E(t) = E_{01}\,\cos(\omega t) + E_{02}\,\cos(\omega t + \Delta\phi)\,, \tag{8.1.1}$$

and using successively

$$\begin{cases} \cos(\omega t + \Delta\phi) = \cos(\omega t)\cos(\Delta\phi) - \sin(\omega t)\sin(\Delta\phi) & \text{(Compound angles)} \\ \cos(\omega t) + \cos(\Delta\phi) = 2\cos\left(\frac{\omega t + \Delta\phi}{2}\right)\cos\left(\frac{\omega t - \Delta\phi}{2}\right) & \text{(Simpson's formula)} \end{cases} \tag{8.1.2}$$

and grouping alike terms yields

$$\begin{aligned} E(t) &= E_{01}\,\cos(\omega t) + E_{02}\,\cos(\omega t)\cos(\Delta\phi) - E_{02}, \sin(\omega t)\sin(\Delta\phi) \\ &= [E_{01} + E_{02}\,\cos(\Delta\phi)]\,\cos(\omega t) - [E_{02}\,\sin(\Delta\phi)]\,\sin(\omega t)\,. \end{aligned} \tag{8.1.3}$$

Each term of Equation 2.3.5 can be developed as follows:

$$\begin{cases} \cos^2(\omega t) & = \dfrac{1 + \cos(2\omega t)}{2} \\ \sin^2(\omega t) & = \dfrac{1 - \cos(2\omega t)}{2} \\ \cos(\omega t)\sin(\omega t) & = \dfrac{\sin(2\omega t)}{2} \end{cases}. \tag{8.1.4}$$